REDOX CONTROLLED TRACE ELEMENT ATTENUATION IN PYRITE: OBSERVATIONS FROM NATURAL & EXPERIMENTAL STUDIES

Josephine M. Ward

A thesis submitted for the degree of Doctor of Philosophy at the Australian National University, Canberra, Australia

May 2020

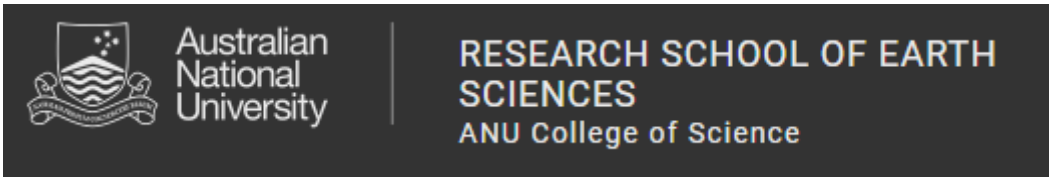

DECLARATION

The work in this thesis is my own except where otherwise stated.

Josephine M. Ward

TABLE OF CONTENTS

LIST OF FIGURES

LIST OF TABLES

ACKNOWLEDGEMENTS

There have been many individuals who have aided my learning during this PhD, their time and efforts are greatly appreciated. In particular, I am incredibly grateful for the help, support, guidance and accommodation from John Mavrogenes and his lovely wife, Sarah. I am also thankful that I was fortunate to meet Bear McPhail and benefit from such a wonderful teacher. I was very lucky to learn from him.

Thank you to Brian Harrold for all of the chats and amazing help with modelling programs. Thank you to Stephen Cox and Peter Holden for the troubleshooting and advice. Thank you to the technical team at R.S.E.S for teaching me how to use the machines and not severely injure myself, or more importantly, the samples in the process.

In many aspects, completing a PhD is a selfish task. I owe a huge thanks to my amazing Mum, Dad and Husband (Margaret, John and Sam) for all of the travel, support and time they have put in to help me finish this thesis, all the while helping me move, plan a wedding and navigate being a Mum. Their efforts are immeasurable and so very appreciated.

Special thanks to Sam, Ella and Dot for giving me quiet time and patiently listening to me talk about minerals they didn't know or ever wanted to know about.

ABSTRACT

Pyrite (iron disulphide) is ubiquitous in economic gold deposits where it is often precipitated at every paragenetic stage during mineral deposit formation. Pyrite can also accommodate a wide gamut of elements over an extensive range of pressures, temperatures, and oxygen and sulfur fugacities. Gold can also be accommodated in pyrite either as inclusions or physically within the crystal lattice. This thesis investigates the possibility of using pyrite crystals to track and monitor changes in geochemistry during hydrothermal deposition, in particular Au-ore formation. Studying pyrites from varied geologic deposits and experimental settings, the globally observed relationship between As and gold will be investigated.

The Au-deposit Wallaby (WA) is a major deposit which exhibits 5 generations of mineralised veins that each contain pyrite. Trace element concentrations acquired using LA- ICP MS, coupled with micro-scale $\delta^{34}S$ SHRIMP- SI analyses (3µm) has demonstrated that pyrite displays progressive and systematic changes in geochemistry, particularly in respect to As and nickel. Thus, pyrite can be used as a monitor of changing redox conditions. The ability to trace gradual changes in ore deposit chemistry during formation (indeed within single crystals via core-rim relationships) allows for new information on where and how an element of interest was deposited. This has wider implications for ore exploration.

Argo (WA) is a mesothermal lode gold deposit which exhibits fluid-rock interaction culminating in 4 mineralised veins. All veins contain pyrite and the later stage veins contain pyrrhotite. Similarly to Wallaby, trace element analyses via LA- ICP MS and $\delta^{34}S$ SHRIMP- SI analyses have shown changes in the pyrite geochemistry however, the appearance of pyrrhotite, a competing Fe-S mineral, causes these trends to differ. This study documents how co-precipitation of related minerals can greatly influence the concentrations of trace

elements in pyrite and how partition coefficients may be successfully employed to better understand these changes and relate these to systematic changes relative to Au deposition.

The S and I Type granites of the Lachlan Fold Belt are best known for classification systems based upon bulk chemistry. While rare, sulfides such as pyrite are observed in these granites. Due to their limited abundance, pyrites have not been investigated thoroughly in the LFB granites and as such present an excellent opportunity to use a single mineral approach using LA-ICPMS and SHRIMP-SI in an attempt to delineate pyrites based on redox. The trends observed in the pyrites of the LFB granites suggest a wider control on partitioning of elements into sulfides and how this is linked to ore deposit genesis.

At Wallaby, Argo and the Lachlan Fold Belt Granites, high As pyrites were related to Au in reduced conditions. Currently there is no clear understanding of what drives the mode or tenor of gold deposition over a range of redox conditions in the presence or absence of As. How Au oxidation states may be related to gold transport is also unclear. The experiments in this thesis aim to provide understanding into how a gold deposit bearing pyrite, may form (in particular Carlin type). Experiments are set over a range of oxygen fugacities and use CVT for crystal synthesis. Crystals were doped with As, Au^0 and Au^+. While As and Au (regardless of oxidation state) were shown to covary, although As and Au concentrations in pyrite increased systematically with reduction in experiments starting with As+Au^0, in runs starting with As+Au^+ concentrations decreased with reduction. This contrasting behaviour is controlled by the mode of gold deposition, i.e whether gold deposits as free gold or within the pyrite structure.

The results demonstrate the usefulness of pyrite as a monitor of reduction over a range of geological settings. This implies a wider universal control on pyrite deposition which this

thesis investigates. The trends observed in both the natural and experimental studies potentially explain why some magmatic rocks are more likely to host ore bodies and how factors influencing mineralisation can affect the tenor of differing ore deposit types.

1. INTRODUCTION

1.1 INTRODUCTION

Pyrite, iron disulfide, forms over a range of conditions and can contain Au and other trace elements in concentrations of significant economic value (Abraitis et al., 2004; Deditius et al., 2014). The association between Au and As in pyrite is well established, yet is not fully understood with relation to oxidation-reduction (redox). Pyrite is found over a range of diverse geological settings, and the systematic variation in trace elements within pyrite likely records information about the depositional conditions, particularly redox. This thesis aims to investigate ore deposition over a range of redox conditions utilizing pyrite as a sensor and to subsequently systematically explore the effects of redox changes on pyrite trace elements.

1.2 THESIS STRUCTURE

This thesis is set out in a modern style where each chapter is written as an independent research paper. Each paper links to the thesis' general theme (redox effects on pyrite trace element attenuation) and builds towards answering particular questions about pyrite in ore systems as detailed in the aims section. The Appendices for each paper are located at the end of this thesis and the pertinent references can be found at the conclusion of each chapter.

The layout is as follows:

1. **Introduction and Background Information**
2. **Published Paper 1 –** ***Trace element and sulfur isotopic evidence for redox changes during formation of the Wallaby Gold Deposit, Western Australia***
3. **Paper 2 -** ***Trace element partitioning between pyrite and pyrrhotite as a monitor of fluid evolution at the Argo (WA) Gold Deposit***

4. **Paper 3 -** ***The link between granites and hydrothermal ore deposits: the Lachlan Fold Belt granite connection***
5. **Paper 4 –** ***Redox controlled variation of Au and As in synthesised pyrite***

1.3 AIMS

1. To test trace element suites and sulfur isotope data (a known oxygen fugacity sensor) within natural pyrite from hydrothermal gold deposits and from a selection of S & I type granites. Sample sites were chosen to best reflect systematic changes in pyrite chemistry relative to changes in redox.
2. To use a process modified from Lenher (2006) to grow pyrite crystals containing gold and/or As over a range of oxygen fugacities (log fO_2 -4 to -24). This was designed to track how Au and As attenuation in pyrite varies with redox conditions and how these two key trace elements interact within pyrite. These experiments were also designed to establish if the oxidation state of Au affects its uptake into pyrite.
3. The outcomes of the small-scale analyses of natural experimental pyrites will be related to large scale depositional processes in metallic mineral deposits.

1.4 LITERATURE REVIEW

Pyrite – A Global Context

Pyrite (FeS_2), is a versatile mineral found in sedimentary, igneous and metamorphic rocks ((Craig et al., 1998; Mann et al., 1990). Pyrite is often formed during late stage crystallisation and has been shown to survive high-grade metamorphic conditions. It can have a range of micro-textures and crystal attributes that reflect structural and depositional characteristics of its geologic setting (Craig et al., 1998). Trace and minor element impurities in pyrite can cause different patterns of chemical zoning in pyrite i.e concentric zoning such as that observed at

Porgera (PNG) (Peterson and Mavrogenes 2014) and simple to complex overgrowth patterns at Gilman, Colorado (Craig et al., 1998). These patterns are indicative of changing geochemical conditions during deposition. An incredible range of trace elements have been found within pyrite, including Au, As, Sb, Hg, Ni, Co, Cu, Tl, Ag, Zn, W, U, Pb, Bi, Se and Te (Abraitis et al., 2004; Reich and Becker, 2006). However, in gold deposits, where As-rich pyrite and arsenopyrite are identified as the most likely minerals to host gold (Cook and Chryssoulis, 1990), the As-gold connection is of great economic importance. Recent studies have also indicated that plastic deformation experienced by pyrite may influence the concentration of trace elements such as As and Co found within the crystals, thus establishing an alternate diffusion mechanism (Dubosq et al., 2019; Fougerouse et al., 2019; Wu et al., 2019). Pyrite forms as a function of its depositional environment and the sulfur isotopes and trace element budgets of pyrite are sensitive to changes in reduction. So, analysis of the trace elements and sulfur isotopes within individual crystals provides insights into how ore deposits formed.

Sulfur isotopes have been utilised in Cu-Au porphyries to quantify the redox of mineralising fluids and/or intrusive bodies (Deyell and Tosdal, 2005). Four stable isotopes of sulfur (^{32,33,34,36}S) exist in nature (Thode, 1970) but only two (32 and 34) are routinely used in ore deposit studies. Isotope fractionation, or deviation of these ratios relative to the Canyon Diablo meteorite, can occur due to pH, temperature and/ or oxygen fugacity, thus providing an indication of large - scale geological process attending mineral deposition (Ohmoto, 1972; Rye, 2005; Thode, 1970). The $^{32/34}$S ratio is a robust indicator of these changes in pyrite (Ohmoto, 1972; Thode, 1970; Zheng, 1991). The sulfur fugacity of a hydrothermal ore fluid can also limit the δ^{34}S of pyrite (Ohmoto, 1972). Sulfur isotopic analysis provides an indication of the physio-chemical parameters from which a crystal formed. In zoned crystals, small spot

measurements are able to track changes in the ore forming fluid as crystallisation progressed. This provides a record of incremental changes in fluid over time.

Optical microscopy and bleaching techniques reveal pyrite zoning and modes of gold occurrence. Bleached samples from the Suurikuusikko deposit, Central Lapland highlighted both Au inclusions and systematic zonation patterns. Subsequent leaching of these samples yielded 4% Au available from 'free gold' and 57% from 'bound' gold, the remaining gold sequestered in other minerals (Kojonen and Johanson, 1999) demonstrating the extreme variability of concentration mechanisms for Au in pyrite. Trace element zone mapping using micro- PIXE (Particle induced X-ray emission) of pyrite from the mesothermal Saldania Belt (South Africa) highlighted geochemical zonation across pyrite surfaces that showed barely perceptible petrological differences. Interestingly, 'invisible Au' at core-rim boundaries between As-rich and As-poor pyrite zones were interpreted as gold deposition via electro-chemical precipitation (Belcher et al., 2004). Further, these pyrites showed zonation in other trace elements (Sb, Ni, and Pb), supporting the idea that physical conditions during formation can greatly affect trace element attenuation in pyrite and as such, are a valuable source of depositional information. It is increasingly common for pyrite to be used to identify key stages during ore formation via trace element and textural similarities, as observed in Archean Yilgarn (WA) deposits (Godefroy-Rodríguez et al., 2020; Godefroy-Rodríguez et al., 2018) and employed to infer other information i.e the geochemical conditions of ancient ocean beds (Gregory et al., 2019).

Archean Witwatersrand Basin pyrites have distinct trace element zonation patterns (in particular, Sb, Mn, Au, Ag, Tl, Mo and Cu) and textural differences between paragenetic stages. These features identified two modes of gold in pyrite which define a depositional

history (Agangi et al., 2015). $\delta^{34}S$ and $\delta^{33}S$ data combined with textural and trace element trends from pyrite showed significant differences between pyrite generations, dependent on fluid source(s) and modes of deposition in the Witwatersrand Basin. This suggests that geochemical features of pyrite yield important information regarding depositional environment and conditions during ore formation.

The Dexing (China) Cu Porphyry deposit contains copious pyrite with strong oscillatory zoning of either Cu-rich or As-rich zones (Reich et al., 2013). This complex chemical zoning resulted from trace elements, such as Cu, As and Au, residing in solid solution or as micro-inclusions. The alternating zones of Cu- and As-rich pyrite show clear decoupling of Cu and As, supporting the theory of selective partitioning recorded on a small scale as a result of fluctuating hydrothermal ore fluid conditions. This suggests that systematic changes in fluid are clearly recorded, even in trace concentrations, and observed on small scales within crystal zones. Thus, pyrite makes a robust monitor for hydrothermal depositional processes.

Sunrise Dam (WA), an Archean hosted gold deposit formed syn- to post-greenschist facies metamorphism (Sung et al., 2009) contains pyrites that display chemical and textural differences across mineralisation stages that effectively record fluid history. The pyrites contain gold and other trace elements that reflect gradual changes during progressive mineralisation events caused by significant structural triggers (Sung et al., 2009). Close examination of the pyrite shows a link between a particular structural event and the highest Au and Te (ppm) pyrite concentrations reported in the Yilgarn Province. This led to an improved understanding of ore deposition at Sunrise Dam and better exploration targeting. Multivariate statistics have been employed to investigate trace element trends in pyrite on a large scale at Olympic Dam, showing that this pyrite is clearly defined by two trace element

trends and that gold is most likely shown as two different forms at this deposit (i.e free gold and as electrum with tellurides) (Dmitrijeva et al., 2020). Co:Ni ratios were vital during calculations to determine the two pyrite trends at Olympic Dam.

Carlin deposits host a significant portion of Earth's gold (Chen et al., 2014a; Cline et al., 2005; Zhao et al., 2020), formed via mass replacement and alteration of silty carbonates. Decarbonisation is thought to have destabilised Au and prompted deposition either in solid solution or as native gold particles within pyrite (Cline et al. 2005). These pyrite crystals have distinct core–rim trace element zoning in As, the boundary of which represents a change in hydrothermal fluid that prompted economic gold deposition within As-rich pyrite. This precipitation of gold is believed to have been caused by a change in redox. How these metals are transported in such high concentrations is still not clear. Understanding the physiochemical processes that lead to high concentration of gold sequestering into pyrite will help targeting gold in the future.

Why is pyrite important in Gold deposits and how is it related to Au-As trends?

Chen et al. (2014) found that 85% of the gold present in the 102 gold deposits they studied resided within pyrite. The stoichiometric variability of pyrite is small, however enrichment in key trace elements such as As has been reported up to 10 wt % and may influence whether or not pyrite can incorporate gold within its structure (Abraitis et al., 2004). While Chen et al. (2013) used Density Functional Theory (DFT) to show that invisible gold was most often incorporated as Au^{+} in the pyrite lattice, Fleet and Mumin (1997) maintain that invisible Au^{0} may also exist. DFT has shown that the presence of As in pyrite distorts the pyrite structure enabling Au^{+} to substitute directly for Fe by warping the pyrite lattice (As substitution for S), this is confirmed by the strong positive correlation seen between As and Au globally (Chen et

al., 2013). An increase in As is shown to increase the reactivity of pyrite, even in the presence of other trace elements (Lehner et al., 2007). This supports modelling of pyrite with As and Au exhibiting lower energy gaps for reduction by changing pyrite from a P-type to n-type conductor (Chen et al., 2013).

The solubility of Au, when in the presence of a pyrite- pyrrhotite is understood to be controlled by temperature, pressure, pH, oxidation potential and available sulfur (Seward, 1973). Experiments conducted suggest that gold is transported in hydrothermal fluids as both thio- and chloro- complexes and is deposited by destabilising one of these controls (Seward, 1973). Gold ions (Au^{+} and Au^{+3}) are not stable in hydrothermal fluids, consequently Au is understood to travel as a chloride or sulfide complex (Liu et al., 2014; Stefánsson and Seward, 2004). Invisible gold has been shown to form via adsorption and reduction of Au^{3+} to Au^{+} from a chloride solution on pyrite surfaces in a manner that mimics natural observation (Maddox et al., 1998; Mycroft et al., 1995). Maddox et al. (1998) suggest that Au^{3+} in solution is reduced by pyrite, whereby surface ferrous iron plus Au^{3+} produces Au^{+} and ferric iron via adsorption.

The covalent reaction between Au^{+} and HS^{-} has been observed (Reich and Becker, 2006) to occur due to greater electrostatic attraction with increasing temperature (Stefansson and Seward, 2004). Experimental data suggests that adsorption of gold complexes on the surface of iron sulfides, such as pyrite, is vital during the formation of gold deposits from hydrothermal fluids (Widler and Seward, 2002), thus understanding pyrite deposition over a range of redox conditions and how this may affect trace element accumulation is of interest.

Carlin type gold deposits, orogenic gold deposits and epithermal gold deposits all display a strong As- Au relationship in As-rich pyrite, suggesting that As is important during Au ore

formation (Liang et al., 2013). Arsenian pyrite is widely understood to contain As^{1-} ($Fe(As_xS_{1-x})_2$) and no As oxidation states other than this were found in the Yang-shan Carlin type Au deposit (Liang et al., 2013). While As is known to control Au solubility (Reich and Becker, 2006), the nature of the relationship relative to variable redox conditions and how that may influence the pyrite lattice and gold deposition is unknown.

The speciation of metal sulfides in magmatic, epithermal and hydrothermal systems is largely responsible for the deposition of ore deposits. Reaction modelling of As species and comparisons to the Uzon Caldera indicates that As deposition is strongly dependent on available sulfur and reduction, in particular the mixing between the ore bearing fluid and an oxygenated source (Cleverley et al., 2003). Research suggests that oxygen fugacity controls the As –sulfide stability as As^{-1} readily substitutes for S in the sulfide lattice.

Originally, Wells and Mullens (1973) showed minor variations of As in pyrite crystals that directly related to Au contents. Fleet et al. (1993), and Peterson & Mavrogenes (2014) showed oscillatory growth zoning in pyrites with fluctuating As, Ni and Co contents, supporting the idea that pyrite could record information across the entire depositional history. Pyrite containing measurable As is shown to be more reactive that pyrite with Ni, Co or other trace elements (Lehner et al. 2007). Higher current responses observed from As-pyrite suggest that this trace element may create a more reactive surface on pyrite with which other metals react. Analytical data shows the maximum concentration of Au is controlled by a solubility curve between solid solution Au^+ and micro inclusion Au^0 in As-rich pyrite (Reich et al. 2005). Seward (1973) suggests that during sulfidation or boiling processes (i.e Carlin vs Epithermal style Au), Au may be removed from under -saturated fluids and adsorbed via $Au(HS)^0_{(aq)}$ complexes (Equations 1 and 2, Reich et al 2005).

Equation 1 $Fe(S, As)_2 + 2Au(HS)^0_{(aq)} = Fe(S,As)_2.Au_2S^0 + H_2S_{(aq)}$

Equation 2 $Fe^{2+} + 2HAsS_{2(aq)} + 2Au(HS)^0_{(aq)} + 2H_2(g) = Fe(S, As)_2.Au_2S^0 + 3H_2S_{(aq)} + 2H^+$

Analysis of Carlin- type and epithermal pyrites suggest that while gold is reduced from Au^{3+} during deposition, it remains oxidised at Au^+ in the crystallised pyrite (Arehart et al., 1993; Fleet and Mumin, 1997b; Reich and Becker, 2006). Gold is concentrated up to 0.37 wt% in Fe deficient, As- enriched pyrites at Deep Star (Nevada), an example of Au substituting for Fe in the pyrite lattice, although in this case, the oxidation state of Au is unknown (Fleet and Mumin, 1997b). As oxygen fugacity often is the dominant control during ore deposition, it raises questions as to whether oxidation state, along with the presence of As, plays a more important role in contributing to the formation and tenor of Au deposits than previously recognised.

What does this thesis look like and why does pyrite matter?

Pyrite and arsenian-pyrite are both important sulfides as they have the potential to host high concentrations of invisible gold in ore deposits. Currently, four main factors are understood to control the formation of a hydrothermal Au deposit (Mycroft et al. 1995);

1) Geologic source of the mineralising fluid
2) Au source
3) Transport mechanism(s)
4) Depositional mechanism(s)

This thesis explores the notion that despite an adequate source of mineralising fluid and Au and a transport mechanism, the chemical controls on deposition are the greatest influence in determining the tenor of a pyrite-hosted gold.

In an attempt to observe the role of changing redox on Au deposition in pyrite, three case studies were selected to 'fingerprint' existing trends. The case studies are as follows:

1. Wallaby – This ore deposit has pyrite in every mineralising stage and contains no other Fe-S minerals. The well-established vein paragenesis displays a systematic change in redox from hematite to magnetite. The temperature, pressure and pH were all estimated to be relatively constant, thus redox was the main driver of Au deposition. This study contained well-formed pyrites at every stage that enabled micro-scale SHRIMP-SI analyses to be utilised. This was the first study published to use 3µm spots to track gradual change across single crystals.
2. Argo - This mesothermal lode gold deposit is similar to Wallaby, with pyrite in every stage. This deposit also has an established vein paragenesis, however unlike Wallaby, the latter stages of mineralisation also contain pyrrhotite. This deposit demonstrates the effect of partitioning between two Fe-S minerals during redox driven deposition and how this affects gold deposition.
3. Lachlan Fold Belt Granites – The classification of S- and I- type granites is well established and a major difference is contrasting redox conditions. To the author's knowledge sulfides within these granite types have not been investigated for trace elements and sulfur isotopes. This study aims to observe similar trace element trends (seen in hydrothermal ore deposits) attributed to redox change in pyrite in the two granite groups. This will provide valuable information regarding source and possible

links to deposits found within the same geological region, maybe answering why some granites develop ore deposits, while others do not.

The final aspect of this research is an experimental study. This research aims to establish the relationship between As and gold in pyrite on a small scale and over a range of redox conditions. It aims to evaluate the significance of the oxidation state of gold and how this might be reflected in natural deposits. The solid solution conjugate pairs, hematite – ilmenite and ulvospinel and magnetite, provide excellent buffers to control oxygen fugacity (Buddington and Lindsley, 1964). These demonstrated relationships control oxygen fugacities over a wide range and should allow pyrite to form at set oxygen fugacities, similar to conditions observed in the environment and with minerals routinely identified in nature. This will provide a better understanding of the role of As in forming gold deposits and better direct how we view pyrite in research and exploration.

1.5 PROBLEMS AND LIMITATIONS

This thesis has not been without its problems. Enabling a consistent experimental method to grow adequate redox controlled pyrites for analyses proved extremely challenging. During development, a near complete experimental series of redox-controlled and doped (As and Sb) pyrrhotite was created using a temperature controlled gas mixing furnace to control the redox conditions during crystal growth, the results of which are not discussed here. Many tubes, steel containers and box furnaces also failed during pyrite experimental runs, the product of which was great frustration. While crystals were formed within a sealed tube, it would have been ideal if they had been removed and mounted relative to other pyrites and minerals formed to better comment on any potential textural differences.

LA-ICP MS and SHRIMP analyses of Wattle Gully were also conducted prior to the mid-term. This crack-seal deposit did not provide a systematic study of mineral deposition and was therefore excluded from further work.

2. TRACE ELEMENT AND SULFUR ISOTOPIC EVIDENCE FOR REDOX CHANGES DURING FORMATION OF THE WALLABY GOLD DEPOSIT, WESTERN AUSTRALIA

Published Paper – 2017 – Ore Geology Reviews

Ore Geology Reviews 82 (2017) 31–48

Contents lists available at ScienceDirect

Ore Geology Reviews

journal homepage: www.elsevier.com/locate/oregeo

Trace element and sulfur isotopic evidence for redox changes during formation of the Wallaby Gold Deposit, Western Australia

Josephine Ward *, John Mavrogenes, Amberley Murray, Peter Holden

Research School of Earth Sciences, The Australian National University, Canberra, 0200 ACT, Australia

ARTICLE INFO

Article history:
Received 15 April 2016
Accepted 10 November 2016
Available online 24 November 2016

Keywords:
Yilgarn
Redox
Pyrite
Gold
Isotopes
Zoning

ABSTRACT

Wallaby is a major gold deposit of the St Ives Gold field of Western Australia, with an estimated resource of 8 million ounces of gold. It has a well-established paragenesis across five vein sets that displays macroscopic evidence of changing redox through time; from hematite to magnetite. Micro-analysis of pyrite from each vein generation shows a progressive and gradual change in redox conditions. The sulfur isotope composition has a $\delta^{34}S$ range of −7.7 to +9.8‰ using 3 μm spots on the Sensitive High Resolution Iron Micro Probe-Stable Isotope (SHRIMP-SI). Negative values indicative of an oxidized sulfur signature are found in the earliest generation of pyrite (which coexists with hematite) that also contains high concentrations of As, Ni, Zn, Ag, Sb, Cu and Pb. Conversely, positive values representative of reduced sulfur are found in later generations of pyrite, with lower concentrations of As, Ni, Sb, Cu, Zn and Pb. These later pyrite crystals display higher As/Ni, As/Sb, and As/Bi, and lower Cu/Te. These geochemical trends are the result of redox controlled transport and partitioning into pyrite of minor and trace elements now within the pyrite structure. Previous studies suggested a single orogenic event formed the Wallaby Deposit. This is not supported by the present study. Trace element ratios such as As/Ni clearly delineate the high Au generations and could be used as an exploration tool. It is suggested that pyrite from the Wallaby Gold Deposit formed via desulfidation and a gradual change in redox conditions within an evolving fluid and did not result from mixing of two separate fluids as previously advocated. Utilizing pyrite to link the entire fluid history of Wallaby demonstrates the general use of pyrite as a valuable mineral tracer in gold-bearing fluid systems.

1. Introduction

Despite many years of orogenic gold deposit research, numerous controversies regarding fluid source and depositional mechanisms remain (reviewed by Moritz, 2000). Within the Yilgarn region of Western Australia, the debate focuses on the source of gold, mainly whether it is intrusion related or not. Previous research is divided as the quartz-vein hosted lode gold deposits of the Yilgarn craton display isotopic evidence for magmatic and regional sources (Groves, 1993). The Wallaby Gold Deposit is contained within this region and exhibits characteristics of both orogenic and intrusion related gold deposits. Furthermore, there is no clearly established depositional mechanism for gold in deposits of this type. Wall-rock reactions (Neumayr et al., 2008), fluid mixing (Hodkiewicz et al., 2009, 2005), and decompression (Salier et al., 2004, 2005) are considered the most viable triggers for gold deposition. Cooling is not considered a major control because temperature gradients greater than 100 °C (Salier et al., 2005) are not seen in orogenic deposits generally and in the Laverton Province specifically. Generations of pyrite-magnetite bearing and pyrite-hematite bearing quartz veins establish a clear redox change during the development of the Wallaby Gold Deposit. Previous sulfur isotope studies of the St Ives region show both oxidized and reduced $\delta^{34}S$ signatures (Hodkiewicz et al., 2009, 2005; Neumayr et al., 2008; Salier et al., 2004, 2005) and suggest a correlation between oxidized rock samples and higher gold grades.

Studies of metal solubilities have shown systematic changes as a function of redox. For example, Te solubility increases during reduction at oxygen fugacities below the hematite-magnetite boundary in hydrothermal fluids (McPhail, 1995). Bismuth solubility is also redox sensitive; specifically, oxidation decreases Bi solubility (Skirrow and Walshe, 2002). Conversely reduction decreases Sb solubility (Yang and Blum, 1999). The solubility of many other elements are redox controlled, including all of the transition metals. The response of As to changing oxygen fugacity is important in gold deposits due to its strong association with economic Au grades (Arehart et al., 1993; Pokrovski et al., 2002). In particular

* Corresponding author at: Research School of Earth Sciences, The Australian National University, Building 142 Mills Road, Acton, ACT 2601, Australia.
E-mail address: jo.ward@anu.edu.au (J. Ward).

http://dx.doi.org/10.1016/j.oregeorev.2016.11.011
0169-1368/

Au is closely related to arsenian pyrite and arsenopyrite (Arehart et al., 1993), which are known to precipitate due to reduction (Arehart et al., 1993). As the behavior of trace elements is affected by changing oxygen and sulfur fugacities, these elements can be used to track changes in hydrothermal fluids. At Wallaby, pyrite is observed in every mineralized generation, hence sulfur isotopes can be used to track subtle changes in redox within individual pyrites across the entire history of Wallaby.

Wallaby was selected to test if trace elements and sulfur isotopes systematically change across an independently determined redox gradient. Given that changes in pH or temperature are minimal, all changes in sulfur isotope and trace element concentrations can be attributed to changes in oxygen fugacity. The outcomes of this study will not only document the evolution of the Wallaby deposit but could also define processes and techniques applicable to all orogenic gold deposits. The pyrite selected for this study represent all five generations of mineralization identified within the deposit.

2. Deposit geology

The Wallaby Gold Deposit is located within the well-endowed region of the Eastern Goldfields Province (EGP) within the Yilgarn Craton (Fig. 1). It is part of the Laverton Greenstone Belt (LGB), a north-south trending tectonic zone comprised of two conformable stratigraphic associations of volcano-sedimentary successions (Hallberg, 1985). This deposit sits on the edge of Lake Carey and is hosted within the Wallaby Conglomerate; a poorly bedded mafic polymict unit altered to greenschist facies. This mafic conglomerate is enriched in Fe and provides a source for iron-sulfide formation during alteration/mineralisation events. The clasts are comprised of basalt, andesite, feldspar porphyry and quartz-feldspar porphyry, BIF and quartz in varying quantities and vary in sizes from sub-centimetre to tens of centimetres (Salier et al., 2004 and references therein). Its formation is attributed to regional compression resulting in the uplift of the Margaret Dome, a granite-gneiss cored batholith north of the Laverton terrane, which caused rapid deposition and burial of sedimentary and conglomeratic material in the Lake Carey Basin (Standing, 2008).

Mineralization occurs as a series of vertically stacked sub horizontal lodes within low angle reverse faults dipping 10–25 degrees to the northeast (Fig. 2). These lodes are linked by a series of thinner and steeper structures. Alteration containing albite-carbonate-sericite and pyrite is prevalent but the regional alteration is distinguished from the high-grade ore associated alteration by the presence of hematite, ie high-grade ore does not contain hematite. Gold is typically found within micro-fractures within disseminated pyrite or as coarse visible gold within hydrothermal quartz veins. In-mine drilling indicates that mineralization ceases at Thet's fault, a highly sheared east-west normal fault that separates the base of the Wallaby Conglomerate from underlying volcaniclastics dated at 2715 Ma (Henson et al., 2010). The mineralization is closely associated with an actino lite-magnetite-epidote-calcite (AMEC) alteration pipe (Coggon, 2003). The alteration pipe contains a series of alkaline intrusions representing a fractionating suite from mafic monzonite to syenite and carbonatite (Mueller et al., 2008).

2.1. Actinolite-magnetite-epidote-calcite (AMEC) alteration pipe

The presence of a magnetic 'bullseye' on regional aeromagnetic surveys led to the discovery of Wallaby in 1997. The magnetic anomaly is attributed to the presence of magnetite within the AMEC alteration zone. In addition to the AMEC, the assemblage includes albite, biotite, chlorite, and quartz (Wall, unpublished Placer Dome Report, 2001). The AMEC pipe, as modelled by Coggon (2003), is broadly ellipsoidal. This alteration is destroyed during the early stages of gold mineralization when hematite forms at the expense of magnetite. The relative timing of the AMEC halo is debatable. Miller (2006) and Mason (unpublished Placer Dome Report, 1999) suggest that the AMEC halo post-dates intrusion emplacement and is observed to cross-cut the conglomerates and intrusive suite. Mueller et al. (2008) suggest the alteration is a result intrusive activity forming 'skarn' like alteration in the conglomerate. Although proximal metasomatic alteration may exist near the syenite dyke swarm, Salier et al. (2004) doubts that the magmatic fluids are responsible for pervasively altering such a large volume of surrounding rock. Mueller et al. (2008) dated the AMEC halo with a concordant titanite U-Pb age of 2662 ± 3 Ma. There is a general consensus that the AMEC halo created a large brittle volume with a high Fe/(Fe + Mg) – favorable conditions for structure formation and later auriferous fluids.

The majority of gold identified within this study is found as 1–10 μm inclusions within pyrite of Generation 3 and cores of Generation 4 pyrites, however, bonanza grade gold at Wallaby is found in brecciated quartz veins associated with Generation 4 and 5 pyrites. Generation 4 and 5 veins sampled for this study also contain native gold.

Mineral assemblages exhibit two distinct redox conditions. There are 5 generations of veining at Wallaby that are established through crosscutting relationships (Figs. 3 and 4). Within these veins individual pyrite textures, mineral associations and the presence or absence of inclusions enables categorization into discrete pyrite generations. Only Generation 1 pyrite, the earliest formed, is identified with hematite. Subsequent generations are associated with magnetite. Current research attributes early, oxidized iron oxide phases to porphyritic intrusions (Standing, 2008). Hematite-bearing veins, associated with E-W trending faults (Neumayr et al., 2008), are crosscut by magnetite-pyrite-quartz (Fig. 3) veins.

Pyrite crystals within each generation are morphologically distinct. Earlier generations are porous and contain small mineral inclusions, – a common feature of low temperature (270° ± 50°, Salier et al., 2004) hydrothermal pyrites (Deditius et al., 2011). Electrum inclusions, often found within pyrite crystals at Wallaby, are common to hydrothermal pyrites worldwide (Cook and Chryssoulis, 1990). Where possible, inclusions were avoided during microanalyses to focus on elements in the pyrite crystal lattice.

Differences in minor and trace element concentrations in pyrite have previously been shown to change the properties of pyrite and have been mapped chemically in discrete zones by proton-induced X-ray emission (PIXE), electron micro-probe analysis (EMPA), nanoscale secondary ion mass spectrometry (nano-SIMS) and laser ablation (LA-ICPMS) (Belcher et al., 2004; Large et al., 2009; Lehner et al., 2006). Chemical changes across progressive pyrite generations have been used to link pyrite generations to ore forming events like those related to Carlin-type and orogenic gold deposits (Large et al., 2009; Raiswell and Plant, 1980). Changes in pyrite with minor and trace element signatures across vein parageneses have been suggested as a tracer for changes in ore-fluid composition and electrochemistry (Belcher et al., 2004; Reich et al., 2013). The successive generations of pyrite display changes in trace element geochemistry that coincide with changes in pyrite mineral assemblages i.e. changes from hematite-pyrite to magnetite-pyrite assemblages, implying *a clear redox change.*

3. Methods

3.1. Sample selection

This study aimed to trace gold and geochemical trends via a single mineral approach on a micro-scale not previously attempted.

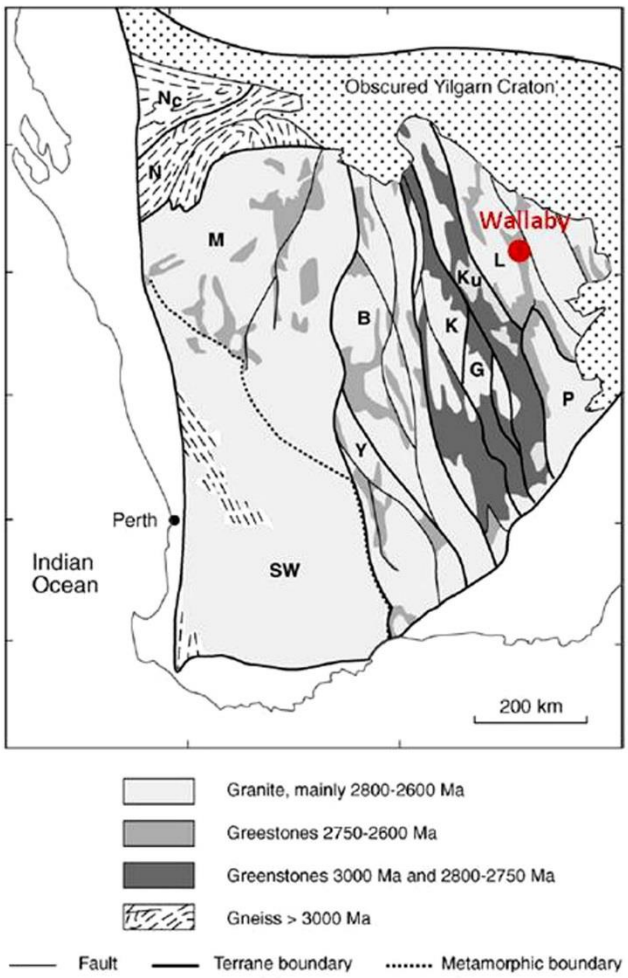

Fig. 1. Map of the terrane structure of the Yilgarn Craton, after Myers (1997). Black letters are identifying provinces as follows; B, Barlee; K, Kalgoorlie; M, Murchison; N, Narryer; Nc, Narryer terrane affected by the Capricorn Orogeny; SW, southwest Yilgarn composite terrane; Y, Yellowdine; Ku, Kurnalpi; G, Gindalbie; L, Laverton; P, Pinjin (Kositcin et al., 2008; Swager, 1997). The Wallaby Gold Deposit is marked in red and is within the Laverton Greenstone Belt. (For interpretation of the references to colour in this figure legend, the reader is referred to the web version of this article.)

This approach reveals the fluid history of Wallaby. The sample selection represents all 5 pyrite generations (other than native gold the dominant sulfide returning Au grade). Once understood, this could be studied regionally for potential exploration targets.

Samples representing each vein generation and containing abundant pyrite were collected from the Wallaby Gold Deposit within the 600 m wide AMEC alteration halo from 3 drill cores (WB0801CD, WB1274UD and WB1274UD) and an underground grab sample from the zone 70 ore load. Sampling provided pyrite crystals from all generations (Appendix 1). Hand specimens were selected based on visual evidence of cross-cutting relationships in drill core and mineralogy. Rock samples were cut and prepared into polished mounts. These mounts underwent petrological study by reflected light microscopy after etching with NaOCl for 6 min to reveal zoning (Kojonen and Johanson, 1999). SEM images of pyrite grains were used to identify the presence of zoning, mineral inclusions and pore spaces. Individual pyrites were selected from hand samples and analyzed based on texture and morphology (Fig. 5).

3.2. Pyrite textures

Petrographic observations and electron backscatter detection (EBSD) imaging were used to discriminate textural differences between the 5 generations of pyrite (Fig. 5). EBSD and orientation contrast were employed to determine if individual pyrite grains are complex aggregates or epitaxial overgrowths. This process was necessary due to the refractory nature of pyrite (Craig et al., 1998). Reddy and Hough (2013) showed that common trace

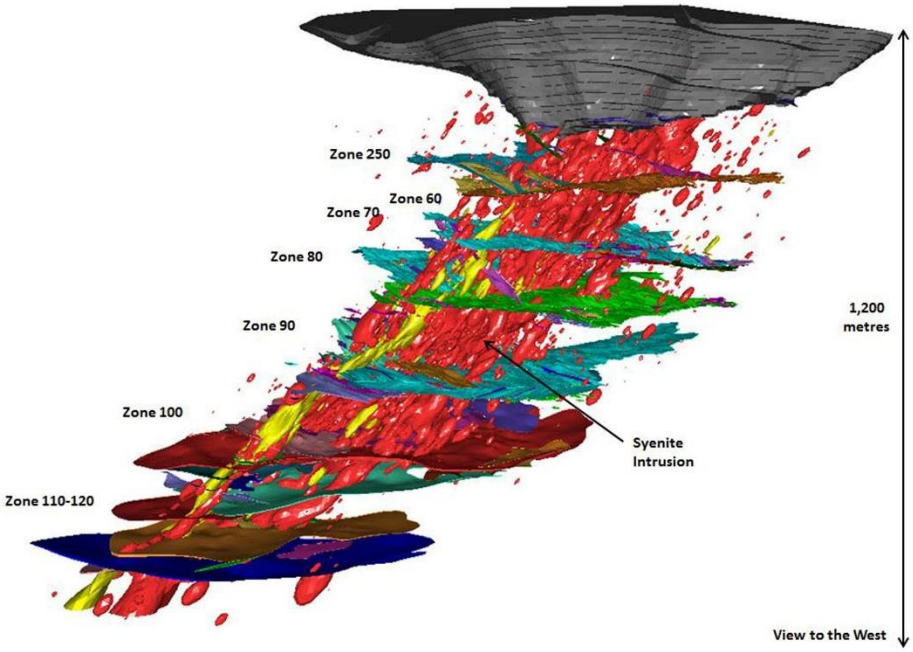

Fig. 2. 3D leapfrog model of the Wallaby gold lodes (horizontal trending sheets) and interlinking syenite structures shown as red and yellow bubbles with trend applied. The current outline of the pit is shown in grey above the gold lodes. Near horizontal wireframes are ore zones (as labelled), alternating colours include orange, brown, blue and green. (For interpretation of the references to colour in this figure legend, the reader is referred to the web version of this article.)

elements in pyrite (As, Ni, Co) could be remobilized by deformation altering diffusion pathways within pyrite lattices. All pyrite crystals imaged from Wallaby display no misorientations. Thus, Wallaby pyrite crystals can be considered as younging outward.

3.3. Sensitive high resolution ion-micro-probe- Stable isotope (SHRIMP-SI)

The Sensitive High Resolution Ion Microprobe- Stable Isotope (SHRIMP-SI) instrument was utilized to measure $\delta^{32}S$ and $\delta^{34}S$ on 3 μm spots in traverses across pyrite grains during a single 24 h period. This size of data point was employed after multiple sessions of larger (20 μm) points were analyzed. The larger points are broadly consistent to ratios from the smaller spots reported in this paper, hence we believe the small scale trends are accurate. Polished mounts were coated with aluminum to ensure conductivity. Total error was less than ±0.66 per mil (0.58 external error) for all pyrites analyzed. Wallaby data was collected during a 24 h SHRIMP-SI session using 2 detectors and acquiring data through 10 separate integrations lasting 10 s. Ruttan pyrite from Manitoba, Canada was used as the standard with a relatively homogeneous $\delta^{34}S$ value of 1.2‰ (Crowe and Vaughan, 1996). Each pyrite traverse was bracketed by 1–3 Ruttan analyses, yielding an average value of 1.02 per mil with a standard deviation of 0.86 (Appendix 2) All measurements are relative to Canyon Diablo Troilite (CDT).

3.4. Laser ablation-inductively coupled plasma-mass spectrometry (LA-ICPMS)

Individual pyrite grains were analyzed by 13 μm wide laser ablation traverses using the 'time slice' LA ICP-MS method outlined in Longerich et al. (1996a) measured by an Argilent 100 LA-ICPMS system at the Australian National University's Research School of Earth Sciences. This allowed special recognition of zoning within pyrite and enabled clear identification of inclusions. Elements analyzed with corresponding limit of detection (LOD) in brackets are as follows: Si^{29} (1942 ppm), Ca^{43} (1683 ppm), V^{51} (8 ppm), Mn^{55} (38 ppm), Ta^{181} (0.01 ppm), Pb^{208} (1 ppm), Ti^{49} (32 ppm), Co^{59} (7 ppm), Cu^{65} (8 ppm), Zn^{66} (6 ppm), As^{75} (5 ppm), Se^{77} (3 ppm), Se^{82} (4 ppm), Mo^{95} (2 ppm), Ag^{107} (0.10 ppm), Sn^{118} (1 ppm), Sb^{121} (3 ppm), Te^{125} (4 ppm), W^{182} (1 ppm), Pt^{195} (0.5 ppm), Au^{197} (1 ppm), Bi^{209} (0.10 ppm) and Ni^{60} (220 ppm). Pyrite samples were ablated using a Lambda Physik Laser ablation system operating at 193 nm, with an output energy of 45 mJ. The sample was initially transported in a H-He-Ar mixture to the Argilent Technologies 7700 series quadrupole ICP-MS. NIST SRM-610 and iron sulfide pellet MASS-1 were used as standards. Data was reduced and signals integrated using Iolite and Igor Pro (6.34A). They were used to minimize operator error during processing and to normalize the unknown samples to the known standards. The standards NIST SRM-610 and MASS-1 were compared to published values within the GeoRem database (Appendix 2) to ensure reasonable homogeneity in the standards for the elements analyzed. Average values and standard deviations of elements can be found in Appendix 2.

Traverses were selected to avoid inclusion-rich areas, however, small (under 10 s) spikes due to metal-sulfide inclusions were unavoidable. High intensity, short bursts of Cu, Pb and Ti were attributed to inclusions. All other elements followed Fe, indicating that these elements were from the pyrite crystal lattice rather than inclusions. Ratios were calculated between abundant trace elements found in the Wallaby pyrites for each generation. The ratios (specif-

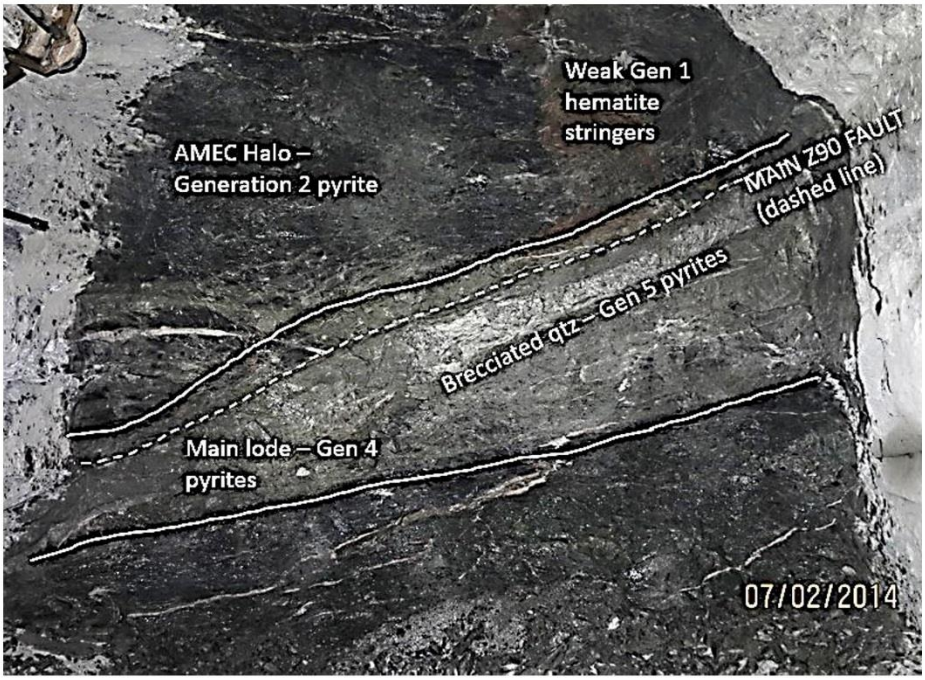

Fig. 3. Underground photo of exposure in Zone 90 North of the underground mining operations at Wallaby. Main mineralizing veins clearly cross-cut both hematite and later AMEC altered rock. Zone 90 North shows an alteration contact between Generation 1 and 2 pyrite and the mineral assemblages.

ically between As Ni, Sb, Cu and Te) are used to approximate chemical changes in each individual stage of pyrite, with the aim of determining whether there are any systematic changes between trace elements observed from early stage 1 pyrite to late stage 5 pyrite. Clear changes in chemistry synchronous with changes in sulfur isotope ratios would be linked to a change in redox conditions.

4. Results (Table 1 Summarizes characterizing features of each generation)

4.1. Pyrite Generation 1 (G1) porous euhedral pyrite with hematite

This first generation is the least abundant pyrite generation observed in hand specimens collected (Fig. 5A). It is the only generation found with hematite and is associated with the low-grade gold event (Fig. 6A). The crystals are porous and typically euhedral. The empty pores may be exposed fluid or gas inclusions or empty casts of minerals. Pyrite crystals of this generation are un-zoned. G1 pyrite crystals contain characteristically high median Sb (Fig. 6C), Ni (Fig. 6D), Ag (Fig. 7A), Cu (Fig. 7B), Co (Fig. 7C) and Zn (Fig. 7G). High Ca and Si are attributed to very small (<50 μm) silicate inclusions. Ti is attributed to rutile inclusions identified during EBSD. This generation contains no metallic inclusions (Fig. 5A). This generation has the greatest median Cu/Te ratio (Fig. 8C)

4.2. Pyrite Generation 2 (G2) porous anhedral inclusion-rich pyrite

Pyrite Generation 2 crystals are large (<2 mm), anhedral and porous. These pyrite crystals are associated with gold-poor conglomerate and the surrounding AMEC halo. Pyrite Generation 2 crystals contain chalcopyrite and magnetite inclusions up to 50 μm in width (Fig. 5B and C). The pseudomorphic texture of Pyrite Generation 2 crystals suggests formation by overgrowing/replacing chalcopyrite and/or magnetite grains. Typically, Pyrite Generation 2 crystals are characterized by low median concentrations of As (Fig. 6B), Ag (Fig. 7A) and Co (Fig. 7B). Generation 2 has the highest instances of Ni observed in all pyrite samples.

4.3. Pyrite Generation 3 (G3) euhedral-subhedral syenite related pyrite

Pyrite Generation 3 crystals are associated with the main syenite intrusion. This generation has no spatial relationship to

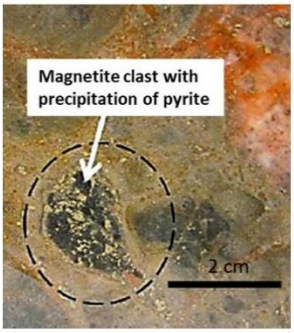

Fig. 4. Detrital magnetite containing pyrite clusters set in hematite-pyrite altered wall rock.

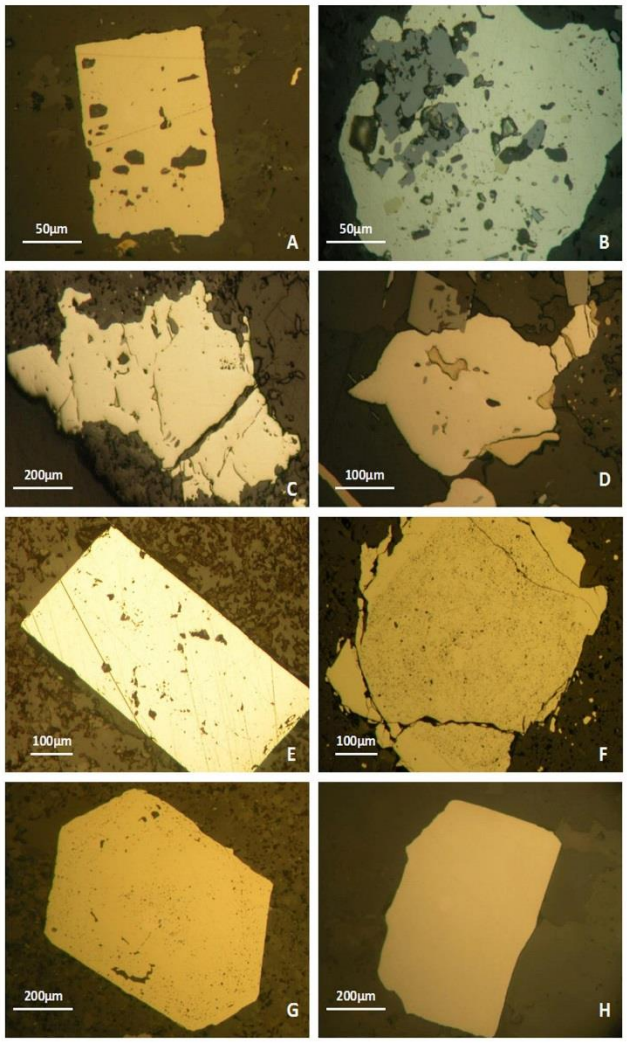

Fig. 5. Reflected light photomicrographs of pyrite grains from Wallaby; (A) Euhedral porous pyrite representative of Generation 1 (B) Generation 2 pyrites show pyrite overgrowths on magnetite and chalcopyrite, (C) Generation 2 pyrite with serrated boundaries and chalcopyrite inclusions, (D) Generation 2 pyrites with silicate filled cracks and chalcopyrite and galena inclusions, (E) Euhedral pyrite from a syenite dyke representative of Generation 3. (F) Generation 4 pyrite showing a porous core rimmed by inclusion-free overgrowths, (G) Generation 4 texturally zoned pyrite and (H) Generation 5 massive pyrite from a quartz-siderite vein.

magnetite and does not display pseudomorphous textures (Fig. 5E). In the pyrites observed, only pores and chalcopyrite inclusions were found. The euhedral pyrite crystals of this generation are characterized by the lowest median As concentrations (Fig. 6 B) and highest median Co (Fig. 7C). This generation is the first to exhibit 'high- grade gold' instances (Outlier observed in Fig. 6A). This generation is also characterized by numerous chalcopyrite inclusions. Pyrite Generation 3 crystals have the lowest As/Ni ratio.

4.4. Pyrite Generation 4 (G4) zoned euhedral pyrite in the high grade gold shear zone

This generation of large (<2 mm), texturally zoned, euhedral pyrite crystals (Fig. 5F and G) was only identified in veins (brecciated quartz) with high Au grades (Fig. 6A). The cores show porous and inclusion-rich textures. The dominant inclusions (in cores) include magnetite, chalcopyrite, pentlandite, pyrrhotite and rarely, galena, all less than 20 µm across. Euhedral overgrowths are

Table 1
Summary of distinguishing features of each pyrite generation and the characterizing trace element trends.

Generation	Crystal Habit	Inclusions	Major	Minor	Fe-O alteration	Au	Zoning
1	Euhedral	Porous Ca Ti Si inclusions	Sb, Ni, Ag, Cu, Co and Zn	Te	Hematite	Sub economic gold	No
2	Anhedral	Porous, Mt and Cpy inclusions	Ni and Mo	As Zn Ag Cu and Co	Magnetite	–	Weak
3	Euhedral	Porous and Cpy inclusions	Co	Au	Magnetite	Economic gold	Weak
4	Zoned Euhedral	Porous and inclusion rich core, clean rim	Au, Sb, Pb, Te elevated in cores	Ag and Zn	Magnetite	Economic gold	Strong Zoning
5	Euhedral	No inclusions	As		Magnetite	–	No

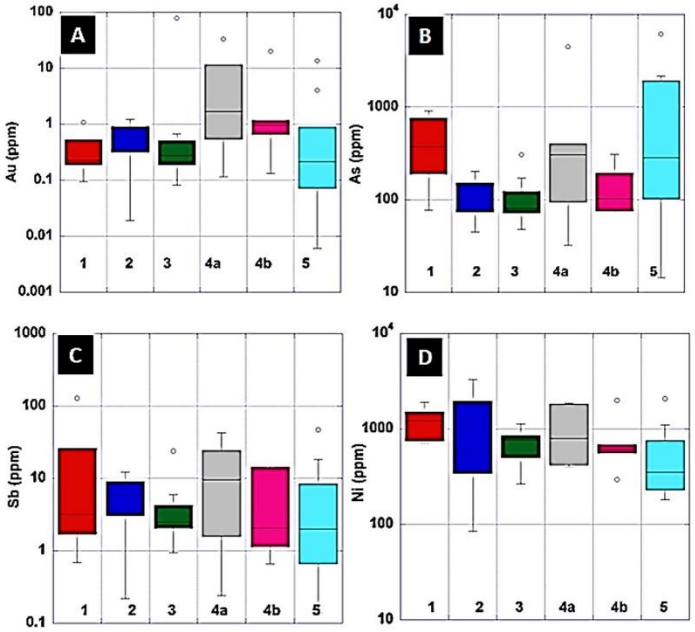

Fig. 6. Box and whisker plots of trace element concentrations for each pyrite generation (G1-G5). Red: Generation 1; Dark Blue: Generation 2; Green: Generation 3; Grey: Generation 4 cores; Pink: Generation 4 rims and Light Blue: Generation 5. (A) Au ppm (B) As ppm (C) Sb ppm (D) Ni ppm. (For interpretation of the references to colour in this figure legend, the reader is referred to the web version of this article.)

inclusion-free. Pyrite textures suggest overgrowth and/or replacement of magnetite.

Chemical zoning, although subtle in Pyrite Generations 2, 3 and 5 (Fig. 9), mimics bleached visual and textural relationships. Pyrite Generation 4 crystals can be separated into core and rim by As and Ni concentrations, with rims containing lower Ni and As concentrations (Figs. 6B and D and 8A). Thus, this generation of pyrite can be separated into two groups:

Cores (4a): Isotopically and texturally distinct cores are porous and contain abundant inclusions. The cores are characterized by the highest median Au (Fig. 6A), Sb (Fig. 6C), Pb (Fig. 7D) and Te concentration (Fig. 7F). The Au and Te is present in telluride inclusions. The gold contents are similar to Pyrite Generation 3. Ni is elevated in the cores and the Se^{77}/Se^{82} is marginally higher (Fig. 10), suggesting minor fractionation associated with the gold event.

Rims (4b): Rims are inclusion-free. These rims are characterized by the depletion of most trace elements found in adjacent cores (Figs. 6 and 7). As, Au, Cu, Co, Ni, Zn, Sb, Pb, Ag and Te compared to Group 1 cores (Figs. 6A–D and 7A–D, F and G). Rims have the lowest median As/Sb ratio in the pyrite generations (Fig. 8B).

4.5. Pyrite Generation 5 (G5) euhedral vein related hydrothermal pyrite

This generation consists of pyrite crystals in alteration selvages of hydrothermal quartz-carbonate veins. Pyrite Generation 5 textures are similar to the previous high-grade Au pyrites rims (4b). These pyrites contain no pores, inclusions or fractures (Fig. 5H). They are characterized by the lowest median Au (Fig. 6A), Sb (Fig. 6C), Ni (Fig. 6C), Ag (Fig. 7A), Cu (Fig. 7B), Bi (Fig. 7E), Te (Fig. 7F) and Zn (Fig. 7G This generation has the highest median As/Ni (Fig. 8A), As/Sb (Fig. 8B) and As/Bi (Fig. 8D) ratios.

W and Pb behave similarly in Pyrite Generations 3 and 4a due to micro-inclusions within pyrite (Fig. 5H). Pyrite Generation 4b and 5 crystals are free of inclusions and low in W and Pb (Fig. 11).

There is a gradual depletion in Zn, Ag, Cu, Co, Bi and Sb from Pyrite Generation 1 to Pyrite Generation 5 within the Wallaby vein

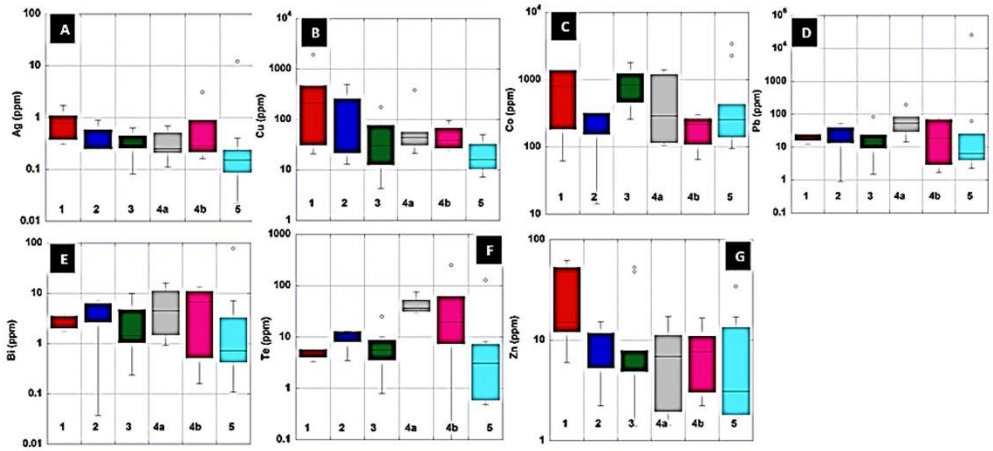

Fig. 7. Box and whisker plots of trace element concentrations for each pyrite generation (G1-G5). Red: Generation 1; Dark Blue: Generation 2; Green: Generation 3; Grey: Generation 4 cores; Pink: Generation 4 rims and Light Blue: Generation 5. (A) Ag ppm (B) Cu ppm (C) Co ppm (D) Pb ppm (E) Bi ppm (F) Te ppm (G) Zn ppm. (For interpretation of the references to colour in this figure legend, the reader is referred to the web version of this article.)

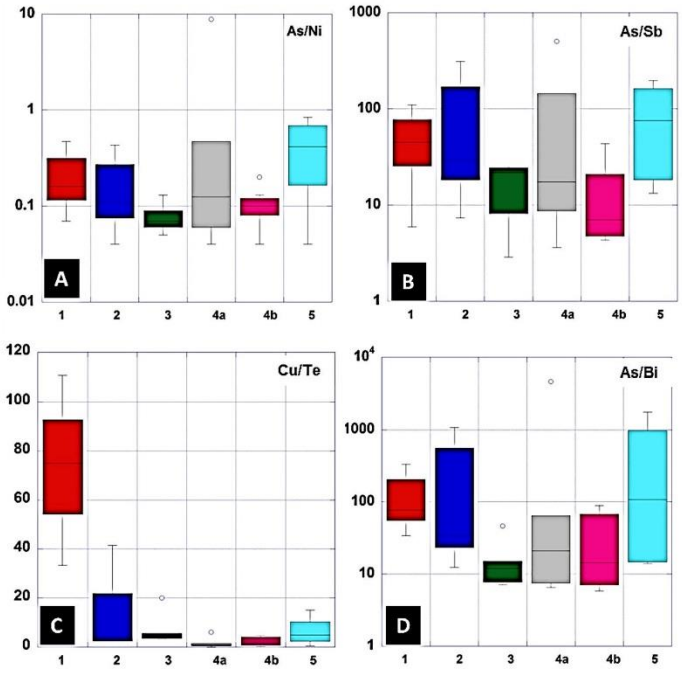

Fig. 8. Box and whisker plots of trace element concentration ratios for each pyrite generation (G1-G5). Red: Generation 1; Dark Blue: Generation 2; Green: Generation 3; Grey: Generation 4 cores; Pink: Generation 4 rims and Light Blue: Generation (A) As vs. Ni (B) As vs. Sb (C) Cu vs. Te (D) As vs. Bi. (For interpretation of the references to colour in this figure legend, the reader is referred to the web version of this article.)

sequence (Fig. 6C and Fig. 7). In Pyrite Generations 2, 3 and 4a, Sb and Bi concentrations show a strong correlation (R^2 = 0.96, 0.73, 0.44 respectively). This gradual change coincides with gold-telluride deposition and an increase in As/Ni (Fig. 8A). High Te coincides with high As values in Pyrite Generations 3 and 4a and b (Figs. 6B and 7F).

4.6. Sensitive high-resolution ion-micro-probe (SHRIMP) (Appendix 2)

Sulfur isotope masses 32 and 34 were measured across the pyrite sequence at Wallaby. Significant changes in this ratio are observed on a 3 μm scale across individual pyrite grains and throughout the fluid history of the Wallaby deposit. Sulfur isotope ratios within pyrite generations at Wallaby range from −7.33 to +9.26 $\delta^{34}S$ (Fig. 12). Each generation yields a specific range (from core to rim) of: Pyrite Generation 1 from −7.33 to −1.99 (more negative in cores); Pyrite Generation 2 from −5.5 to +3.85; Pyrite Generation 3 from −0.21 to +6.86; Pyrite Generation 4 from 4 to 8.61 (more positive towards rims); Pyrite Generation 5 from 5.27 to 9.26.

5. Discussion

5.1. Pyrite sulfur isotope patterns

Sulfur isotope analyses of individual pyrite display a gradual enrichment in $\delta^{34}S$ from core to rim. Pyrite Generation 1 crystals have the most negative sulfur isotopic values of the entire series. Subsequent generations yield gradually increasing $\delta^{34}S$, up to +9.26 in the last generation. Rye and Ohmoto (1974) established the major controls on $\delta^{34}S$ to be temperature, pH and oxygen fugacity. The Wallaby Gold Deposit is estimated to have formed within the temperature range 250–350 °C and a narrow pH range (Hodkiewicz et al., 2009; Salier et al., 2004), both of which should not affect sulfur isotopic composition. The change in sulfur isotopes is most likely due to a reduction in oxygen fugacity (Fig. 13). This was suggested generally from mineralogical observations in drill core, with hematite-bearing veins crosscut by later magnetite-bearing veins. This was shown to be a change in redox between Pyrite Generation 1 and Pyrite Generation 2 veins where hematite is lost and magnetite gained and is reflected in Fig. 12. Thus, once in the magnetite field, subtle changes in fO_2 were monitored by changes in trace metals and sulfur isotopes, as shown by Ohmoto (1972) and mentioned previously (Fig. 13). The change in δS^{34} is accompanied by a marked increase in Au (Fig. 6A) and systematic trace element changes (Fig. 14). The continuous delivery

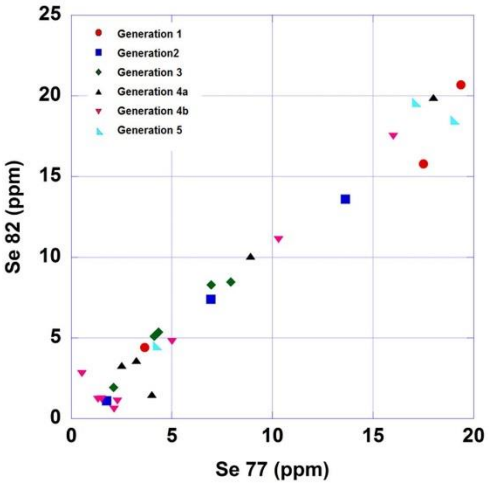

Fig. 10. Se^{77} vs. Se^{82} displaying minor fractionation in Generation 3–4 pyrite. Red: Generation 1; Dark Blue: Generation 2; Green: Generation 3; Grey: Generation 4 cores; Pink: Generation 4 rims; Light Blue: Generation 5. (For interpretation of the references to colour in this figure legend, the reader is referred to the web version of this article.)

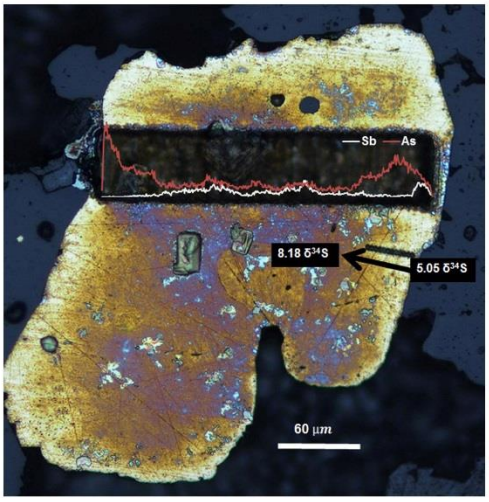

Fig. 9. Group 5 NaOCl-stained pyrite under reflected light. Laser traverse of Sb and As counts per second overlain in red and white respectively. 3 μm SHRIMP-SI traverse shown with an arrow and the change of sulfur isotope ratio across the traverse are indicated. Sample WAL A3-1. (For interpretation of the references to colour in this figure legend, the reader is referred to the web version of this article.)

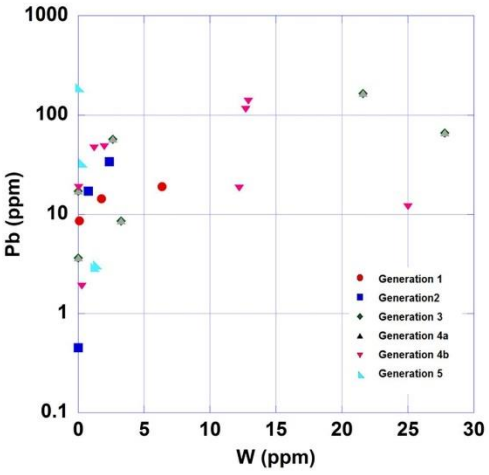

Fig. 11. Variation plot Pb vs. W of each pyrite generation. Red: Generation 1; Dark Blue: Generation 2; Green: Generation 3; Grey: Generation 4 cores; Pink: Generation 4 rims and Light Blue: Generation 5. (For interpretation of the references to colour in this figure legend, the reader is referred to the web version of this article.)

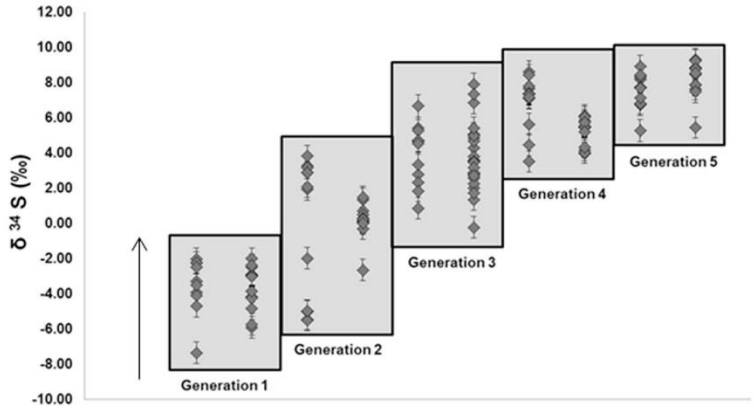

Fig. 12. 3-µm spot traverses (Rim to Core in direction of arrow) of Wallaby pyrite $\delta^{34}S‰$. Overlapping is seen between generations of pyrite. All errors < 0.6 per mil.

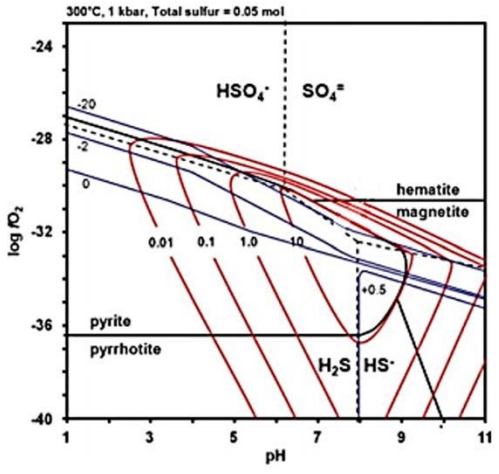

Fig. 13. fO_2 vs. pH plot with contoured sulfur isotopes (blue lines) and gold solubility (red lines displaying 0.01, 0.1, 1.0 and 10.0 ppm). Note that the most negative isotope values are found at high fO_2. Modified from Hodkiewicz et al. (2009) after Seward (1973). Conditions set at 300 °C, 1 kbar, $\Sigma S = 0.05$ mol, $mNa^+ = 1$, $mK^+ = 0.1$ and $MCa^{2+} = 0.01$. Note that Au solubility contours suggest oxidation as an excellent trigger for gold deposition (i.e. steepness of contours), while reduction is a much more gradual process. (For interpretation of the references to colour in this figure legend, the reader is referred to the web version of this article.)

of fluid into Wallaby during the formation of each pyrite –bearing generation has resulted in a progressive alteration of the iron enriched conglomerate mentioned previously. We suggest that this continual change in fluid chemistry has prolonged the system reaching equilibrium and so, is reflected by the systematic changes in trace elements observed in the pyrites. This is a larger range of sulfur values for discrete pyrite grains, measured on a much finer analytical scale than has been previously published (Salier et al., 2005; Hodkiewicz et al., 2009).

Light isotopic ratios were only measured in Pyrite Generation 1 (hematite associated) crystals. While the range between Pyrite Generations 1 and Generation 2 is large there are similarities between the rims of Pyrite Generation 1 crystals and the cores of Pyrite Generation 2 crystals. This is observed as a broad trend across all subsequent pyrite sulfur isotopes further supporting that each generation of pyrite is overgrown by a constantly evolving fluid.

5.2. Pyrite trace element variations

The most notable changes from Pyrite Generation 1 to Pyrite Generation 5 crystals are increases in As and Te concentrations (Figs. 6A and 7F), and gradual decreases in Ag, Cu, Co, Bi, Ni, Sb and Zn (Figs. 6C and D and 7A–C, E and G). These sequential changes mirror the enrichment of $\delta^{34}S$ (Fig. 13). As/Ni and As/Bi show negative correlation trends (Fig. 8A and D). This suggests that the cause of coupled enrichment/ depletions of trace elements in the pyrite is controlling the ion substitution in the pyrite lattice. The oxidizing conditions attending the first generation caused enrichment in trace elements that support Fe^{2+} substitution dominance (Reich et al., 2005). Thus Pyrite Generation 1 crystals have higher Ni and Co concentrations than subsequent generations. Under more reduced conditions (Generation 2–5) gradual enrichment in trace elements that replace the S^{-2} atoms such as As and Sb (Reich et al., 2005) are seen. These sequential geochemical changes were the result of larger geologic processes such as wall-rock reactions consuming oxygen or desulfidation consuming sulfur. As the fluid proceeded through permeable zones, progressive wallrock alteration produced an evolving mineralized sequence. This fluid – wall rock interaction established the conditions required to destabilize Au-bisulfide complexes and trigger gold deposition. This is supported by the trace element and sulfur isotope changes observed. Earlier suggestions that the AMEC alteration halo was formed during metasomatism associated with the emplacement of the syenite intrusion (Coggon, 2003; Salier et al., 2004) are not supported by sulfur isotope and trace element trends, since there is no distinct sulfur isotope change between the altered and unaltered conglomerate. The presence of magnetite inter-grown with Pyrite Generation 2 crystals suggests that the fluid was reduced relative to Pyrite Generation 1. This generation is significantly higher in granophile elements such as Bi and Pb (Fig. 7D and E), which could have been sourced from the surrounding host rock. It has been observed by Salier et al. (2004) that the 600 m wide AMEC halo is too large relative to the size of the intrusion, hence it occurred before the syenite intrusions.

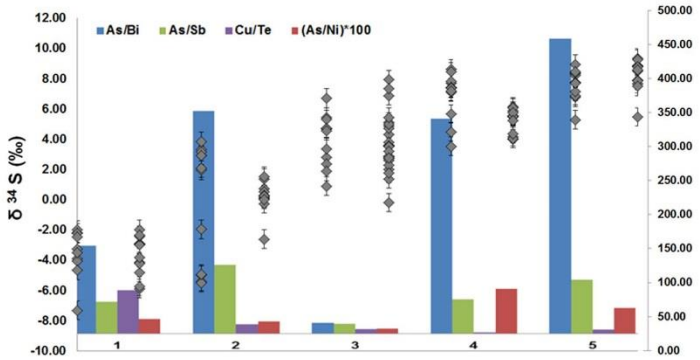

Fig. 14. Sulfur isotope ratios (Left axis) of Generation 1–5 pyrites (Grey symbols with error bars). Trace element ratio averages for each pyrite generation as a column graph (X-axis).

5.3. The role of redox in gold deposition at Wallaby

Small spot sulfur analyses and laser traverses from this study have established a concise story of ore deposition at Wallaby. Studies by Stoltze et al. (2006), Salier et al. (2004) and Miller (2006) and Wall (unpublished Placer Dome Report, 2001) suggested that the formation of the gold deposit commenced with the intrusion of the alkaline suite (monzonite-syenite-carbonatite) during extension. This established the first low-grade gold (<2.0 g/T) event deposited from an oxidized fluid (Miller, 2006). Salier et al. (2004) suggested that iron-enriched zones became increasingly permeable and favorable for gold deposition during this event. The early stage alteration due to magmatism was initially thought responsible for the significant gold endowment at Wallaby, however, the late stage, evolved fluid deposited the bulk of the economic gold observed.

The initial ore-forming event was followed by fluid reduction during a structural event that formed the horizontal lode gold shears. This series of stacked gold lodes contain high gold grades associated with the late stage reduced hydrothermal fluid.

The $\delta^{34}S$ analyses from this study combined and the trace element pattern in pyrites suggest that desulfidation was the predominant driver for significant gold deposition within the Wallaby Gold Deposit. Negative $\delta^{34}S$ isotope values are common in oxidizing environments, such as the Wallaby Pyrite Generation 1 crystals. This is due to sulfur preferentially bonding with O_2, leaving the heavier isotopes in the fluid (Rye and Ohmoto, 1974). Determining which oxidized sulfur species predominated in the Pyrite Generation 1 crystals is difficult due to pH estimation (5.5) and requires further study of mineral assemblages however, these pyrite crystals most likely formed from a highly oxidized fluid rich in HSO_4^- and SO_4^{-2}. This is consistent with deposition of the economic gold occurring later than previously established (Fig. 15).

One source for oxidized sulfur species is felsic intrusions; however there is no current research suggesting that there are such intrusions in the Yilgarn. Walshe et al. (2003) suggest that mixing of a deeply derived, relatively oxidized fluid from a distal source and a proximal, locally reduced magmatic fluid could trigger gold deposition. This fluid mixing is unlikely given that Pyrite Generation 1 crystals have high concentrations of granophile elements. The more realistic mechanism for gold deposition is desulfidation due to the relative abundance of Fe oxide minerals in the Wallaby host conglomerate. The high Fe-mafic conglomerate at Wallaby provided an excellent source for Fe-sulfide deposition favorable for gold deposition. The equation below established gold deposition via ferromagnesian minerals enabling pyrite and gold reduction.

Rye and Ohmoto (1974) showed that $\delta^{34}S$ fractionation occurs as a function of temperature, desulfidation and redox. Temperature changes across orogenic deposits in the Laverton Province are

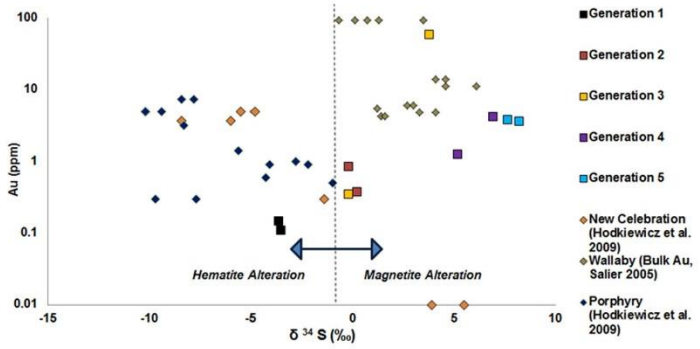

Fig. 15. Average $\delta^{34}S$ versus average gold concentrations for Wallaby pyrites (squares) and overlain results from previous studies (diamonds) (Salier et al., 2005; Hodkiewicz et al., 2009). Black line and blue arrows depict visual mineralogy boundary as a potential phase change which is representative of the redox change responsible for the most significant gold deposition at the Wallaby Gold Deposit. (For interpretation of the references to colour in this figure legend, the reader is referred to the web version of this article.)

considered minimal (Salier et al., 2005) and fluids at Wallaby are estimated to have contained 3–6% H_2O-CO_2-NaCl or 0.05–3*m* CO_2 (Salier et al., 2004). Orogenic fluids are generally described as near-neutral (Hodkiewicz et al., 2009), with Goldfarb and Groves (2015) estimating the pH of "typical" orogenic gold fluid to be 5.5 after their work using CO_2 fluid inclusion data. Thus, if temperature and pH do not vary significantly, the main control in such environments is fO_2. As demonstrated in Fig. 12 the sulfur isotope contours vary with oxygen fugacity. Note that at low to moderate pH, oxidation drives $\delta^{34}S$ to negative values, and the most negative sulfur is found in the hematite field. At Wallaby we see a clear change between the first stage (hematite-bearing) and all subsequent generations (magnetite-bearing). After this step change in redox, fO_2 is no longer reflected by mineral buffers and must be monitored via trace element and sulfur isotopic analyses.

$$Au + H_2S(aq) + HS^- = Au(HS)_2^- + 0.5H_2(g)$$ (Shenberger and Barnes,1989)

At Wallaby, pH and temperature are considered unimportant while the fluid interaction with the host rock would dramatically change the oxygen and sulfur fugacity of the system. As the mineral assemblages observed at Wallaby across all generations show no indication of highly acidic or alkaline fluids the authors believe the estimation of pH of the greenstone terrain to be realistic (Goldfarb and Groves, 2015). The desulfidation occurred during the gradual redox change and is considered responsible for gold deposition. This well-established scenario is represented in Figs. 14 and 15 and is supported by the modeled Au-solubility based on Au in the thio-complex ($AuHS_2^-$) by Shenberger and Barnes (1989) and Hodkiewicz et al. (2009); previously discussed in Fig. 13 displays Au solubility contours suggesting that oxidation is an excellent trigger for Au deposition. However, the authors believe that gradual reduction alone cannot account for the significant gold endowment. Thus concluding that desulfidation in parallel with gradual reduction was the cause of economic gold deposition at Wallaby.

5.4. Consequences for Wallaby

The Au is closely associated with Te, Bi and irregular Se concentrations. The Te and Bi appear to have been transported within the oxidized fluid at Wallaby and precipitated due to reduction, as suggested by McPhail (1995) and Skirrow and Walshe (2002). High arsenic concentrations, which coincide with gold also precipitated due to reduction, as demonstrated by Pokrovski et al. (2002). It seems unlikely that the trace element and sulfur isotope pattern seen here would eventuate if the fluid was derived from more than one source. The results of this study indicate that the Wallaby Gold Deposit formed during the evolution of an originally oxidized fluid that under changing structural conditions (regional compression) underwent continual reaction with the Fe rich-mafic wallrock.

The heavier sulfur isotopes of the gold-bearing Pyrite Generation 3–4 crystals all display an increase in Se^{77}/Se^{82}. This may be indicative of a fractionation process related to redox during gold deposition. This requires further research as Se could be elevated in multiple ways. It should also be noted while gold within pyrites decreases in Pyrite Generations 4 and 5, native gold in associated veins is abundant. This suggests that the fluid completed reduction, triggering Au deposition.

Selenium has been shown to be soluble in oxidized fluids and deposited via reduction (Johnson et al., 1999). This explains the elevated Se concentrations during gold deposition but not Se isotopic fractionation. Selenium preferentially partitions into chalcopyrite (Yamamoto et al., 1983), which could account for the lower Se values in earlier chalcopyrite- bearing pyrite generations at Wallaby. The decrease in Se^{77}/Se^{82} and the decrease in Te and Au in Pyrite Generation 5 could reflect that reduction was complete. The slight elevation in elements that predominated prior to gold deposition such as Co, Pb and the Se isotopes also support this.

5.5. Comparison with other mines in the St Ives region

This study shows two distinct gold events characterized by light and heavy sulfur isotopic ratios. The evolution is consistent across broad geochemical and isotopic trends, which are best supported by the distinct zoning seen in Pyrite Generation 4 crystals. Where previous models supported gold deposition from oxidized fluids (Salier et al., 2005; Hodkiewicz et al., 2009), this study supports the main driver for gold deposition as desulfidation (Fig. 15). Pyrite Generation 1 crystals associated with the early low-gold event have similar SHRIMP–SI values to those previously published by Hodkiewicz et al. (2009) and Salier et al. (2005) for the Wallaby, Porphyry and New Celebration deposits. Pyrite Generation 2, 3, 4 and 5 crystals from Wallaby analyzed by small SHRIMP-SI spots returned comparatively reduced values. Pyrtie Generation 1 crystals analyzed here have similar $\delta^{34}S$ compared to the Porphyry and New Celebration deposits measured by Salier et al. (2005) and Hodkiewicz et al. (2009). Generations 2–5 from Wallaby show a distinctly more positive $\delta^{34}S$, as seen on Figs. 12 and 15 associated with an increase in gold grade. The results reported here support the finding of Salier et al. (2005) that the significant gold event was associated fluid reduction.

This study differs from previous work by suggesting that the AMEC halo was in place before the syenite intrusion, established via paragenetic relationships. This is supported by the significant change in Pyrite Generation 3 chemistry and the overlapping but increasingly positive sulfur isotopes. Secondly, this work places the first low gold, hematite-associated event before the formation of the AMEC.

The change in oxygen fugacity, as recorded by the change from hematite to magnetite, is accompanied by a change in As/Ni (and other ratios) reflecting reduction. Generation 1 hematite associated pyrite has As/Ni of 0.24. Generations 2, 3, and 4a have As/Ni ratios of 0.20, 0.08 and 1.60, respectively (Fig. 8A). The highest ratio (1.6) is from Pyrite Generation 4 crystals, which also contain the highest concentrations of gold. The redox change observed at Wallaby is characterized by a change from hematite to magnetite. The final pyrite generation exhibits As/Ni of 0.43. Thus, by Pyrite Generation 5 the fluid was reduced. The use of As/Ni in pyrite as a redox sensor in an evolving fluid is novel. This may provide a 'reduction' indicator for redox-influenced gold deposits. Further work should be conducted to strengthen this relationship over a range of gold deposits from the mineral to deposit scale.

5.6. Global context

Structurally controlled fluid flow through Fe-rich conglomerates at Wallaby deposited pyrite and magnetite, effectively stripping sulfur and oxygen to reduce the fluid and trigger gold deposition. This is not the only way to trigger gold deposition. For instance, gold deposition at Porgera, PNG and at the Bendigo Goldfields of Australia appears to have been quite different. These deposits appear to have formed via fault-valve processes (Sibson, 1992; Cox et al., 1995; Peterson and Mavrogenes, 2014) whereby huge pressure variations drove gold deposition. Recently, Weatherley and Henley (2013) showed that during fault rupture pressure drops from lithostatic or hydrostatic pressures to near 0 bars in seconds. This causes major changes in fluid supply, from wall-rock buffered pre-rupture to fluid buffered during or after failure. At Porgera, Peterson and Mavrogenes (2014) interpret alternating zones within individual pyrite crystals as a consequence of this process. Switching between oxidized magmatic fluids concen-

trated in Sb, Pb, Ag, As, and Au, and relatively reduced regional fluids containing only Ni and Co. Porgera, a predominantly magmatically driven fault valve system contrasts strongly with the Bendigo deposit where regional fluids were reduced by black shale but overall fluid pressures remained high (Cox et al., 1995). Both Porgera and Bendigo deposits produced Co-Ni rich pyrites from the reduced source fluids and trace element rich fluids from the orogenic fluids. No obvious switching is seen at Bendigo, although the outer rims of pyrite are concentrated in Au-As (Thomas et al., 2011). Thus, gold deposit styles can be delineated by pyrite grains alone. At Wallaby, gradual changes reflect an evolving fluid while fault-valve systems involving either magmatic (Porgera) or regional (Bendigo) fluids can be inferred.

Banded pyrite crystals from Sangihe Island, interpreted by King et al. (2014) as formed by reduction of highly oxidized gases (still above the hm-mt buffer). Alternating zones of high Au, Cu and Te are observed to over-grow pyrite crystals during repetitive input of gas. This contrasts strongly to Wallaby as the economic Au in all generations at Sangihe exhibits very low As concentrations. King et al. (2014) confirm that redox affects substitution, particularly As + Au replacing Fe ions in the pyrite structure. Perhaps the adsorption of Au and Te is controlled primarily through a relative reduction of the ore carrying gas and the anomalous concentrations of Cu (up to 6 wt%) at Sangihe are due to the same relative reduction but in a highly oxidized environment. Pokrovski et al. (2005) showed that in the presence of sulfur, Cu can form stable complexes enabling magmatic-gas transport.

Raiswell and Plant (1980) observed enrichment in redox sensitive elements such as Cu, Ni, Zn and Co in sedimentary pyrites formed in carbonate concretions in the Upper Lias of Yorkshire (England) compared with those in the black shale host rock. They linked changes in pyrite trace elements to Fe-availability and suggested a direct link to source, where high concentrations of As signal an external source. The trace elements observed in Generation 1 pyrites at Wallaby and the changes in morphology across the entire paragenesis are very similar and support relative As concentration as a proxy for ore-fluid source.

6. Conclusion

Trace element trends were identified in successive pyrite generations of the Wallaby Gold Deposit, WA. The pyrites were characterized by optical mineralogy, LA-ICP-MS and SHRIMP-SI on an extremely small scale, which the authors believe has not been observed previously. Large-scale geological processes are reflected on the microscopic scale. This study shows that pyrite can be used to track changes in trace element concentrations that reflect a process of progressive reduction. Trace elements of note include As, Bi, Cu, Ni, Co and Pb.

The results of this study help explain the mechanisms that controlled native gold deposition vs. disseminated gold deposition within sulfide at the Wallaby Gold Deposit. The geochemical and isotopic changes observed are consistent with textural zoning within each paragenetically defined generation of pyrite and can be used to define discrete groups.

Systematic changes in sulfur isotopes and trace elements known to be redox sensitive, in particular, As, Ni, Sb and Co within the successive pyrite generations support redox change as the dominant driver for ore deposition. Elemental ratios, particularly As/Ni, support a change in substitution in pyrite from cation dominant under oxidizing conditions to anion dominant under reducing conditions. This has wider exploration implications for Archean greenstone belt gold exploration. In particular these trends can be used to delineate tectonic gold deposit styles i.e. magmatic vs. regional fluid sourced.

While the hematite associated Pyrite Generation 1 crystals contain sub-economic gold, a clear change in oxygen fugacity is observed between Pyrite Generations 1 and 2. This is seen mineralogically (hematite to magnetite), and in trace element and sulfur isotope abundances. This reduction continued systematically and was responsible for the economic endowment of both Au and Te observed predominantly in Pyrite Generations 3 and 4 crystals. Pyrite Generation 4 and 5 rims contain less gold because fluid reduction was complete. Thus, while desulfidation occurred at Wallaby, the authors ascribe the dominant control on $\delta^{34}S$ to be gradual reduction, which is responsible for the main gold event. This differs from previously established triggers for gold deposition at Wallaby.

Acknowledgements

We thank David Craw and Artur Deditius for constructive revisions. Their time and effort was greatly appreciated. We would also like to thank the technical staff at ANU for assistance during sample processing and analysis.

Appendix 1: Samples and locations WB1274UD (B3) B)WB0801CD (A3) C) WB0801CD (A1,3,4,5,9,10)

Table 1. Sample locations, descriptions and bulk Au assay data.

Sample	Hole/ location	Interval (m)	Rock type/alteration	Au assay
A1	WB0801CD	159.22–159.42	meta-basaltic conglomerate with magnetite-actinolite alteration	3.86 ppm
A3	WB0801CD	188.2–188.51	Sheared conglomerate with hematite-dolomite-sericite-albite alteration	1.36 ppm
A4	WB0801CD	334.76–334.88	Greenschist facies chlorite-calcite conglomerate	0.02 ppm
A5	WB0801CD	481.22–481.38 m	Brecciated quartz veining and gold mineralisation in dolomite-sericite--albite alteration	11.63 ppm
A10	WB0801CD	692.91–693.21 m	Hematite-dolomite-albite-sericite altered sheared conglomerate	1.24 ppm
B3	WB1274UD	27.6–27.73 m	High grade gold mineralisation with dolomite-albite-sericite alteration and associated quartz veining	6.58 ppm
GSZ80X	Z80W	Grab sample	Boundary between hematite altered Syenite and moderate grade py-ser-dol-ab mineralisation	4–5 ppm
GSZ70	Z70W 1002	Grab sample	–	2–3 ppm

(*continued on next page*)

Appendix 1: Samples and locations WB1274UD (B3) B)WB0801CD (A3) C) WB0801CD (A1,3,4,5,9,10) (*continued*)

Sample	Hole/ location	Interval (m)	Rock type/alteration	Au assay
A9	SL1 WB0801CD	691.84–691.93 m	Hematite-altered syenite	0.41 ppm

Appendix 2: Results

Table 1. SHRIMP results from 24 h session, shows standards and samples analyzed with total error.

Title	Date	Time	34S/32S	95%T_err	34S/32S drift corrected	Ratio Permil	StdErr_95%T	Total error
RUTTAN-6	22/09/2014	11:23 AM	0.04	8.30E−06	0.04	0.93	0.19	0.61
RUTTAN-7	22/09/2014	11:32 AM	0.04	9.00E−06	0.04	1.61	0.20	0.62
RUTTAN-8	22/09/2014	11:44 AM	0.04	7.05E−06	0.04	1.24	0.16	0.60
WAL-A10-1.1.1	22/09/2014	11:56 AM	0.04	9.38E−06	0.04	2.90	0.21	0.62
WAL-A10-1.1.2	22/09/2014	12:04 PM	0.04	8.92E−06	0.04	1.94	0.20	0.61
WAL-A10-1.1.3	22/09/2014	12:12 PM	0.04	9.21E−06	0.04	2.09	0.21	0.62
WAL-A10-1.1.4	22/09/2014	12:20 PM	0.04	7.36E−06	0.04	3.29	0.17	0.60
WAL-A10-1.1.5	22/09/2014	12:28 PM	0.04	8.40E−06	0.04	3.17	0.19	0.61
WAL-A10-1.1.6	22/09/2014	12:36 PM	0.04	6.10E−06	0.04	3.85	0.14	0.60
WAL-A10-1.1.7	22/09/2014	12:44 PM	0.04	6.47E−06	0.04	2.91	0.15	0.60
WAL-A10-1.1.8	22/09/2014	12:52 PM	0.04	8.61E−06	0.04	−1.98	0.20	0.61
WAL-A10-1.1.9	22/09/2014	1:00 PM	0.04	1.15E−05	0.04	−4.96	0.26	0.64
WAL-A10-1.1.10	22/09/2014	1:08 PM	0.04	7.92E−06	0.04	−5.00	0.18	0.61
WAL-A10-1.1.11	22/09/2014	1:16 PM	0.04	6.99E−06	0.04	−5.44	0.16	0.60
WAL-A10-1.1.12	22/09/2014	1:24 PM	0.04	7.07E−06	0.04	−5.50	0.16	0.60
RUTTAN-8	22/09/2014	1:38 PM	0.04	8.95E−06	0.04	1.41	0.20	0.61
WAL-A10-2.1.1	22/09/2014	1:49 PM	0.04	7.88E−06	0.04	4.15	0.18	0.61
WAL-A10-2.1.2	22/09/2014	1:57 PM	0.04	9.10E−06	0.04	5.46	0.21	0.62
WAL-A10-2.1.3	22/09/2014	2:05 PM	0.04	9.76E−06	0.04	6.12	0.22	0.62
WAL-A10-2.1.4	22/09/2014	2:13 PM	0.04	9.29E−06	0.04	5.53	0.21	0.62
WAL-A10-2.1.5	22/09/2014	2:21 PM	0.04	8.10E−06	0.04	5.49	0.18	0.61
WAL-A10-2.1.6	22/09/2014	2:29 PM	0.04	8.08E−06	0.04	5.85	0.18	0.61
WAL-A10-2.1.7	22/09/2014	2:37 PM	0.04	6.62E−06	0.04	6.05	0.15	0.60
WAL-A10-2.1.8	22/09/2014	2:45 PM	0.04	7.49E−06	0.04	5.74	0.17	0.60
WAL-A10-2.1.9	22/09/2014	2:53 PM	0.04	8.63E−06	0.04	5.23	0.20	0.61
WAL-A10-2.1.10	22/09/2014	3:00 PM	0.04	6.61E−06	0.04	4.00	0.15	0.60
WAL-A10-2.1.11	22/09/2014	3:08 PM	0.04	7.03E−06	0.04	4.01	0.16	0.60
WAL-A10-2.1.12	22/09/2014	3:16 PM	0.04	7.90E−06	0.04	4.35	0.18	0.61
RUTTAN-9	22/09/2014	3:28 PM	0.04	7.96E−06	0.04	0.99	0.18	0.61
RUTTAN-10	22/09/2014	3:39 PM	0.04	8.05E−06	0.04	1.40	0.18	0.61
WAL-A3-1.1.1	22/09/2014	3:51 PM	0.04	1.03E−05	0.04	5.27	0.23	0.62
WAL-A3-1.1.2	22/09/2014	3:59 PM	0.04	1.20E−05	0.04	6.77	0.27	0.64
WAL-A3-1.1.3	22/09/2014	4:07 PM	0.04	7.93E−06	0.04	6.84	0.18	0.61
WAL-A3-1.1.4	22/09/2014	4:15 PM	0.04	1.03E−05	0.04	7.74	0.23	0.63
WAL-A3-1.1.5	22/09/2014	4:23 PM	0.04	8.70E−06	0.04	8.35	0.20	0.61
WAL-A3-1.1.6	22/09/2014	4:31 PM	0.04	1.03E−05	0.04	8.95	0.23	0.62
WAL-A3-1.1.7	22/09/2014	4:38 PM	0.04	8.50E−06	0.04	8.45	0.19	0.61
WAL-A3-1.1.8	22/09/2014	4:46 PM	0.04	7.92E−06	0.04	7.14	0.18	0.61
WAL-A3-1.1.9	22/09/2014	4:54 PM	0.04	1.07E−05	0.04	7.70	0.24	0.63
WAL-A3-1.1.10	22/09/2014	5:02 PM	0.04	1.03E−05	0.04	7.75	0.23	0.63
WAL-A3-1.1.11	22/09/2014	5:10 PM	0.04	9.04E−06	0.04	8.32	0.20	0.61
WAL-A3-1.1.12	22/09/2014	5:18 PM	0.04	7.61E−06	0.04	8.20	0.17	0.60
WAL-A3-2.1.1	22/09/2014	5:38 PM	0.04	7.56E−06	0.04	3.52	0.17	0.60
WAL-A3-2.1.2	22/09/2014	5:45 PM	0.04	9.97E−06	0.04	4.47	0.23	0.62
WAL-A3-2.1.3	22/09/2014	5:53 PM	0.04	9.15E−06	0.04	5.65	0.21	0.62
WAL-A3-2.1.4	22/09/2014	6:01 PM	0.04	1.09E−05	0.04	7.35	0.25	0.63
WAL-A3-2.1.5	22/09/2014	6:09 PM	0.04	8.75E−06	0.04	7.11	0.20	0.61
WAL-A3-2.1.6	22/09/2014	6:17 PM	0.04	9.38E−06	0.04	7.81	0.21	0.62
WAL-A3-2.1.7	22/09/2014	6:25 PM	0.04	9.74E−06	0.04	7.40	0.22	0.62

Appendix 2: Results (*continued*)

Title	Date	Time	34S/32S	95%T_err	34S/32S drift corrected	Ratio Permil	StdErr_95%T	Total error
WAL-A3-2.1.8	22/09/2014	6:33 PM	0.04	1.01E−05	0.04	7.37	0.23	0.62
WAL-A3-2.1.9	22/09/2014	6:41 PM	0.04	1.17E−05	0.04	7.18	0.26	0.64
WAL-A3-2.1.10	22/09/2014	6:49 PM	0.04	7.41E−06	0.04	7.68	0.17	0.60
WAL-A3-2.1.11	22/09/2014	6:57 PM	0.04	9.71E−06	0.04	8.61	0.22	0.62
WAL-A3-2.1.12	22/09/2014	7:05 PM	0.04	8.53E−06	0.04	8.43	0.19	0.61
RUTTAN-12	22/09/2014	7:18 PM	0.04	8.26E−06	0.04	1.49	0.19	0.61
WAL-A3-3.1.1	22/09/2014	7:31 PM	0.04	1.12E−05	0.04	0.73	0.26	0.63
WAL-A3-3.1.2	22/09/2014	7:39 PM	0.04	1.26E−05	0.04	0.52	0.29	0.65
WAL-A3-3.1.3	22/09/2014	7:47 PM	0.04	1.38E−05	0.04	1.36	0.31	0.66
WAL-A3-3.1.4	22/09/2014	7:55 PM	0.04	1.07E−05	0.04	−0.28	0.24	0.63
WAL-A3-3.1.5	22/09/2014	8:03 PM	0.04	1.12E−05	0.04	0.29	0.25	0.63
WAL-A3-3.1.6	22/09/2014	8:11 PM	0.04	1.20E−05	0.04	0.09	0.27	0.64
WAL-A3-3.1.7	22/09/2014	8:19 PM	0.04	1.37E−05	0.04	0.24	0.31	0.66
WAL-A3-3.1.8	22/09/2014	8:27 PM	0.04	9.41E−06	0.04	0.01	0.21	0.62
WAL-A3-3.1.9	22/09/2014	8:35 PM	0.04	8.87E−06	0.04	1.51	0.20	0.61
WAL-A3-3.1.10	22/09/2014	8:43 PM	0.04	7.51E−06	0.04	0.09	0.17	0.60
WAL-A3-3.1.11	22/09/2014	8:51 PM	0.04	1.02E−05	0.04	0.15	0.23	0.62
WAL-A3-3.1.12	22/09/2014	8:59 PM	0.04	8.43E−06	0.04	−2.63	0.19	0.61
RUTTAN-13	22/09/2014	9:10 PM	0.04	9.12E−06	0.04	1.26	0.21	0.62
WAL-B3-1.1.1	22/09/2014	9:21 PM	0.04	8.83E−06	0.04	3.60	0.20	0.61
WAL-B3-1.1.2	22/09/2014	9:29 PM	0.04	1.05E−05	0.04	4.69	0.24	0.63
WAL-B3-1.1.3	22/09/2014	9:37 PM	0.04	1.36E−05	0.04	5.09	0.31	0.66
WAL-B3-1.1.4	22/09/2014	9:45 PM	0.04	1.07E−05	0.04	5.00	0.24	0.63
WAL-B3-1.1.5	22/09/2014	9:53 PM	0.04	9.80E−06	0.04	6.86	0.22	0.62
WAL-B3-1.1.6	22/09/2014	10:01 PM	0.04	9.67E−06	0.04	5.42	0.22	0.62
WAL-B3-1.1.7	22/09/2014	10:09 PM	0.04	1.16E−05	0.04	2.72	0.26	0.64
WAL-B3-1.1.8	22/09/2014	10:16 PM	0.04	6.29E−06	0.04	3.80	0.14	0.60
WAL-B3-1.1.9	22/09/2014	10:24 PM	0.04	7.79E−06	0.04	7.92	0.18	0.61
WAL-B3-1.1.10	22/09/2014	10:32 PM	0.04	9.01E−06	0.04	4.87	0.20	0.61
WAL-B3-1.1.11	22/09/2014	10:40 PM	0.04	8.73E−06	0.04	4.30	0.20	0.61
WAL-B3-1.1.12	22/09/2014	10:48 PM	0.04	1.07E−05	0.04	2.84	0.24	0.63
WAL-B3-1.11.1	22/09/2014	11:07 PM	0.04	8.11E−06	0.04	−0.21	0.18	0.61
WAL-B3-1.11.2	22/09/2014	11:15 PM	0.04	7.96E−06	0.04	1.34	0.18	0.61
WAL-B3-1.11.3	22/09/2014	11:23 PM	0.04	6.93E−06	0.04	3.53	0.16	0.60
WAL-B3-1.11.4	22/09/2014	11:30 PM	0.04	1.13E−05	0.04	3.51	0.26	0.63
WAL-B3-1.11.5	22/09/2014	11:38 PM	0.04	1.11E−05	0.04	3.18	0.25	0.63
WAL-B3-1.11.6	22/09/2014	11:46 PM	0.04	1.39E−05	0.04	7.35	0.31	0.66
WAL-B3-1.11.7	22/09/2014	11:54 PM	0.04	8.52E−06	0.04	2.27	0.19	0.61
WAL-B3-1.11.8	23/09/2014	12:02 AM	0.04	1.04E−05	0.04	1.75	0.24	0.63
WAL-B3-1.11.9	23/09/2014	12:10 AM	0.04	8.03E−06	0.04	2.74	0.18	0.61
WAL-B3-1.11.10	23/09/2014	12:18 AM	0.04	1.05E−05	0.04	2.59	0.24	0.63
WAL-B3-1.11.11	23/09/2014	12:26 AM	0.04	8.79E−06	0.04	2.00	0.20	0.61
WAL-B3-1.11.12	23/09/2014	12:34 AM	0.04	1.09E−05	0.04	2.88	0.25	0.63
RUTTAN-14	23/09/2014	12:44 AM	0.04	7.31E−06	0.04	0.68	0.17	0.60
RUTTAN-15	23/09/2014	12:53 AM	0.04	8.97E−06	0.04	1.00	0.20	0.61
WAL-B3-2.1.1	23/09/2014	1:05 AM	0.04	9.33E−06	0.04	4.68	0.21	0.62
WAL-B3-2.1.2	23/09/2014	1:13 AM	0.04	9.38E−06	0.04	0.88	0.21	0.62
WAL-B3-2.1.3	23/09/2014	1:21 AM	0.04	1.01E−05	0.04	2.78	0.23	0.62
WAL-B3-2.1.4	23/09/2014	1:29 AM	0.04	8.40E−06	0.04	2.35	0.19	0.61
WAL-B3-2.1.5	23/09/2014	1:37 AM	0.04	1.00E−05	0.04	1.86	0.23	0.62
WAL-B3-2.1.6	23/09/2014	1:45 AM	0.04	8.26E−06	0.04	3.34	0.19	0.61
WAL-B3-2.1.7	23/09/2014	1:53 AM	0.04	1.00E−05	0.04	4.71	0.23	0.62
WAL-B3-2.1.8	23/09/2014	2:01 AM	0.04	1.10E−05	0.04	6.68	0.25	0.63
WAL-B3-2.1.9	23/09/2014	2:09 AM	0.04	8.02E−06	0.04	4.55	0.18	0.61
WAL-B3-2.1.10	23/09/2014	2:17 AM	0.04	6.56E−06	0.04	4.69	0.15	0.60
WAL-B3-2.1.11	23/09/2014	2:25 AM	0.04	9.82E−06	0.04	5.42	0.22	0.62
WAL-B3-2.1.12	23/09/2014	2:33 AM	0.04	8.35E−06	0.04	5.30	0.19	0.61
RUTTAN-16	23/09/2014	2:42 AM	0.04	8.51E−06	0.04	0.84	0.19	0.61
WAL-A5-1.1.1	23/09/2014	2:53 AM	0.04	8.56E−06	0.04	5.45	0.19	0.61
WAL-A5-1.1.2	23/09/2014	3:01 AM	0.04	9.44E−06	0.04	7.89	0.21	0.62
WAL-A5-1.1.3	23/09/2014	3:09 AM	0.04	1.01E−05	0.04	7.87	0.23	0.62

(*continued on next page*)

Appendix 2: Results (*continued*)

Title	Date	Time	34S/32S	95%T_err	34S/32S drift corrected	Ratio Permil	StdErr_95%T	Total error
WAL-A5-1.1.4	23/09/2014	3:17 AM	0.04	1.14E−05	0.04	7.50	0.26	0.63
WAL-A5-1.1.5	23/09/2014	3:25 AM	0.04	1.02E−05	0.04	8.81	0.23	0.62
WAL-A5-1.1.6	23/09/2014	3:33 AM	0.04	1.08E−05	0.04	9.31	0.24	0.63
WAL-A5-1.1.7	23/09/2014	3:41 AM	0.04	9.08E−06	0.04	9.26	0.20	0.62
WAL-A5-1.1.8	23/09/2014	3:49 AM	0.04	6.93E−06	0.04	8.79	0.16	0.60
WAL-A5-1.1.9	23/09/2014	3:57 AM	0.04	7.41E−06	0.04	8.56	0.17	0.60
WAL-A5-1.1.10	23/09/2014	4:05 AM	0.04	9.55E−06	0.04	8.86	0.22	0.62
WAL-A5-1.1.11	23/09/2014	4:13 AM	0.04	1.00E−05	0.04	8.48	0.23	0.62
WAL-A5-1.1.12	23/09/2014	4:21 AM	0.04	8.71E−06	0.04	7.64	0.20	0.61
RUTTAN-17	23/09/2014	6:16 AM	0.04	7.81E−06	0.04	−2.14	0.18	0.61
RUTTAN-18	23/09/2014	6:26 AM	0.04	8.26E−06	0.04	1.02	0.19	0.61
WAL-A1-1.1.3	23/09/2014	6:57 AM	0.04	7.57E−06	0.04	−7.33	0.17	0.61
WAL-A1-1.1.4	23/09/2014	7:05 AM	0.04	1.05E−05	0.04	−4.68	0.24	0.63
WAL-A1-1.1.5	23/09/2014	7:13 AM	0.04	9.15E−06	0.04	−2.21	0.21	0.62
WAL-A1-1.1.6	23/09/2014	7:20 AM	0.04	9.19E−06	0.04	−2.01	0.21	0.62
WAL-A1-1.1.7	23/09/2014	7:28 AM	0.04	1.17E−05	0.04	−2.23	0.27	0.64
WAL-A1-1.1.8	23/09/2014	7:36 AM	0.04	8.82E−06	0.04	−3.49	0.20	0.61
WAL-A1-1.1.9	23/09/2014	7:44 AM	0.04	8.93E−06	0.04	−2.48	0.20	0.61
WAL-A1-1.1.10	23/09/2014	7:52 AM	0.04	7.60E−06	0.04	−3.90	0.17	0.61
WAL-A1-1.1.11	23/09/2014	8:00 AM	0.04	8.96E−06	0.04	−4.08	0.20	0.62
WAL-A1-1.1.12	23/09/2014	8:08 AM	0.04	1.08E−05	0.04	−3.29	0.25	0.63
RUTTAN-20	23/09/2014	8:28 AM	0.04	1.12E−05	0.04	1.72	0.25	0.63
RUTTAN-21	23/09/2014	8:37 AM	0.04	9.97E−06	0.04	1.35	0.23	0.62
WAL-A1-2.1.1	23/09/2014	9:08 AM	0.04	7.67E−06	0.04	−5.90	0.18	0.61
WAL-A1-2.1.2	23/09/2014	9:16 AM	0.04	9.08E−06	0.04	−5.74	0.21	0.62
WAL-A1-2.1.3	23/09/2014	9:24 AM	0.04	9.35E−06	0.04	−4.83	0.21	0.62
WAL-A1-2.1.4	23/09/2014	9:32 AM	0.04	8.68E−06	0.04	−4.16	0.20	0.61
WAL-A1-2.1.5	23/09/2014	9:40 AM	0.04	1.26E−05	0.04	−4.22	0.29	0.65
WAL-A1-2.1.6	23/09/2014	9:48 AM	0.04	9.51E−06	0.04	−3.84	0.22	0.62
WAL-A1-2.1.7	23/09/2014	9:56 AM	0.04	8.50E−06	0.04	−2.99	0.19	0.61
WAL-A1-2.1.8	23/09/2014	10:04 AM	0.04	9.21E−06	0.04	−2.45	0.21	0.62
WAL-A1-2.1.9	23/09/2014	10:12 AM	0.04	7.12E−06	0.04	−2.36	0.16	0.60
WAL-A1-2.1.10	23/09/2014	10:20 AM	0.04	7.38E−06	0.04	−2.89	0.17	0.60
WAL-A1-2.1.11	23/09/2014	10:28 AM	0.04	7.11E−06	0.04	−2.96	0.16	0.60
WAL-A1-2.1.12	23/09/2014	10:36 AM	0.04	9.00E−06	0.04	−1.99	0.21	0.62
RUTTAN-23	23/09/2014	1:27 PM	0.04	1.19E−05	0.04	1.44	0.27	0.64
RUTTAN-24	23/09/2014	1:35 PM	0.04	9.54E−06	0.04	1.14	0.22	0.62

Table 2 and 3. All values are in ppm and lie within the given parameters from GEOREM (GeoReM: A New Geochemical Database for Reference Materials and Isotopic Standards. Klaus Peter Jochum*, Uwe Nohl, Kirstin Herwig, Esin Lammel, Brigitte Stoll and Albrecht W. Hofmann. Article first published online: 22 MAY 2007 DOI: 10.1111/j.1751-908X.2005.tb00904.x.

Standard	Si 29	Ca 43	V 51	Ta 181	Pb 208	Ti 49	Zn 66	Se 77	Se 82	W 182
G_NIST610_1	326,000	81,900	440	452	426	433	454	108.4	108.9	444
G_NIST610_2	332,000	83,400	455	452	427	437	465	113	108	435
G_NIST610_3	331,000	82,900	441	460	433	441	458	114	110	449
G_NIST610_4	323,000	80,700	440	446	421	426	452	105	110	441
G_NIST610_5	334,000	90,000	446	460	450	447	470	121	100	470
G_NIST610_6	327,000	81,000	442	460	420	433	457	108	114	442
Average	328833.33	83316.67	444.00	455.00	429.50	436.17	459.33	111.57	108.48	446.83
Stan. Dev	4167.33	3437.10	5.83	5.90	11.08	7.28	6.86	5.71	4.63	12.22

Standard	Mn 55	Co 59	Cu 65	As 75	Mo 95	Ag 107	Sn 118	Sb 121	Pt 195	Au 197	Bi 209	Ni 60
Mass_1_1	258.1	69.5	138,700	59.1	53.48	59.99	58.33	59.74	77.9	48.1	64.41	149.6
Mass_1_2	197.6	57.6	109,700	50.9	46.1	51.36	49.22	49.39	61.7	39.2	51.26	103.2
Mass_1_3	205.3	59.3	108,800	54.8	46.8	53.6	51.3	52.84	59.5	40.5	54.7	110.4
Mass_1_4	215.1	56.9	107,500	53.2	47.2	48.65	50.5	52.78	54.8	36.56	50.38	93.9
Mass_1_5	187.4	47.2	102,500	48.43	43.6	45.85	45.52	47.28	55.6	36.5	44.11	96.6
Average	212.70	58.10	113,440	53.29	47.44	51.89	50.97	52.41	61.90	40.17	52.97	110.74
Stan. Dev	27.34	7.94	14392.29	4.04	3.66	5.38	4.67	4.73	9.38	4.75	7.45	22.64

Table 4. LA-ICP-MS Analysis of pyrite samples for each generation. All results in ppm. B.d.l (Below detection limit).

Generation	Samples	Te	Ag	As	Au	Bi	Ca	Co	Cu	Mn	Mo	Ni	Pb	Pt	Sb	Se77	Se82	Si	Sn	Ti	V	W	Zn
1	***WAL-A1-1***	4.00	0.97	440.67	0.45	3.04	2449.67	2360.67	660.70	126.46	b.d.l.	1283.33	20.97	0.02	10.36	21.10	18.30	9156.67	0.32	1561.33	14.21	5.01	26.73
	WAL-A1-2	6.23	1.09	76.60	0.22	2.01	103.00	184.00	468.00	18.40	b.d.l.	750.00	12.30	0.03	0.69	22.90	23.00	950.00	0.03	75.00	4.53	0.10	15.10
	WAL-A5-2	5.75	0.31	907.00	0.54	2.43	109.00	795.00	211.00	1.94	0.11	1517.00	27.00	0.04	128.00	4.57	4.66	1510.00	0.33	777.00	13.10	8.10	53.00
2	***WAL-A4-1***	3.47	0.27	45.03	0.02	0.04	99.00	14.20	13.13	0.94	b.d.l.	84.20	0.92	0.05	0.22	16.54	15.00	152.00	0.09	16.40	0.06	b.d.l.	2.22
	WAL-A3-3	12.99	0.90	202.20	1.21	5.33	580.00	344.00	490.00	19.30	590.00	3300.00	26.10	0.03	5.93	9.35	9.11	2510.00	0.19	78.00	18.70	0.98	15.30
	WAL-B3-2	12.62	0.23	101.60	0.61	7.26	28.00	296.00	31.00	1.21	b.d.l.	596.00	52.40	0.19	12.28	2.15	2.67	7230.00	0.17	260.00	46.10	3.73	8.33
3	***WAL-A10-1***	8.70	0.45	71.70	0.51	6.35	164.00	839.00	175.00	5.18	b.d.l.	764.00	14.60	0.01	2.13	5.32	6.80	2690.00	0.15	85.00	9.40	0.95	6.51
	WAL-GSZ80X-1	7.86	0.35	54.00	0.27	3.67	129.00	1130.00	30.20	51.80	b.d.l.	328.00	26.50	0.09	5.99	9.90	9.51	1610.00	0.16	1300.00	20.10	10.80	7.93
	WAL-GSZ80X-2	5.60	0.62	110.60	0.20	1.04	9980.00	462.00	27.80	209.00	b.d.l.	1135.00	23.70	0.48	3.66	3.30	2.10	34100.00	0.33	394.00	354.00	3.97	48.00
	WAL-B3-1	25.00	0.64	80.60	78.00	9.93	121.00	554.00	81.00	1.84	0.15	874.00	84.80	0.18	23.80	3.43	2.90	13160.00	0.29	1430.00	92.00	11.90	52.80
	WAL-A10-3	4.13	0.19	169.17	0.42	1.92	b.d.l.	708.33	25.73	1.09	0.01	715.33	6.12	0.01	1.83	3.42	4.40	1240.00	0.04	88.47	7.64	2.18	3.77
	WAL-GSZ80X-2	4.70	0.38	109.83	0.16	1.29	3442.00	1167.33	39.13	81.78	b.d.l.	648.00	16.17	0.18	3.22	9.07	8.13	12060.00	0.20	364.33	122.65	4.18	18.11
4a	***WAL-A10-2***	29.40	0.51	94.10	1.51	11.10	279.00	334.00	51.60	4.81	b.d.l.	1073.00	67.20	0.19	24.30	1.14	0.50	5960.00	0.18	1610.00	70.00	28.40	10.02
	WAL-B3-3	34.30	0.69	400.00	11.50	15.85	b.d.l.	1400.00	380.00	0.88	b.d.l.	1860.00	82.60	0.07	15.56	4.60	2.20	16800.00	b.d.l.	440.00	108.00	4.19	17.20
	WAL-A5-3	52.60	0.21	396.00	1.88	5.10	720.00	1193.00	56.10	19.30	0.07	1836.00	194.00	0.08	42.53	4.59	4.08	9110.00	0.33	886.00	74.70	19.30	11.14
	WAL-A3-2	38.20	0.11	4460.00	33.10	0.93	77.00	243.00	31.20	0.86	0.06	401.00	30.00	b.d.l.	3.50	1.91	2.36	327.00	1.00	27.70	0.09	b.d.l.	1.96
	WAL-GSZ70-1	32.00	0.26	32.10	0.54	3.89	66.00	115.40	21.50	0.67	1.96	522.00	14.40	0.03	1.57	11.33	11.65	1280.00	0.28	102.00	2.41	3.02	3.69
	WAL-GSZ70-2	75.10	0.25	212.20	0.12	1.49	103.00	104.70	36.00	0.23	b.d.l.	419.00	41.00	0.06	0.24	19.30	16.60	440.00	0.23	15.30	0.07	b.d.l.	1.42
4b	***WAL-A10-2***	0.00	0.90	309.00	0.13	0.16	b.d.l.	108.00	43.00	0.49	b.d.l.	586.00	1.70	b.d.l.	0.66	7.80	2.20	b.d.l	b.d.l.	21.20	0.19	b.d.l.	5.50
	WAL-A10-2	7.40	3.10	195.00	20.00	0.52	370.00	212.00	96.00	2.10	0.45	684.00	2.96	35.00	1.14	3.40	4.00	490.00	0.63	29.40	0.34	0.29	16.60
	WAL-B3-3	19.30	0.16	72.70	0.65	11.09	75.00	221.00	27.00	1.58	b.d.l.	558.00	68.50	0.03	14.25	2.94	2.10	9660.00	0.06	193.00	56.90	1.61	9.85
	WAL-B3-3	19.80	0.24	103.30	0.79	10.85	101.00	302.00	67.00	3.30	b.d.l.	631.00	72.40	0.12	14.87	1.50	1.80	14200.00	0.04	185.00	60.30	2.32	11.00
	WAL-GSZ70-2	251.00	0.22	75.10	1.16	2.79	76.00	65.50	24.00	0.67	0.09	295.00	10.10	0.04	1.36	21.80	22.70	660.00	0.14	44.00	0.73	5.30	2.23
	WAL-GSZ70-2	61.90	0.34	101.00	1.13	13.40	56.00	262.00	34.50	0.80	5.50	1990.00	27.30	0.08	2.78	12.80	12.60	3020.00	0.21	17.70	0.03	0.04	3.04
5	***WAL-A1-3***	5.30	0.21	149.90	0.13	3.57	89.33	2036.00	29.87	65.50	b.d.l.	256.73	30.24	0.03	3.18	26.67	24.63	3220.00	0.13	148.63	8.50	0.06	16.47
	WAL-A3-1	43.14	4.19	869.67	4.59	26.27	145.67	167.33	22.20	3.31	b.d.l.	327.33	8570.42	0.01	18.54	0.86	0.88	70.33	0.09	29.20	0.09	b.d.l.	7.59
	WAL-A5-1	24.22	2.20	509.78	2.36	14.92	117.50	1101.67	26.03	34.40	b.d.l.	292.03	4300.33	0.02	10.86	13.77	12.76	1645.17	0.11	88.92	4.29	0.03	12.03
	WAL-A9-1	0.59	0.18	14.33	0.07	1.13	70.00	140.70	16.30	0.74	b.d.l.	323.00	5.88	b.d.l.	0.66	4.55	4.97	532.00	0.37	72.00	1.86	1.47	1.68

References

Arehart, G.B., Chryssoulis, S.L., Kesler, S.E., 1993. Gold and arsenic in iron sulfides from sediment-hosted disseminated gold deposits; implications for depositional processes. Econ. Geol. 88 (1), 171–185.

Belcher, R.W., Rozendaal, A., Przybylowicz, W.J., 2004. Trace element zoning in pyrite determined by PIXE elemental mapping: evidence for varying ore–fluid composition and electrochemical precipitation of gold at the Spitskop deposit, Saldania Belt, South Africa. X-Ray Spectrom. 33 (3), 174–180.

Coggon, J., 2003. Magnetism—key to the Wallaby gold deposit. Explor. Geophys. 34 (1/2), 125–130.

Cook, N.J., Chryssoulis, S.L., 1990. Concentrations of invisible gold in the common sulfides. Can. Mineral. 28 (1), 1–16.

Cox, S., Sun, S., Etheridge, M., Wall, V., Potter, T., 1995. Structural and geochemical controls on the development of turbidite-hosted gold quartz vein deposits, Wattle Gully mine, central Victoria, Australia. Econ. Geol. 90 (6), 1722–1746.

Craig, J.R., Vokes, F.M., Solberg, T.N., 1998. Pyrite: physical and chemical textures. Miner. Deposita 34 (1), 82–101.

Crowe, D., Vaughan, R., 1996. Characterization and use of isotopically homogeneous standards for in situ laser microprobe analysis of 34S/32S ratios. Am. Mineral. 81 (1–2), 187–193.

Deditius, A.P. et al., 2011. Trace metal nanoparticles in pyrite. Ore Geol. Rev. 42 (1), 32–46.

Goldfarb, R.J., Groves, D.I., 2015. Orogenic gold: common or evolving fluid and metal sources through time. Lithos 233, 2–26.

Groves, D., 1993. The crustal continuum model for late-Archaean lode-gold deposits of the Yilgarn Block, Western Australia. Miner. Deposita 28 (6), 366–374.

Hallberg, J.A., 1985. Geology and Mineral Deposits of the Leonora-Laverton Area, Northeastern Yilgarn Block, Western Australia.

Henson, P., Blewett, R., Roy, I., Miller, J.M., Czarnota, K., 2010. 4D architecture and tectonic evolution of the Laverton region, eastern Yilgarn Craton, Western Australia. Precambrian Res. 183 (2), 338–355.

Hodkiewicz, P., Groves, D., Davidson, G., Weinberg, R., Hagemann, S., 2009. Influence of structural setting on sulphur isotopes in Archean orogenic gold deposits, Eastern Goldfields Province, Yilgarn, Western Australia. Mineral. Deposita 44 (2), 129–150.

Hodkiewicz, P., Weinberg, R., Gardoll, S., Groves, D., 2005. Complexity gradients in the Yilgarn Craton: fundamental controls on crustal-scale fluid flow and the formation of world-class orogenic-gold deposits. Aust. J. Earth Sci. 52 (6), 831–841.

Johnson, T.M., Herbel, M.J., Bullen, T.D., Zawislanski, P.T., 1999. Selenium isotope ratios as indicators of selenium sources and oxyanion reduction. Geochim. Cosmochim. Acta 63 (18), 2775–2783.

King, J., Williams-Jones, A., van Hinsberg, V., Williams-Jones, G., 2014. High-sulfidation epithermal pyrite-hosted Au (Ag-Cu) ore formation by condensed magmatic vapors on Sangihe Island, Indonesia. Econ. Geol. 109 (6), 1705–1733.

Kojonen, K., Johanson, B., 1999. Determination of refractory gold distribution by microanalysis, diagnostic leaching and image analysis. Mineral. Petrol. 67 (1–2), 1–19.

Kositcin, N., Brown, S.J., Barley, M.E., Krapež, B., Cassidy, K.F., Champion, D.C., 2008. SHRIMP U-Pb zircon age constraints on the Late Archaean tectonostratigraphic architecture of the Eastern Goldfields superterrane, Yilgarn craton, Western Australia. Precambrian Res. 161 (1), 5–33.

Large, R.R. et al., 2009. Gold and trace element zonation in pyrite using a laser imaging technique: implications for the timing of gold in orogenic and Carlin-style sediment-hosted deposits. Econ. Geol. 104 (5), 635–668.

Lehner, S., Savage, K., Ayers, J., 2006. Vapor growth and characterization of pyrite (FeS_2) doped with Co, Ni, and As: Variations in semiconducting properties. J. Cryst. Growth 286 (2), 306–317.

Longerich, H., Günther, D., Jackson, S., 1996a. Elemental fractionation in laser ablation inductively coupled plasma mass spectrometry. Fresenius' J. Anal. Chem. 355 (5–6), 538–542.

Mason, D.R., 1999. Placer Dome Report.

McPhail, D., 1995. Thermodynamic properties of aqueous tellurium species between 25 and 350°. Geochim. Cosmochim. Acta 59 (5), 851–866.

Miller, J., 2006. Linking structure and mineralisation in Laverton, with specific reference to Sunrise Dam and Wallaby. In: Predictive Mineral Discovery CRC-Extended Abstracts for the April 2006 Conference. Geoscience Australia Record, pp. 62–67.

Moritz, R., 2000. What have we learnt about orogenic lode gold deposits over the past 20 years. Internet.

Mueller, A.G. et al., 2008. Archean high-Mg monzodiorite–syenite, epidote skarn, and biotite–sericite gold lodes in the Granny Smith-Wallaby district, Australia: U-Pb and Re–Os chronometry of two intrusion-related hydrothermal systems. Miner. Deposita 43 (3), 337–362.

Neumayr, P. et al., 2008. Oxidized and reduced mineral assemblages in greenstone belt rocks of the St. Ives gold camp, Western Australia: vectors to high-grade ore bodies in Archaean gold deposits? Miner. Deposita 43 (3), 363–371.

Ohmoto, H., 1972. Systematics of sulfur and carbon isotopes in hydrothermal ore deposits. Econ. Geol. 67 (5), 551–578.

Peterson, E.C., Mavrogenes, J.A., 2014. Linking high-grade gold mineralization to earthquake-induced fault-valve processes in the Porgera gold deposit, Papua New Guinea. Geology G35286, 1.

Pokrovski, G.S., Kara, S., Roux, J., 2002. Stability and solubility of arsenopyrite, FeAsS, in crustal fluids. Geochim. Cosmochim. Acta 66 (13), 2361–2378.

Pokrovski, G.S., Roux, J., Harrichoury, J.-C., 2005. Fluid density control on vapor-liquid partitioning of metals in hydrothermal systems. Geology 33 (8), 657–660.

Raiswell, R., Plant, J., 1980. The incorporation of trace elements into pyrite during diagenesis of black shales, Yorkshire, England. Econ. Geol. 75 (5), 684–699.

Reddy, S.M., Hough, R.M., 2013. Microstructural evolution and trace element mobility in Witwatersrand pyrite. Contrib. Miner. Petrol. 166 (5), 1269–1284.

Reich, M. et al., 2013. Pyrite as a record of hydrothermal fluid evolution in a porphyry copper system: a SIMS/EMPA trace element study. Geochim. Cosmochim. Acta 104, 42–62.

Reich, M. et al., 2005. Solubility of gold in arsenian pyrite. Geochim. Cosmochim. Acta 69 (11), 2781–2796.

Rye, R.O., Ohmoto, H., 1974. Sulfur and carbon isotopes and ore genesis: a review. Econ. Geol. 69 (6), 826–842.

Salier, B.P., Groves, D.I., McNaughton, N.J., Fletcher, I.R., 2004. The world-class Wallaby gold deposit, Laverton, Western Australia: an orogenic-style overprint on a magmatic-hydrothermal magnetite-calcite alteration pipe? Miner. Deposita 39 (4), 473–494.

Salier, B.P., Groves, D.I., McNaughton, N.J., Fletcher, I.R., 2005. Geochronological and stable isotope evidence for widespread orogenic gold mineralization from a deep-seated fluid source at ca 2.65 Ga in the Laverton gold province, Western Australia. Econ. Geol. 100 (7), 1363–1388.

Seward, T.M., 1973. Thio complexes of gold and the transport of gold in hydrothermal ore solutions. Geochim. Cosmochim. Ac. 37 (3), 379–399.

Shenberger, D., Barnes, H., 1989. Solubility of gold in aqueous sulfide solutions from 150 to 350 °C. Geochim. Cosmochim. Acta 53 (2), 269–278.

Sibson, R., 1992. Implications of fault-valve behaviour for rupture nucleation and recurrence. Tectonophysics 211 (1–4), 283–293.

Skirrow, R.G., Walshe, J.L., 2002. Reduced and oxidized Au-Cu-Bi iron oxide deposits of the Tennant Creek Inlier, Australia: an integrated geologic and chemical model. Econ. Geol. 97 (6), 1167–1202.

Standing, J.G., 2008. Terrane amalgamation in the Eastern Goldfields Superterrane, Yilgarn Craton: evidence from tectonostratigraphic studies of the Laverton Greenstone Belt. Precambr. Res. 161 (1), 114–134.

Stoltze, A., Campbell, I., Nakamura, E., McCulloch, M., 2006. The use of radiogenic isotopes for identifying the mineralising fluid source at the Wallaby Gold Deposit, Northeastern Goldfields, Western Australia. Geochim. Cosmochim. Acta 70 (18), A618.

Swager, C.P., 1997. Tectono-stratigraphy of late Archaean greenstone terranes in the southern Eastern Goldfields, Western Australia. Precambrian Res. 83 (1), 11–42.

Thomas, H.V. et al., 2011. Pyrite and pyrrhotite textures and composition in sediments, laminated quartz veins, and reefs at Bendigo gold mine, Australia: insights for ore genesis. Econ. Geol. 106 (1), 1–31.

Wall, V., 2001. Wallaby Petrology: Part of a Geological Overview of the Wallaby Lode-Gold Project, Laverton Region, Western Australia. Placer Granny Smith. Technical Report.

Walshe, J., Halley, S., Hall, G., Kitto, P., 2003. Contrasting fluid systems, chemical gradients and controls on large-tonnage, high-grade Au deposits, Eastern Goldfields Province, Yilgarn Craton, Western Australia. Mineral Explor. Sustainable Dev., 827–830

Weatherley, D.K., Henley, R.W., 2013. Flash vaporization during earthquakes evidenced by gold deposits. Nat. Geosci. 6 (4), 294–298.

Yamamoto, M., Kase, K., Ueda, A., 1983. Fractionation of sulfur isotopes and selenium between coexisting pyrite and chalcopyrite from the Hitachi deposits, Ibaraki Prefecture, Japan. Geochem. J. 17 (1), 29–39.

Yang, S., Blum, N., 1999. A fossil hydrothermal system or a source-bed in the Madiyi Formation near the Xiangxi Au–Sb–W deposit, NW Hunan, PR China? Chem. Geol. 155 (1), 151–169.

3. TRACE ELEMENT PARTITIONING BETWEEN PYRITE AND PYRRHOTITE AS A MONITOR OF FLUID EVOLUTION AT THE ARGO (WA) GOLD DEPOSIT.

ABSTRACT

Argo, a mesothermal lode gold deposit in Western Australia, records extreme fluid-rock interaction that produced systematic changes to sulfide trace elements across all vein stages. Vein paragenesis established 4 pyrite bearing vein events, displaying systematic changes in chemistry in a manner similar to the Wallaby Au mine, WA (Ward et al. 2017). However, changes in trace element concentrations across the Argo paragenesis differ due to the appearance of co-existing Fe-(As)-S minerals in the late stages. Unlike typical Au-bearing pyrite deposits, at Argo, the highest Au concentrations do not correlate with the highest As concentrations. This is attributed to co-precipitation of pyrrhotite affecting the trace metal budget of pyrite. The presence of additional Fe-S sulfides, i.e pyrrhotite, systematically alters observed trends. In such cases, the pyrite/pyrrhotite partition coefficient (D), in particular for As, Ni and Au clearly tracks chemical changes. At Argo, D of Ni, Co and As decrease through time whereas Au increases. Thus DAu/DAs or DAu/DNi accurately monitor changes in the sulfides relative to Au deposition. This systematic change with time is a potentially powerful exploration tool.

3.1 INTRODUCTION

Argo, a Neoarchean greenstone-hosted mesothermal lode gold deposit situated 90 kilometres south-southeast of Kalgoorlie in the St Ives gold region (Western Australia) (Figure 3.1) which is reported to have yielded over 45 t of gold (McGoldrick et al., 2013a; Prendergast, 2007). The combined Argo- Athena- Hamlet Deposits are estimated to have contained 3.7Moz (Ovens, 2014). This deposit is hosted within an Archean volcano-sedimentary sequence in the

Norseman- Wiluna Greenstone Belt (NWGB) which is part of the broader Eastern Goldfields Province (EGP), a major component of the Yilgarn Craton reported to contain at least 15 of the world's largest gold deposits (Crawford, 2011; Hageman and Cassidy, 2000). In 1994 this deposit was developed as an open pit (130m depth) and later (2003) an underground mine by Goldfields Ltd (Ovens, 2014). A series of anticlines within the Kambalda region controlled mineralising fluid pathways at Argo. Gold deposition is likely to have been prompted by a reduction of the ore fluid causing destabilization of gold complexes during pressure variations established by a "fault-valve" system (Blewett et al., 2010; Cox and Ruming, 2004; McGoldrick et al., 2013a). This study tracks pyrite chemistry through time with respect to co-precipitating pyrrhotite.

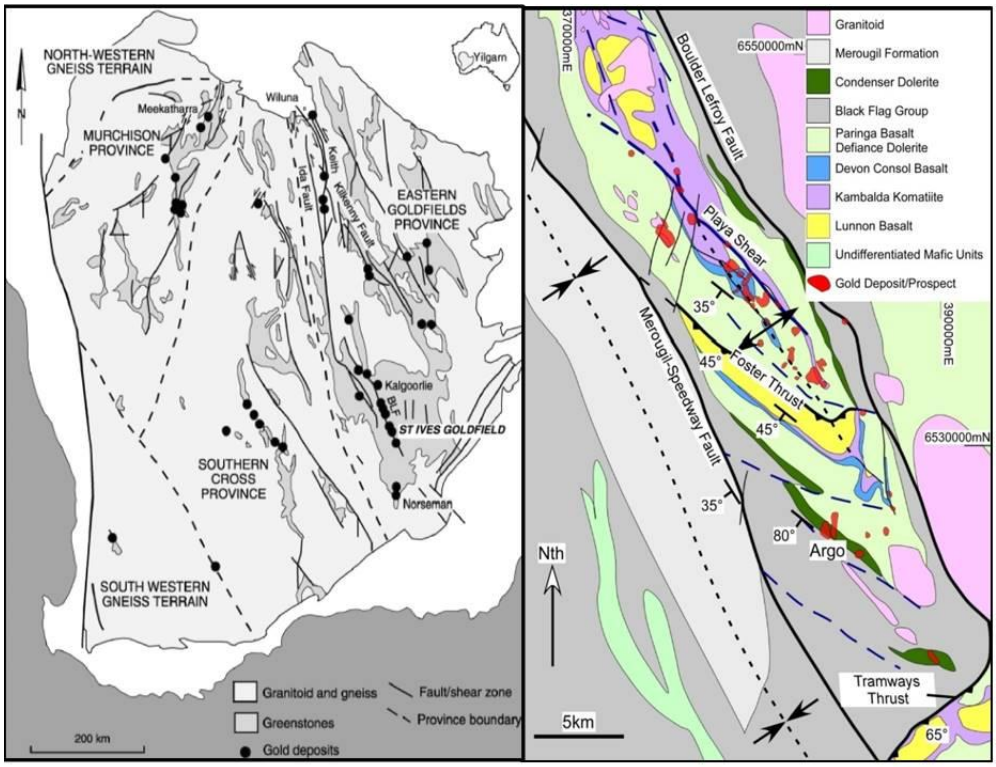

Figure 3.1: (left) Major gold deposits of the Archean Yilgarn Craton of Western Australia (modified from Crawford 2011 modified from Cox et al., 2004). (Right) Simplified geological map of Argo including major structures in the area, including the D1 thrust, D2 fold trends and D3 regional faults. The locations of faults interpreted from regional magnetic data are shown as blue dashed lines. The gold deposits in the area cluster in and around the Playa Fault and within the core of the D2 Kambalda Anticline. The Argo deposit is remote from the main Playa region and hosted within the Condenser Dolerite.

The Argo deposit experienced four deformation events (D1-4) that coincide with the four representative vein sets containing variable amounts of native Au and Au (and associated trace elements) in pyrite. The Argo deposit formed over millennia (the main gold event occurring 2680-2625Ma) over a range of redox conditions (Crawford, 2011). Pyrite is present in all vein stages at Argo, and provides a sensor of changes in fluid chemistry (Ward et al., 2017). This geochemical change is observed through a change of Fe-oxides with subsequent stages i.e hematite in stage 1 and magnetite, pyrrhotite and minor arsenopyrite in later stages (2-4) (Figure 3.2 and Figure 3.3).

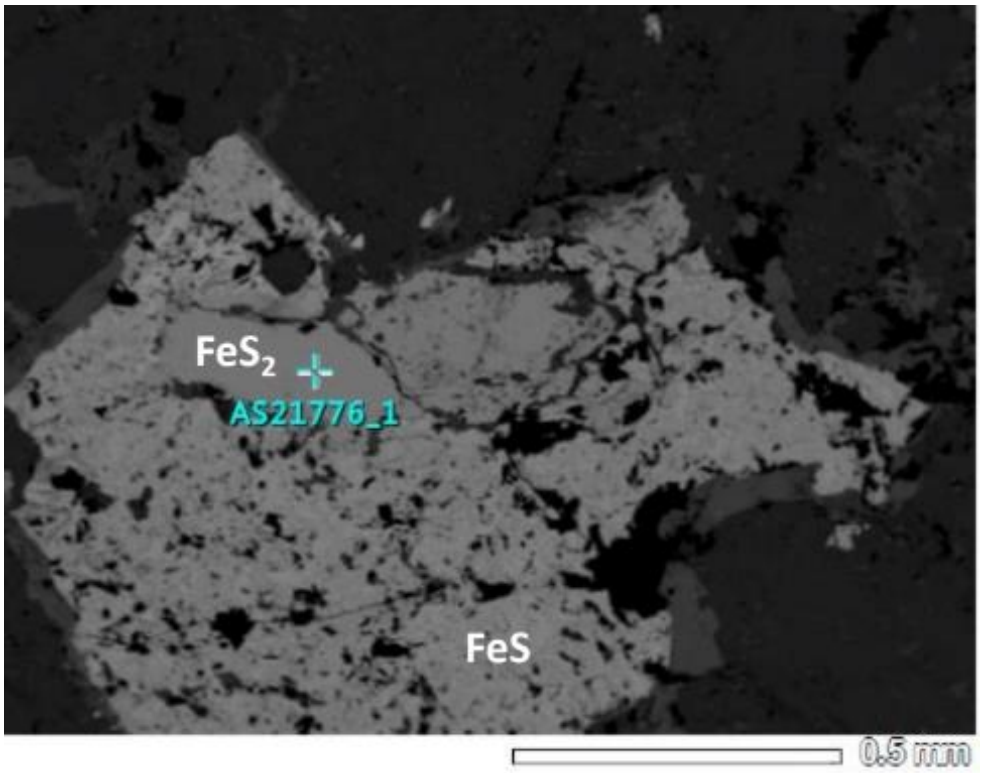

Figure 3.2 SEM image of Sample AS21776-1 showing co-existing pyrite-pyrrhotite in Stage 4 mineralisation

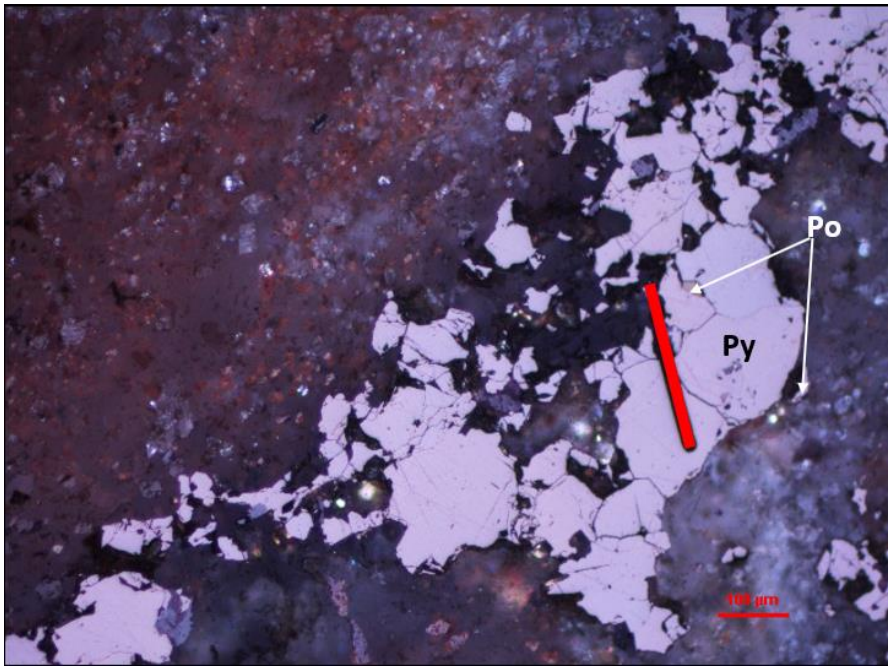

Figure 3.3 XPL 100µm image of Sample AS21287 showing co-existing pyrite-pyrrhotite in Stage 2 mineralisation. Red line denotes LA-ICP-MS traverse.

Redox in particular, has been shown to control sulfur isotopes of pyrite, pyrrhotite and arsenopyrite (Godefroy-Rodríguez et al., 2018; LaFlamme et al., 2018; Ward et al., 2017). At Wallaby (WA), where pyrite is the only iron sulfide, sulfur isotopes and trace elements reflect changing redox conditions (Ward et al., 2017). The py-po assemblage is established elsewhere in the Archean terranes of WA to reflect reducing conditions via sulfur isotopes (Oroya and Mt Charlotte), and the hm-py assemblage to reflect oxidising conditions (e.g. Finniston) (Godefroy-Rodríguez et al., 2018; LaFlamme et al., 2018), At Argo, on the other hand, fluid redox transitioned from hm-py to py- po in the later stages. We suggest that trace element partitioning between coexisting iron sulfides significantly alters established pyrite trace element trends independent of sulfur isotopic signatures. This is due to the competition for trace elements during crystallisation as shown by partition coefficients for As and Au. The Nernst distribution coefficient has been used between phases to predict the likelihood of sulfide ore enrichment in Ni and PGEs (Campbell and Naldrett, 1979), and as this depends on

redox, it may be employed to uncover the trace element trends between co-existing iron sulfides at Argo.

Regional and Deposit Geology

The Argo–Junction deposit is situated on the Western flank of the Kambalda anticline and is largely hosted by the Paringa Basalt (7130m thick Mg rich Archean komatiite), Condenser dolerite (tholeiitic gabbro) and the volcano-sedimentary Black Flag Group (Cox and Ruming, 2004; Crawford, 2011; McGoldrick et al., 2013a; Roberts, 1990). The Paringa basalt is intruded by the Condenser Dolerite and all hosts are metamorphosed to greenschist facies (McGoldrick 2013a). Mineralisation occurs throughout the stratigraphic column at Argo, concentrating in the granophyric zone within a series of faults (Argo Fault System, AFS) at the Northern end of the deposit (Cox and Ruming, 2004; Crawford, 2011; McGoldrick et al., 2013a; McGoldrick et al., 2013b; Myers, 1997; Nelson, 2008). The regional antiform is overturned towards the north west, creating a sink for ore fluids (Blewett et al., 2010). Subsequent shearing resulted in 4 stages of deformation and mineralisation, as seen in the vein sequences (Extension, Stockwork, Breccia and Fault –fill veins).

Deformation Events and Mineralisation

As mentioned, the Argo Fault System (AFS) consists of four distinct structural events (Figure 3.1, Figure 3.4 and Figure 3.5) recorded by four vein sets best observed within the core of the AFS, where they are clearly distinguishable through mineralogy and overprinting relationships. These structural events and their related vein type are as follows:

D1 – Stage 1 Veins – developed within the shear zones resulting in extensional quartz-calcite veins (<1cm thick) with chlorite-biotite-quartz-plagioclase-ilmenite-rutile alteration and minor pyrite, chalcopyrite and hematite within compositional banding parallel to foliation. Pyrite crystals are dominantly euhedral with sulfide inclusion-rich rims and cores containing silicate inclusions.

D2 – Stage 2 Veins - are a stockwork vein system (Fe-Dol-Qz) in the core of the shear zone. Pyrite and minor pyrrhotite fill fractures within the stockwork of brecciated veins. Vein selvages typically contain muscovite-biotite-calcite alteration assemblages.

D3 – Stage 3 Veins – are Au-bearing quartz-calcite fault fill veins and extensional veins in regional shears (displacement of the Playa fault) (Figure 3.1). These veins carry sulfides (pyrite-pyrrhotite -arsenopyrite-/+chalcopyrite) and native Au. This stage is characterized by alteration assemblages of biotite-tourmaline-muscovite, as compositional banding parallel to the laminated quartz-calcite fault fill veins. These veins, up to a metre wide, are strongly laminated and contain large, euhedral sulfide and gold crystals. This is the main structural event at Argo and hosts the majority of the gold.

D4 – Stage 4 Veins–consist of thin quartz-calcite-biotite extensional veins overprinting the centre of the AFS. Pyrite grains on vein edges and in the matrix are commonly associated with biotite-tourmaline- calcite alteration. These medium to coarse grained pyrite crystals are

similar to those in Stage 3. Stage 4 pyrite crystals are regularly overgrown by un-deformed, inclusion-rich pyrrhotite.

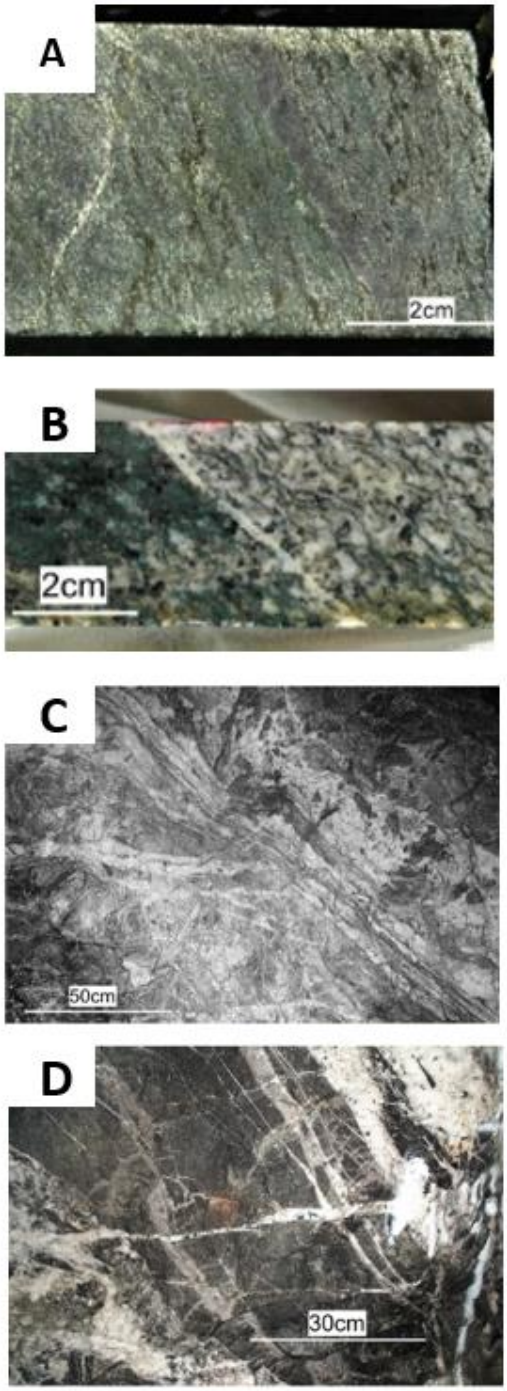

Figure 3.4: A) Stage 1 foliation defined by aligned chlorite aggregates and compositional banding of carbonate-quartz aggregates B) Stage 2 stockwork veins (carbonate-quartz) set in a fine-grained matrix of carbonate, chlorite and quartz C) laminated stage 3 quartz vein with thin laminations D) Sub-horizontal stage 4 extension vein (centre) cross-cutting a foliated wallrock clast in a stage 3 breccia vein modified after Crawford 2012.

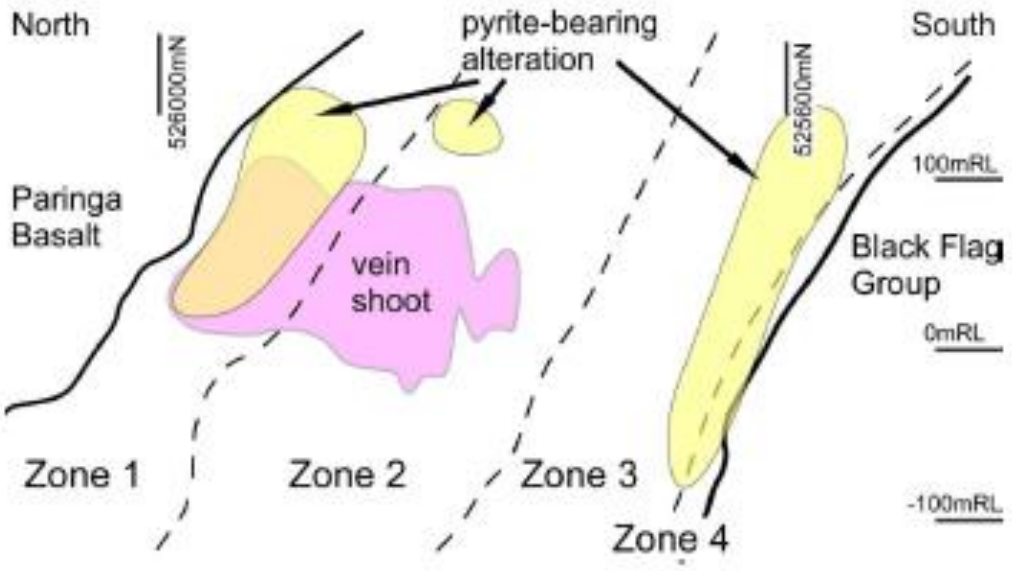

Figure 3.5: N-S long-section of the A01 shear zone displaying the mineralised zones sampled. Mineralised zones have been constrained using a diamond drilling database and underground mapping by Crawford (2011).

While mineralisation is seen most commonly in the Condenser dolerite, Au and pyrite occur predominantly in the Mg-rich Paringa Basalt (McGoldrick et al., 2013a). Significant mineralisation is also observed in D_3 veins that correlate with regional shearing at 2630Ma (Crawford, 2011). Successive faulting developed brittle-ductile shear zones (up to 30m in width) that show systematic hydrothermal alteration (Cox and Ruming, 2004; Crawford, 2011; Sibson et al., 1988). Cox et al. (2004) assert that increased permeability due to shearing and associated pressure drops facilitated the injection of hydrothermal fluids into the host rock, encouraging fluid-rock interaction (Cox, 2010; Cox, 1995).

Whole rock analyses identified pathfinder elements for exploration in the Archean goldfields in Western Australia (Prendergast, 2007). While As, Bi, Sb, W and Mo are concentrated in structural zones at Argo, the mechanism(s) under which these elements were deposited or in what minerals they occur is not well established. The temperature of the hydrothermal fluids

that transported gold have been estimated, by arsenopyrite thermometry, at 300 to 400° C (Howe, 2002). The mineral assemblages identified within the Argo deposit suggest the fluid was above the CO_2-CH_4 buffer (Crawford, 2011). Goldfarb and Groves (2015) established that all orogenic Au deposits of single origin, regardless of age, are of similar chemical composition with pH estimated to be near neutral at 5.5 (Goldfarb and Groves, 2015).

Cox et al. (2004) established that high fluid flux during active deformation enhanced permeability enabling lode gold deposition. This is thought to occur near the seismic-aseismic transition, at between 300° and 450°C(Groves, 1993). Crawford (2011) proposed factors that facilitated mineralisation at Argo, including large-scale pressure changes, wall rock interaction and fluid mixing. The host rock at Argo shows crystal overgrowths (replacement textures) and structural deformations that suggest wall rock interaction as the dominant mechanism for Au deposition. This study aims to identify progressive change in the sulfur isotope patterns in successive pyrite generations at Argo and link this to any observed trace element chemistry changes. This study while focussing on pyrite has identified that when a deposit has an additional Fe-S mineral, such as pyrrhotite, inherent mineral chemistry and the geochemical conditions primarily drives trace element concentration in iron sulfides.

Sulfide bonding is complex relative to oxide and silicate due to the reduced electronegativity of S in comparison, bonding is primarily serviced via molecular orbital formation by way of sharing electrons to satisfy valence requirements (Nesse, 2009). Particular trace elements like Ag, Co, Ni and Pb have preference to concentrate in Fe-S minerals (Hawley and Nichol, 1961). While Co is shown to preferentially concentrate in pyrite to pyrrhotite and Ni in the latter, which Fe-S minerals the elements will concentrate in appears to be dependent on the geochemistry of the deposit (Hawley and Nichol. 1961). Pyrite typically has a structure similar

to halite while pyrrhotite has a pseudohexagonal structure and often substitutes $2Fe^{3+}$ + □ (vacancy) for $3Fe^{2+}$, this leads pyrrhotite to being able to concentrate a significant percentage (13%) of Fe sites for other similar sized cations in comparison to pyrite (Nesse, 2009). Arenopyrite is a sulfarsenide, where As and S act as anions, it forms similarly to marcasite (similar to pyrite) and often replaces Co for Fe (Nesse, 2009). Understanding that trends in pyrite can only be understood by observing the entire Fe-S system present is novel and while this study attempts to uncover some of the preferential partitioning behaviour between Py-Po, further work is required to better delineate partitioning coefficients.

3.2 METHODOLOGY

Sample Selection

Samples were selected from Matthew Crawford's PhD collection. Crawford (2011) used structural relationships to establish veining paragenesis at Argo (Figure 3.4). Samples of all mineralised stages were selected from the stores at The Australian National University (ANU). Stages were categorised in the field based upon regional knowledge, cross-cutting relationships, mineral assemblages and micro-textures observed in veins identified previously. As Argo's mineral assemblage shows progressive reduction, expressed by the disappearance of hematite (after stage 1) and the appearance of pyrrhotite (in stage 2) (Toulmin III and Barton Jr, 1964), these minerals established redox conditions and guided selection of pyrite samples that best reflect this incremental change. Micro differences in pyrite stages can be observed in Figure 3.7. The electron microprobe at ANU (Cameca SX 100) was used during identification and selection to investigate quantitatively whether Argo exhibited significant or measureable zoning in minor trace elements commonly observed in Au ore deposits. Emission dispersive spectrometry (EDS) was used to map element zonation and while weak or limited patterns were occasionally observed, all pyrites were identified to be generally homogenous (Figure 3.6).

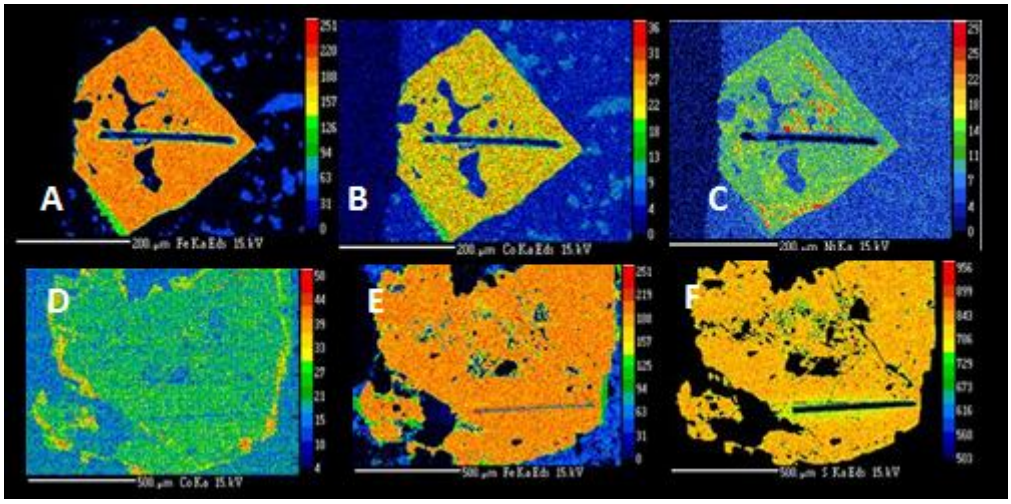

Figure 3.6: EDS microprobe images: Stage 3 Sample 12005 a) Fe showing rim depletion b) Co rim enrichment c) Assymetric Ni zonation; Stage 3 Sample 276 d) Co rim enrichment e) Fe rim depletion f) Sulfur

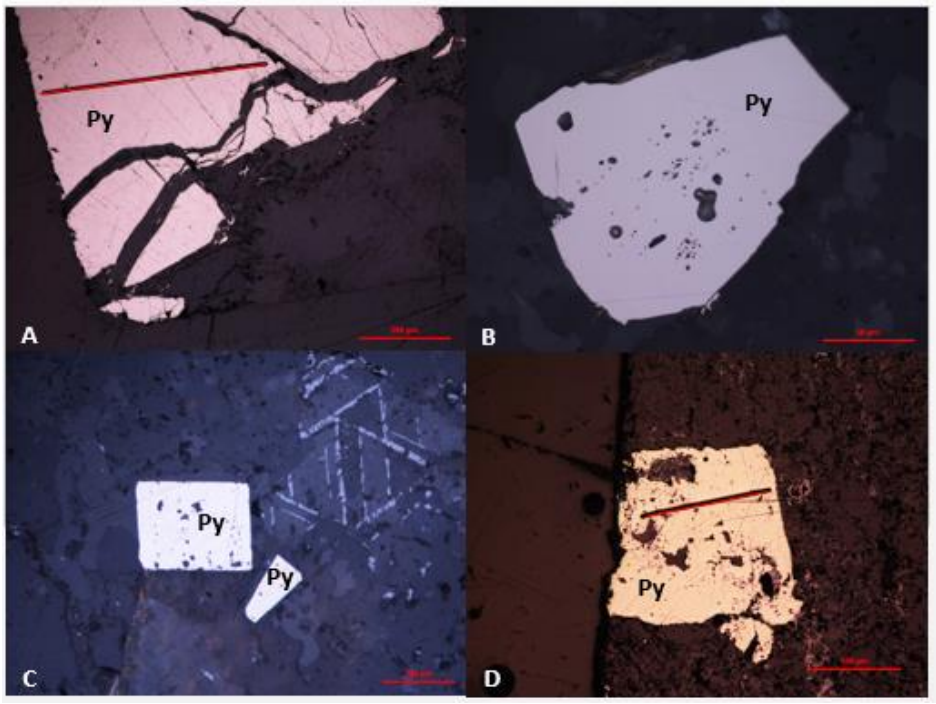

Figure 3.7: A) Sample 033, well-formed Stage 1 pyrite with fracture filled by quartz vein, cracks on pyrite surface from faulting observed B) Sample 276, anhedral Stage 2 pyrite with minor inclusions in the centre of the crystal C) Sample 12005, euhedral Stage 3 pyrite trace inclusions D) Sample 234, Stage 4 pyrite with larger inclusions observed across the pyrite surface.

Samples were cut, set in mounts and polished to ¼µm and studied by reflected light microscopy, Scanning Electron Microscopy (SEM), Laser Ablation Inductively Coupled Mass Spectrometry (LA-ICP-MS) and Sensitive High Resolution Iron Micro-Probe Stable Isotope (SHRIMP-SI).

SHRIMP-SI

SHRIMP-SI was used to measure $\delta^{34}S$ using a 3µm spot on aluminium coated polished mounts for a selection of stage 1-4 pyrites over a 24-hour period (Appendix 1 Table 3.2). Pyrite from Ruttan, Manitoba ($\delta^{34}S$ 1.2 per mil, Crowe and Vaughan 1996) was used to standardize each session and was analysed at the start, after every 6 spots and at the conclusion of each session, with standard analyses all within error. SHRIMP –SI analyses used 2 detectors with data acquired through 10 separate integrations of 10 seconds. Total error on samples was +/- 0.18 per mil for all pyrites analysed. Samples were polished and cleaned in an ultrasonic bath after the SHRIMP analyses to remove any remnant Al on the surface or in pits. All measurements are relative to Canyon Diablo Troilite (CDT).

LA-ICPMS

Multiple pyrite grains from all 4 stages and pyrrhotites from stages 2-4 were selected by reflected light microscopy and SEM to avoid inclusions, LA- ICPMS traverse counts per second (CPS) were observed to ensure grains were relatively homogenous and so able to represent the true value of the grain (Figure). Pyrite grains were then analysed at the Research School of Earth Science at the Australian National University by an Agilent 100 LA-ICPMS system using a 20µm traverse to acquire average trace element concentrations across a crystal's surface at a rate of 1µm per second. The LA-ICP-MS operated using a 'time slice' method outlined in Longerich et al (1996a). This method enables the identification of anomalous trends that may be caused by mineral inclusions (Figure 3.8).

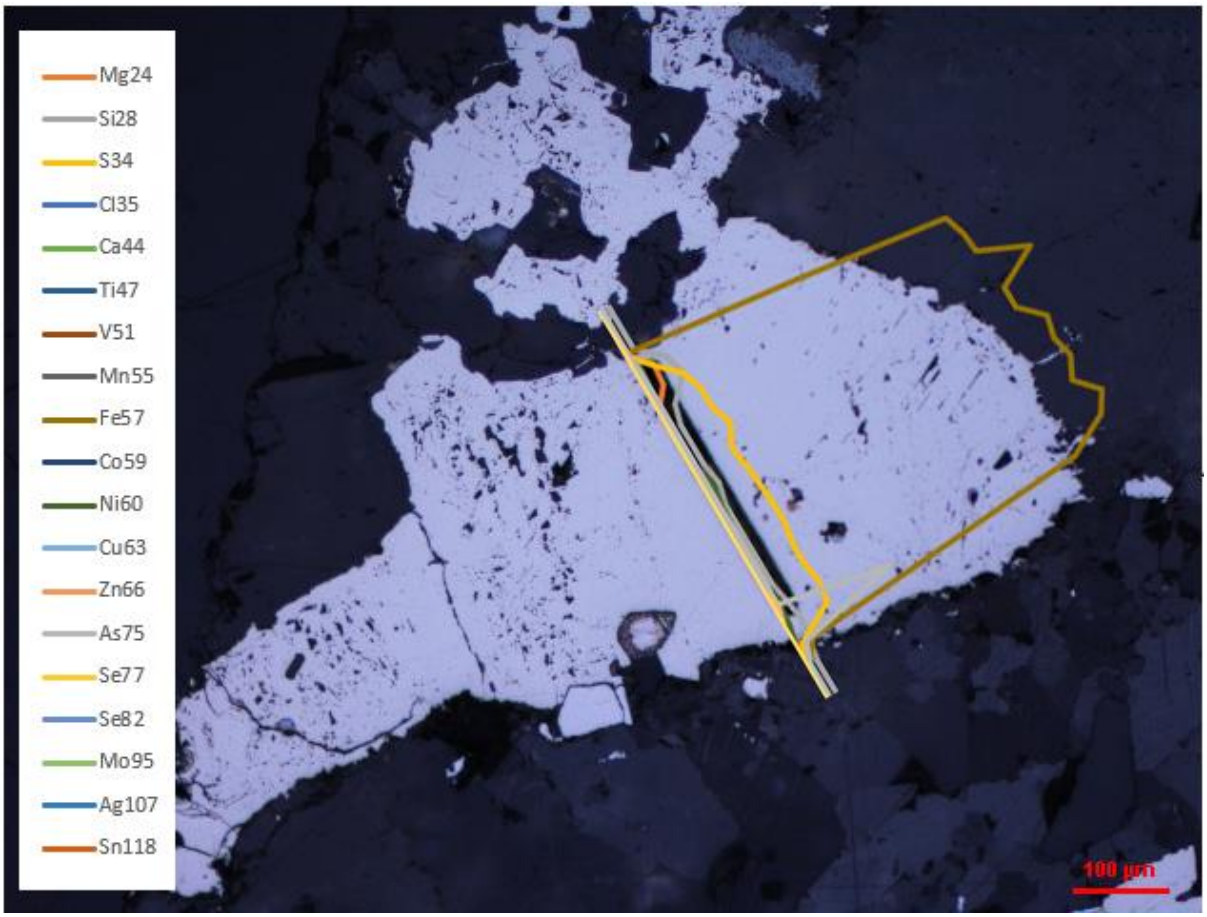

Figure 3.8: XPL image at 100µm showing Stage 4 pyrite from sample 364 with CPS from LA-ICPMS overlain to show relative homogeneity in element traces.

Pyrite and pyrrhotite crystals were ablated by a Lambda Physik Laser ablation system and traverses were selected to avoid large inclusions, however small (under 10s) spikes due to mineral inclusions were unavoidable. This ArF laser operated at 193nm with an energy output of 45mJ. The sample was initially transported in a H-He-Ar mixture to the Agilent Technologies 7700 series quadrupole. NIST SRM -610 and iron sulfide pellet MASS-1 were employed as standards and measure at the beginning, after every 6 traverses and at the conclusion of the session. These standards were then compared to published values (Jochum et al. 2005) to ensure acceptable homogeneity for the elements analysed. Iron was used as the internal standard normalisation element. Elements analysed include ^{59}Co, ^{60}Ni, ^{65}Cu, ^{77}Se, ^{82}Se, ^{49}Ti, ^{51}V, ^{55}Mn, ^{64}Zn, ^{75}As, ^{95}Mo, ^{107}Ag, ^{118}Sn, ^{121}Sb, ^{130}Te, ^{182}W, ^{197}Au, ^{208}Pb, ^{209}Bi and all produced

results within error and limits of detection (Appendix 2 Table 3.3 and Table 3.4). Raw CPS signals were reduced using Iolite and Igor Pro (6.34A). The aim of this software is to minimise operator errors during processing and to normalise the unknown samples to known standards.

Trace element ratios of pyrite were calculated using the absolute element concentration of individual pyrites and then an average determined for each pyrite stage to reflect the group. This was completed to determine if systematic changes in trace element concentrations are seen across stage 1 to stage 4 pyrites.

Pyrrhotite was only observed between stage 2 and 4 in the Argo samples. Partitioning coefficients between pyrite and pyrrhotite were determined using py and po average trace element concentrations from each vein stage. These changes in trace elements, if found to occur simultaneously with changes in sulfur isotopes may be attributed to redox and the preferential partitioning of trace elements.

3.3 RESULTS

(APPENDIX 2 CONTAINS ALL RESULTS)

Stage 1 pyrite $\delta^{34}S$ range from -0.36 to 3.47 per mil (Figure 3.9), with the highest average concentrations of Co (4126 ppm), As (1880 ppm), Sb (6.11ppm) and Pb (112ppm). Stage 2 $\delta^{34}S$ pyrite ranges from 3.37 to 6.45 per mil, and the highest average concentrations of Mg (189 ppm), Ni (748 ppm), Zn (29 ppm), Sn (0.46ppm) and W (54 ppm). Stage 3 pyrites have a $\delta^{34}S$ range of 4.15 to 9.3 per mil, and the highest average concentration of Cu (412 ppm). Stage 4 pyrites show the greatest $\delta^{34}S$ range (5.67 to 12.29 per mil) and the highest average concentrations of V (24 ppm), Mn (9 ppm), Mo (24 ppm), Ag (116 ppm), Sb (6 ppm), Te (21 ppm) and Au (5 ppm).

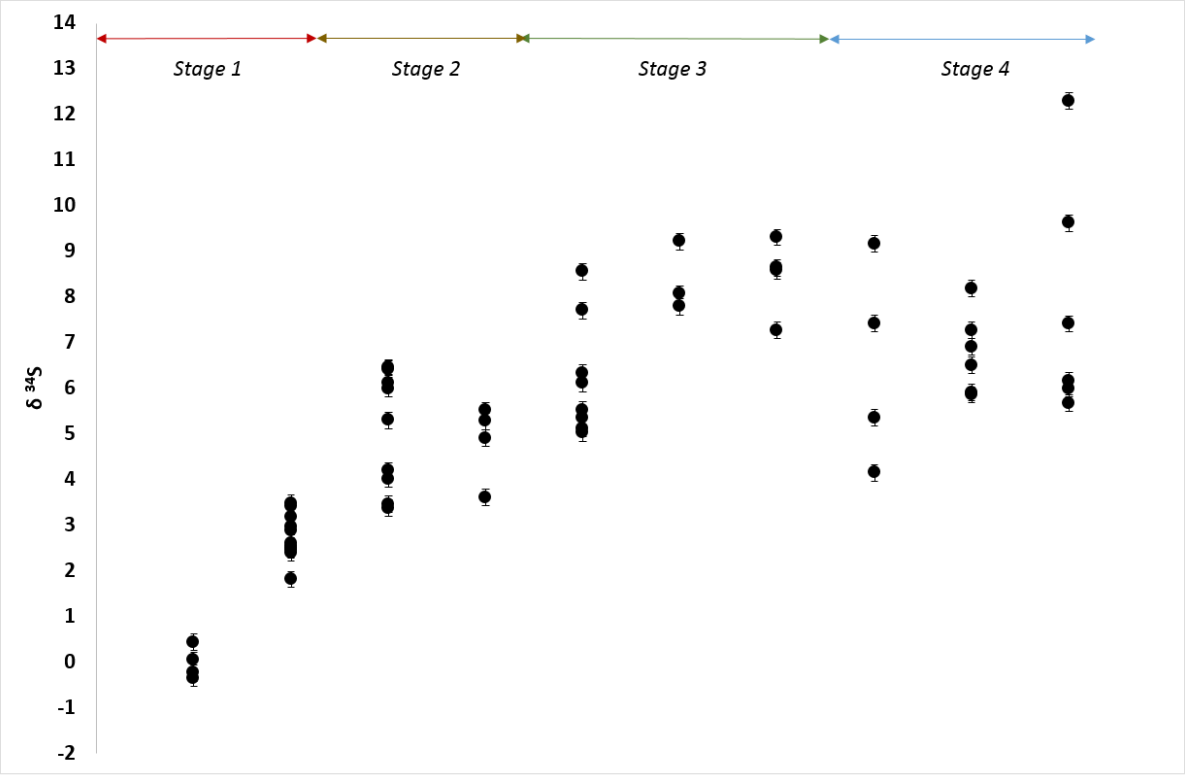

Figure 3.9: δ34S vs pyrite stages 1-4 (left to right) measured by SHRIMP-SI by 3 and 10 m spots, including 10 sample traverses. Error bars are shown (no more than 0.8 on 3 micron burns), although most errors plot within data points.

Gold and Mo concentrations increase systematically across the 4 stages, while As concentrations decrease (Figure 3.10). Cobalt, Pb and Pt concentrations decrease towards stage 4. Silver and Te concentrations increase with each stage. Manganese, Zn, Sn, Sb and Ni concentrations all increase by stage 4. Bismuth and W concentrations do not change across generations.

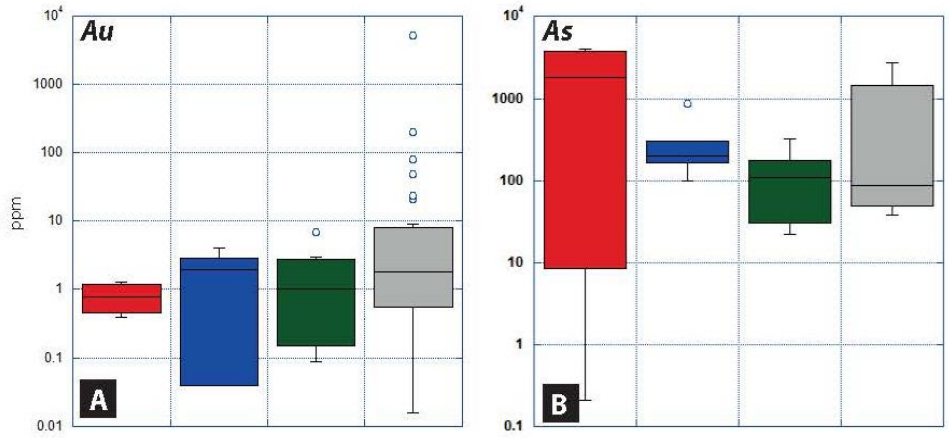

Figure 3.10 Box and whisker plots of Au (left), and As (right) of pyrite across the paragenesis, as measured by LA-ICPMS.

Stage 2 pyrrhotite has the highest Zn (1160ppm), Mo (0.73ppm), Ag (5ppm), Sn (61ppm), Sb (27ppm) W (1600ppm), Au (12) and Pb (550 ppm) concentrations. Stage 3 pyrrhotites are the highest in Ni (1417ppm) and Bi (0.52ppm). Stage 4 pyrrhotites are the highest in Pt (62ppm), Te (17ppm), Se 82 (94ppm) Se 72(52ppm), As (325ppm), Cu (44ppm) and Co (2479ppm). Co concentration increases systematically throughout.

Partition coefficients (D) defined below (Equation 1) determined for the pyrite-pyrrhotite pairs in Stages 2, 3 and 4 are listed in Table 3.1 for As, Co, Ni, Au and Sn concentrations.

Equation 1 **D (partition coefficient) = Concentration of I $_{(pyrite)}$/ Concentration of I $_{(pyrrhotite)}$**

A systematic decrease in D of As, Co and Ni is seen from stage 2 to 4 (Table 3.1 and Figure 3.11). There is also a gradual increase in D of Sn and Au from stage 2 to 4. Au preferentially

partitions into pyrrhotite in Stage 2 and pyrite in stages 3 and 4. The highest average gold in pyrite occurs in stage 4. The ratio of D_{Au}/D_{As} shows a consistent decrease (Figure 3.11). In Stage 3 the ratio between the two coefficients is 1, which is the only stage containing high-grades of native gold. This ratio is highest in Stage 4, which contains the highest concentrations of gold in pyrite.

Table 3.1: Partitioning Coefficient (D) for the pyrite –pyrrhotite pairs for stages 2,3 and 4 at Argo (*denotes where pyrrhotite becomes dominant)

	As	Co	Ni	Sn	Au	DAu/As
Stage 2	3.6	2.8	10.0	0.01	0.1	0.04
Stage 3	2.9	1.3	0.4	0.9	3.0	1.0
Stage 4	1.8	0.04	0.1	1.1	8.0	4.4

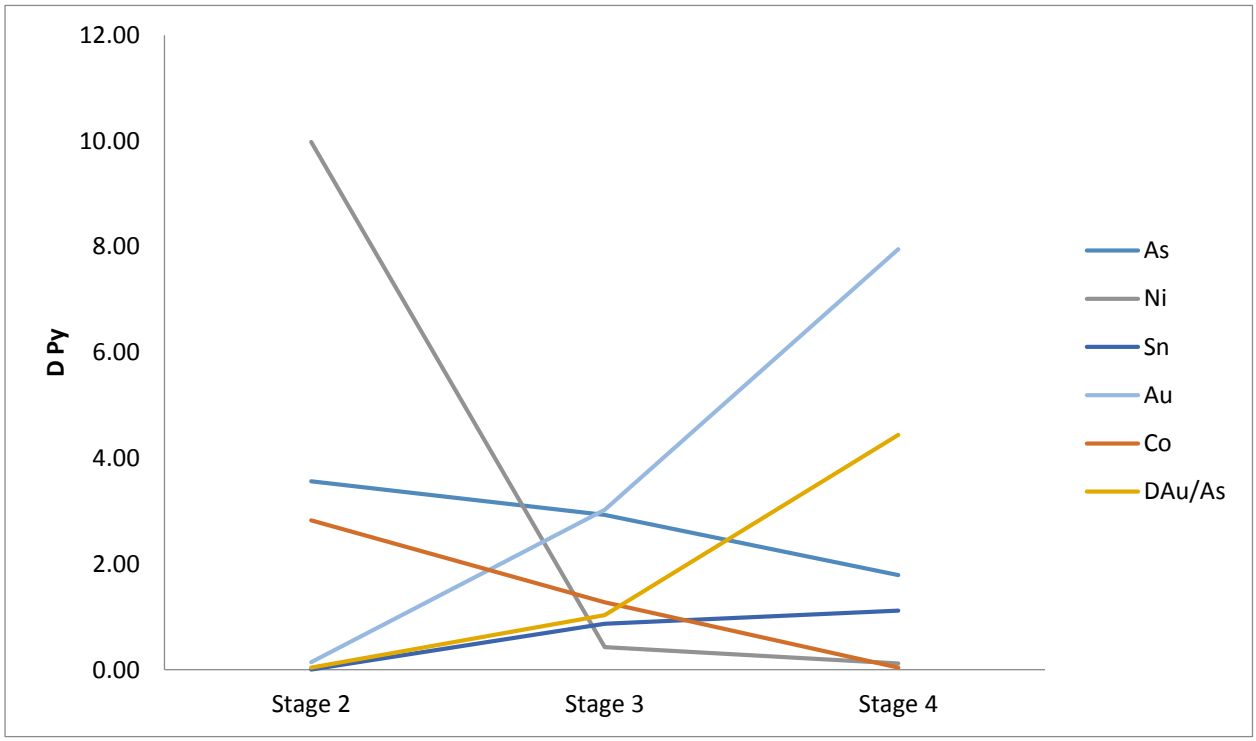

Figure 3.11: A) Line plot depicting the change of DPy (partitioning coefficients) between pyrite and pyrrhotite with the successive stages.

The clearest changes in trace element concentration are observed via the ratios in Figure 3.12. As/Ni, Co/Ni, Pb/W and As/Sb all display broad trends decreasing from Stage 2 to 4. The opposite is observed in Ag/Zn.

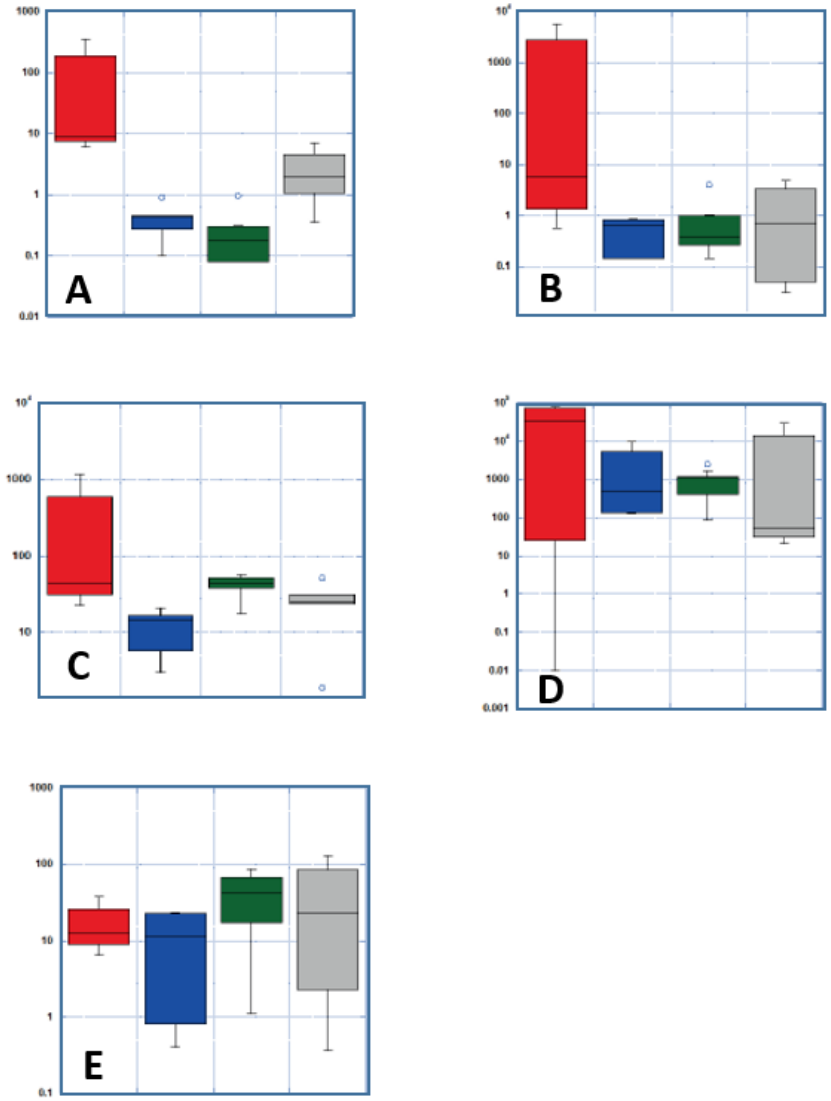

Figure 3.12: Box and whisker plots of element ratios of pyrite across four pyrite stages A) As/ Ni, B) Co/Ni, C) Pb/W, D) As/Sb and, E) Ag/Zn.

Progressive change of sulfur isotopes (Figure 3.9) and trace elements (Figure 3.12) in pyrite are recorded within individual crystals in every stage of the vein paragenesis. Progressive changes in trace element abundances are observed between Stages 2- 4 of the vein

paragenesis, specifically the appearance of pyrrhotite. These changes in trace elements between subsequent pyrite and pyrrhotite vein generations are attributed to gradual wall rock alteration and reduction of the fluid, prompting deposition (Bath et al., 2013; McGoldrick et al., 2013a; Palin and Xu, 2000). Trace element relationship between co-existing pyrite and pyrrhotite reflects gradual reduction observed at Argo and resulted in the deposition of economic gold.

3.4 DISCUSSION

Trace element and isotopic trends at Argo, WA

The sulfur isotopes were acquired using a small spot (i.e 3-10 µm) thereby minimising averaging across pyrite zones. The results observed display a significantly greater range in δS^{34}, i from 12.2 to -0.36 ‰ rather than that identified by Crawford for Argo (3.1-7.3 ‰) and Neumayr et al. (2008) for the nearby St Ives region (5.1 to -8 ‰). Sulfur isotopes of each pyrite stage overlap the previous set, supporting an incremental change of sulfur across the generations. The variation from negative Stage 1 pyrites to positive Stage 2 pyrites is consistent with the mineralogical changes seen from hematite in stage 1 to pyrrhotite in all subsequent stages.

Sulfur fugacity affects the transport and fractionation of metals in magmatic- hydrothermal fluids (Pokrovski et al., 2008; Pokrovski et al., 2005). It has been suggested that at relatively low temperatures (350-400°), low concentrations of sulfur can effectively mobilise and concentrate metals such as Cu, Au and Pt within acidic solutions enabling them to bind with reduced sulfur species such as H_2S (Pokrovski et al. 2005). Reduction due to bacteria in the Archean Witwatersrand basin was shown to trap Au in pyrite as 'invisible Au' and accumulate trace elements such as Sb, Mo, Ag, Mn and Cu (Agangi et al., 2015). Argo has a thick lithologic column (approximately 7km) providing an ample source of Fe and continual fluid input delivers consistent sulfur.

Moving from the Py-Hm-Mt triple point on **Error! Reference source not found.** towards the Py-Po-Mt triple point, regardless of temperature and pressure, is achieved via reduction of oxygen and sulfur (Crerar et al. 1978) . This mineralogical change defines the Argo system, as

pyrite and pyrrhotite are co-precipitated, we can assume that the changes in pyrite trace elements are due to changing fO_2 and partitioning between the two phases.

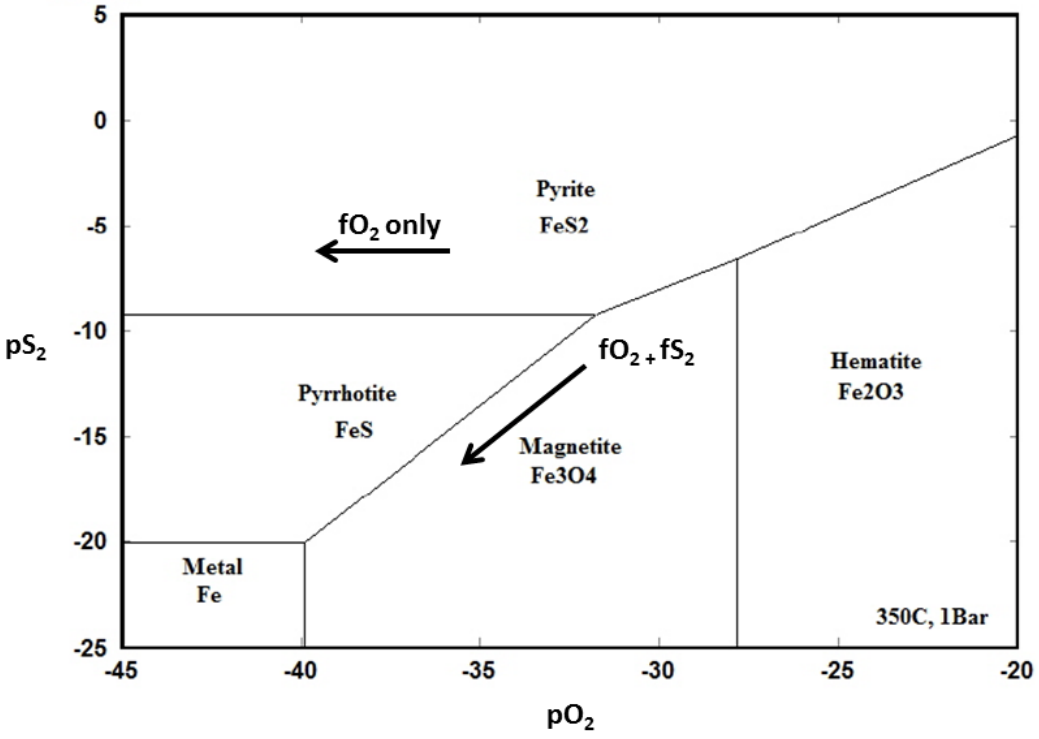

Figure 3.13: Fe-S-O stability diagram at 350 Celsius and 1 Bar. Horizontal arrow depicts change in oxygen fugacity within pyrite and pyrrhotite while diagonal arrow depicts changes in oxygen and sulfur fugacity in pyrrhotite.

The changes in partitioning between pyrite and pyrrhotite are then the result of reduction in oxygen and sulfur fucagity. The change in oxygen fugacity is much greater than the change in sulfur fugacity. *We assume a constant sulfur fugacity as there is continuity of the assemblage FeS_2 +/- FeS, however we suggest that there is a desulifidation process occurring during progressive deposition of each stage of pyrite*. Oxygen fugacity during stage 3 and 4 of the main gold event is most likely controlled by the following equation;

$$4Fe_3O_4 + O_2 \rightleftharpoons 6Fe_2O_3$$ **(Einaudi et al. 2005)**

De-sulfidation of the fluid is best controlled by the following equation:

$$2FeS + S_2 \rightleftharpoons 2FeS_2$$ **(Einaudi et al. 2005)**

The interaction between oxidation and de-sulfidation is shown in the following equation of Crerar et al. (1978);

$$0.5Fe_3O_4 + 1.5FeS_2 \rightleftharpoons 3FeS + O_2\ (g)$$ **(Crerar et al. 1978)**

The pH as discussed previously, is weakly acidic and is most likely controlled by silicate assemblages or CO_2 pressure (Hall, 1986). Thus, during Au deposition (i.e in the presence of FeS_2- FeS) the reduced equation can be written as;

$$0.5FeS + 0.25FeS_2 + H_2O \rightleftharpoons 0.25Fe_3O_4 + H_2S_{(aq)}$$ **(Crerar et al. 1978)**

By buffering the fluid's oxygen fugacity and ensuring sulfur is reduced (H_2S), gold bi-sulfide is stable (Loucks and Mavrogenes, 1999).

$$Au_{(s)} + 2H_2S_{(aq)} = HAu(HS)^0_2 + 0.5H_{2\ (aq)}$$ **(Hayashi and Ohmoto, 1991)**

Thus, reduction and desulfidation (i.e removal of sulfur from the fluid) is the main driver for gold deposition.

Pyrite trace elements show systematic changes, the most significant between Au and As. It is expected that in a pyrite-only system, Au and As are coupled during crystallisation, thus as gold deposition occurs via reduction, so too should As. This is not the case as As decreases with respect to Au concentration. There were no observable As-S minerals in the samples collected, so it follows that As partitioned into pyrrhotite and arsenopyrite. With the co-precipitation of Fe-S, ratios previously understood to follow redox changes in pyrite are not as clear, i.e As/Ni , Co/Ni and Pb/W (Figure 3.12 A, B and C)(Ward et al., 2017). More sensitive

trends in As/Sb and Ag/Zn appear to better track systematic redox changes in pyrite in a multi-Fe-S sulfide deposit (Figure 3.12 D and E).

Neumayr et al (2008) assert that gold is destabilised and deposited consistently where fluids of contrasting redox mix. As previously stated, the greatest concentration of Au at Argo is attributed to the D_3 structural event, which resulted in significant structural deformation and subsequent episodic fault-valve behaviour. Only stage 3 veins contain native Au with co-precipitated pyrite and pyrrhotite. We assert that Argo underwent continual delivery of hydrothermal fluids that interacted with the host rock resulting in systematic reduction, rather than the mixing of two fluids. The partition coefficient for Au for stage 2, 3 and 4 displays this relative redox change and identifies that sulfide assemblage plays a vital role in trace element behaviour.

The role of partitioning during deposition

The relationship between high gold and high As concentrations is well established (Belousov et al., 2016; Deditius et al., 2014; Peterson and Mavrogenes, 2014; Pokrovski et al., 2008; Ward et al., 2017). At Wallaby there was no significant competition for chalcophile trace elements such that Au crystallised with arsenian pyrite due to the preferential electro-chemical configuration i.e, As ion is postulated to be more electro-negative then S (2.58), thereby attracting Au. At Argo the high gold concentrations in pyrite do not correlate with the highest As concentrations in the same pyrites but rather, contain less Au. The difference in trace element behaviour of Argo vs Wallaby is shown in Figure 3.14. Pyrite As/Ni increases at Wallaby, but decreases at Argo. This is due to decreasing partitioning of As between py and po at Argo (Table 3.1), which is also observed for Co and Ni which prefer arsenopyrite and pyrrhotite respectively (Hawley and Nichol, 1961).

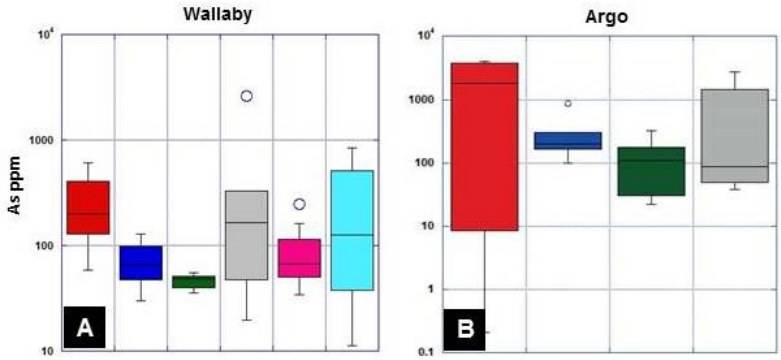

Figure 3.14: A) Boxplot of increasing average As ppm in each consecutive mineralised pyrite stage at Wallaby during gradual reduction B) Boxplot of decreasing As ppm in each consecutive mineralised pyrite stage at Argo during gradual reduction

We explain this trend through two mechanisms; preferential partitioning between sulfides driven by mineral chemistry and competition for similar sized atoms to fill vacancies. The gradual change in partition coefficients for As between stages 2 to 4 and the appearance of arsenopyrite (FeAsS) in Stage 3 provided further competition for As. Antimony also readily substitutes for S in pyrite (Abraitis et al., 2004) and is expected to mimic the behaviour of As, although it appears to partition more strongly into pyrite at Argo (Table 3.1). Mineral structures and electronegativity are also a likely driver of element partitioning. Nickel strongly partitions into pyrrhotite since it is ferromagnetic and is attracted to magnetic minerals such as pyrrhotite. At Wallaby, Ni displays the same trend with redox, in that Ni partitions into pyrite under oxidising conditions but is not found in more reduced assemblages. While pyrrhotite was not identified at Wallaby, there is a high concentration of magnetite, which also concentrates Ni (Boutroy et al., 2014).

Mineral structures can also drive partitioning of trace elements by providing appropriate bonding angles to accommodate specific trace elements. Thus, despite pyrite (NaCl structure) and pyrrhotite (Ni-As structure) both consisting of Fe-S bonds, the lattice in which they sit controls the atomic radii able to substitute in, according to Goldschmidt's rules, thus it follows that oxidation state affects the ability of a mineral to accommodate any particular trace

element. It is these preferences that control trace element partitioning and this is what changes during reduction and subsequent deposition.

As desulfidation occurred, continuous fluid input provided trace elements of similar atomic radii (i.e As and Sb). Pyrite is a versatile mineral that can readily substitute trace elements for Fe or S. Thus, if one major element is deficient in a fluid, an alternate element of similar size can replace it in pyrite. It is this substitution process that extends the period over which pyrite can form during desulfidation. At Wallaby, while desulfidation triggered gold deposition, As concentrations significantly increased in pyrite. However, at Argo, arsenic partitioned into pyrrhotite rather than pyrite (Table 3.1).This is supported by experiments that show that sulfur deficient environments allow greater trace elements, specifically As, enrichments in magmatic systems (Simon et al., 2007),

Co/Ni is considered an indicator of ore genesis (Bajwah et al., 1987; Loftus -Hills and Solomon 1967), with ratios in pyrite >5 being of volcanic origin, and anything below considered sedimentary or hydrothermal in origin. Co/Ni at Argo does not exceed 0.3, consistent with its hydrothermal origin. At Argo, due to competition between minerals during the latter stages of mineralisation, cations such as Co^{+2} partition into arsenopyrite over pyrite (Gavelin, 1947) and Ni^{+2} partitions into pyrrhotite and/or pendlandite if present (Boutroy et al. 2014). Thus, the mineral assemblage rather than source determines Co/Ni in Argo pyrites.

Comparison to other Archean lode Au deposits

Archean lode or “orogenic” gold deposits are dominantly controlled by regional scale compressional events related to terrane accretion (Kerrich and Cassidy, 1994; Moritz, 2000). Lode Au deposits form via faults that function as hydrothermal fluid conduits (Cox, 2010; Cox and Ruming, 2004). Their mineralogy is simple, consisting mainly of quartz, carbonates and

sulfide minerals. The Au - As association in these deposits is beyond question (Belousov et al., 2016; Deditius et al., 2014; Keith et al., 2018), however while this study confirms that Argo contains native gold in veins, as do most Archean deposits, invisible gold is often underestimated in other minerals such as pyrite and pyrrhotite. This study outlines how the mode of Au precipitation (i.e. free gold vs 'invisible' Au) reflects depositional mechanisms. Although stage 3 contains native gold, it does not show the highest gold concentrations in pyrite or pyrrhotite. Rather, stage 4 pyrites show the highest concentrations of gold and py-po partitioning coefficients, suggesting that reduction is not solely responsible for the deposition of Au in the Fe-S-O system but that the mineral phases control partitioning and ultimately Au enrichment.

Sulfur isotopes have been shown to vary within orogenic gold deposits of all ages and locations (Nesbitt, 1991; McCuaig and Kerrich 1998). Moritz (2000) surmises that observed isotopic differences are due to varying hydrothermal fluids and wall-rock compositions. We assert that the change in sulfur isotopes documented at Argo show the extreme wall rock – fluid interactions produced by a fault-valve system, which creates predictable redox gradients (LaFlamme et al. 2018). Argo is similar to Junction, an orogenic Au deposit of the southern St Ives gold region that contains reduced assemblages (Py-Po) (Neumayr et al. 2008), although the $\delta^{34}S$ range for Argo is greater, most likely due to individual pyrite analyses, as opposed to bulk.

The Argo and Junction deposits flank the relatively more oxidised central St Ives gold deposits (Hm-Py- Mt) containing the Victory-Defiance and Greater Revenge Au deposits. The traditional view of hydrothermal alteration describes wall rocks undergoing changes on different scales, intensity and mineralogy depending on fluid volume (McCuaig and Kerrich,

1998), which becomes problematic in deposits with multiple stages of alteration. The reduced deposits (Argo, Junction and Wallaby) and the oxidised deposits (Victory-Defiance and Greater Revenge) both show Au associated with the most 'reduced' mineral assemblage (Ward et al. 2017; Neumayr et al. 2008). At Argo, we distinguish broad groups of mineralisation based upon systematic chemical changes in pyrite due to cyclic fluid pumping through the deposit, similar to that observed at other St Ives deposits, i.e Wallaby (Ward et al. 2017) and Kapai (Gregory et al. 2016). However, at Argo, unlike the other deposits, it contains pyrrhotite, such that pyrite chemistry alone does not track ore fluid behaviour.

Global Context

The changes in As/Ni, Co/Ni, As/Sb, Pb/W and Ag/Zn seen at Argo are not attributed to nano-inclusions in pyrite but are attributed to systematic changes within the FeS_2 lattice (Deditius et al., 2011; Reich et al., 2005). This is similar to the As-rich pyrite and arsenopyrite containing 'invisible' gold at Sunrise Dam, a multi-stage Archean gold deposit in WA (Sung et al., 2009). At Sunrise Dam, anomalous trace elements in pyrite are attributed to the host rock and fluid-wall rock interaction, however the elements of interest include Bi and Te, which are both redox sensitive (Skirrow and Walshe, 2002). Anomalies in Argo's trace element attenuation in pyrite are due to competition for similar substrates during crystallisation in the later stages of ore formation.

The appearance of pyrrhotite at Argo is most likely due to reduction of the hydrothermal fluid causing an increased rate of S substitution within the pyrite lattice to account for the deficit. At Wallaby (WA), there was higher sulfidation, which prevented the formation of pyrrhotite and arsenopyrite. At Argo, where there was competition for trace elements, partition coefficients distinguish uneconomic (D_{Au}/D_{As} = <1) from economic (D_{Au}/D_{As} ≥1) pyrite stages.

Prendergast (2007) suggested As, Sb, W and Mo as pathfinder elements of gold mineralisation in the St Ives goldfield. However, bulk analyses often skew data by diluting the concentrations of trace elements, while a monomineralic study using trace elements (including ratios) and partition coefficients as demonstrated here would overcome dilution. A significant advantage of partition coefficients is their non-dependence on concentration. Thus, significant swings in concentrations are avoided by their use.

3.5 CONCLUSIONS

Argo, a mesothermal gold deposit, formed within a 'fault-value' system, in which hydrothermal fluids were episodically pumped through permeable wallrock. This established a pattern of continual reduction and resulted in systematic destabilisation of trace elements that facilitated ore deposition. Sulfur isotopes support systematic reduction via continual fluid interaction. Pyrite is present in every mineralised stage and does not solely track changes in the hydrothermal fluid due to simultaneous crystallisation of pyrrhotite. Trace element partitioning between pyrite and pyrrhotite clearly shows that preferential partitioning is driven by mineral properties (i.e magnetic, crystal structure, electro-static attraction of atomic radii) that reflect the redox conditions of the fluid during formation.

This study has shown that the accepted trace element relationship between pyrite, Au and As is not accurately recorded in the presence of pyrrhotite.

At Argo, partition coefficients better monitor changes in trace element chemistry than pyrite concentrations alone. In particular, $D_{Au\ (Py/Po)}$ increases over successive stages inversely to $D_{As(Py/Po)}$. This suggests that Au preferentially substitutes as bound gold into the most reduced pyrite, regardless of As availability.

This is similar to gold enrichment at Wallaby WA and suggests a universal pattern in hydrothermal gold deposition in redox controlled pyrite-bearing deposits.

At Argo, pyrite and pyrrhotite indicate that desulfidation during systematic reduction drove gold deposition. Gold deposition in pyrite at Argo was likely extended via the scavenging nature of pyrite and the availability of trace elements of similar size to sulfur. Further, native 'free' gold was identified in Stage 3 veins, while Stage 4 pyrites held the highest structural gold concentrations, suggesting the conditions for 'free gold' and structurally bound gold, are linked but not coeval. This author surmises that there may be a solid-solution between pyrite and Au-S and that once a substitution mechanism for Au is identified, that the concentration of Au substituted may be calculated and thus, predicted. However, this thesis can not estimate this calculation given the data collected.

This study identifies there is an element of competition during trace element uptake during crystallisation of pyrite. The pattern of trace element uptake in pyrite in deposits such as Argo, is similar to behaviour in Au deposits globally. This further supports a universal mechanism controlling trace element uptake in sulfides and thus common drivers for ore deposition, while phases present dictate how these trends are expressed. Finally, in orogenic gold deposits containing pyrite and pyrrhotite, partition coefficient ratios distinguish uneconomic (D_{Au}/D_{As} = <1), from economic (D_{Au}/D_{As} ≥1) stages.

APPENDIX 1 – DATA STATISTICS

Table 3.2: SHRIMP- SI Statistics

Title	34S/32S	95%T_err	ratio_permil	wStdErr_95 %T_permil	Corrected values	Total Error
RUT-1	0.0438150	0.000002601	-0.094	0.059	1.11	0.18
RUT-2	0.0438216	0.000002278	0.055	0.052	1.25	0.18
RUT-3	0.0438227	0.000002007	0.080	0.046	1.28	0.18
RUT-4	0.0438243	0.000002314	0.118	0.053	1.32	0.18
RUT-5	0.0438117	0.000002504	-0.169	0.057	1.03	0.18
RUT-6	0.0438220	0.000002628	0.064	0.060	1.26	0.18
RUT-7	0.0438162	0.000001854	-0.068	0.042	1.13	0.18
RUT-8	0.0438190	0.000002843	-0.003	0.065	1.20	0.18
RUT-10	0.0438197	0.00000269	0.013	0.061	1.21	0.18
RUT-11	0.0438240	0.000003134	0.110	0.072	1.31	0.18
RUT-12	0.0438163	0.000002575	-0.065	0.059	1.13	0.18
RUT-13	0.0438193	0.000002985	0.002	0.068	1.20	0.18
RUT-14	0.0438248	0.000002116	0.127	0.048	1.33	0.18
RUT-19	0.0438099	0.000002307	-0.211	0.053	0.99	0.18
RUT-20	0.0438157	0.000003232	-0.080	0.074	1.12	0.19
RUT-21	0.0438201	0.000002871	0.022	0.066	1.22	0.18
RUT-22	0.0438183	0.000002109	-0.020	0.048	1.18	0.18
RUT-23	0.0438207	0.000002227	0.035	0.051	1.24	0.18
RUT-24	0.0438150	0.000002133	-0.095	0.049	1.10	0.18
RUT-25	0.0438144	0.000002366	-0.109	0.054	1.09	0.18
RUT-26	0.0438132	0.000002975	-0.137	0.068	1.06	0.18
RUT-27	0.0438263	0.000002476	0.164	0.056	1.36	0.18
RUT-28	0.0438191	0.000002837	-0.002	0.065	1.20	0.18
RUT-29	0.0438197	0.000002916	0.013	0.067	1.21	0.18
RUT-30	0.0438247	0.000002551	0.127	0.058	1.33	0.18
RUT-31	0.0438203	0.00000243	0.026	0.055	1.23	0.18
RUT-32	0.0438234	0.000002204	0.096	0.050	1.30	0.18
RUT-33	0.0438186	0.000002234	-0.013	0.051	1.19	0.18
RUT-34	0.0438148	0.000002627	-0.099	0.060	1.10	0.18
RUT-35	0.0438210	0.000001739	0.042	0.040	1.24	0.17
RUT-36	0.0438165	0.000002541	-0.060	0.058	1.14	0.18
RUT-37	0.0438177	0.000002365	-0.034	0.054	1.17	0.18

Table 3.3: Standards from LAICPMS

	NIST 610		MASS 1	
	Average	σ	Average	σ
Mg ppm	465.33	0.58	N.S	N.S
Ti ppm	434.00	0	N.S	N.S
V ppm	442.33	0.58	50.5	8.0
Mn ppm	485.33	0.58	232.5	45.3
Co ppm	405.00	0	59.0	10.1
NI ppm	459.00	0	98.9	13.3
Cu ppm	430.33	0.58	107533.3	15756.1
Zn ppm	456.00	0	190666.7	42770.7
As ppm	317.00	0	40.1	26.4
Se ppm	109.00	0	42.9	7.6
Mo ppm	410.33	0.58	46.9	6.6
Ag ppm	239.00	0	48.1	8.1
Sn ppm	396.00	0	46.1	6.7
Sb ppm	368.00	1.73	49.1	8.2
Te ppm	320.33	0.58	18.8	2.9
Ta ppm	452.00	0	N.S	N.S
W ppm	445.33	0.58	N.S	N.S
Pt ppm	3.29	0.15	51.6	11.0
Au ppm	23.03	0.06	38.8	5.8
Pb ppm	426.33	0.58	58.8	10.2
Bi ppm	358.00	0	49.2	8.4

Table 3.4: Limits of Detection (LOD) from LAICPMS

Element	LOD
Mg ppm	2.3
Ti ppm	1.8
V ppm	0.4
Mn ppm	1.1
Co ppm	1.6
NI ppm	4.2
Cu ppm	12.2
Zn ppm	16.2
As ppm	0.8
Se 77 ppm	2.6
Se 82 ppm	3.0
Mo ppm	0.4
Ag ppm	0.2
Sn ppm	0.9
Sb ppm	0.6
Te ppm	4.5
Ta ppm	0.4
W ppm	0.4
Pt ppm	0.1
Au ppm	0.05
Pb ppm	0.5
Bi ppm	0.3

APPENDIX 2 – DATA

Table 3.5: SHIMP-SI data

Title	34S/32S	95%T_err	wStdErr_95%T_permil	Values
ANU234_1	0.044091257	0.000003	0.07	7.41
ANU234_2	0.044036352	0.000002	0.05	6.16
ANU234_3	0.044015013	0.000003	0.07	5.67
ANU234_4	0.044028805	0.000003	0.07	5.98
ANU234_5	0.044187988	0.000003	0.06	9.62
ANU234_6	0.044305146	0.000003	0.06	12.29
ANU234.2_1	0.044084954	0.000003	0.08	7.27
ANU234.2_2	0.044051546	0.000003	0.07	6.50
ANU234.2_3	0.044069172	0.000002	0.05	6.91
ANU234.2_4	0.044025247	0.000003	0.06	5.90
ANU234.2_5	0.044023165	0.000002	0.04	5.86
ANU234.2_6	0.044125113	0.000004	0.09	8.18
AS21287_1	0.043942358	0.000002	0.06	4.01
AS21287_2	0.043917863	0.000002	0.05	3.45
AS21287_3	0.043914224	0.000003	0.06	3.37
AS21287_4	0.043950361	0.000003	0.07	4.19
AS21287_5	0.044049262	0.000003	0.06	6.45
AS21287_6	0.044034384	0.000002	0.05	6.11
AS21287_7	0.044028835	0.000003	0.06	5.98
AS21287_8	0.044047756	0.000003	0.07	6.42
AS21287_9	0.043998442	0.000003	0.07	5.29
12005A_2	0.044101823	0.000007	0.17	9.21
12005A_3	0.04404761	0.000007	0.15	8.06
12005A_4	0.044031874	0.000008	0.19	7.79
12500A3_1	0.044089892	0.000007	0.16	9.30
12005A3_2	0.043996622	0.000009	0.20	7.26
12500A3_3	0.044050025	0.000008	0.18	8.58
12500A3_4	0.044048399	0.000008	0.18	8.64
ARGO-276-1	0.043969566	0.000009	0.20	5.52
ARGO-276-2	0.043961708	0.000009	0.21	5.34
ARGO-276-3	0.043951962	0.000009	0.21	5.12
ARGO-276-4	0.043947386	0.000008	0.18	5.01
ARGO-276-5	0.043994926	0.000008	0.18	6.10
ARGO-276-6	0.044064898	0.000007	0.16	7.70
ARGO-276-7	0.044004901	0.000009	0.21	6.33
ARGO-276-8	0.044102466	0.000009	0.19	8.56
ARGO-380-1	0.043711888	0.000011	0.26	-0.36
ARGO-380-2	0.043729537	0.000012	0.27	0.04
ARGO-380-3	0.043746683	0.000011	0.26	0.43
ARGO-380-4	0.04371705	0.000015	0.34	-0.25
ARGO_266_1.1	0.043987261	0.000018	0.41	5.50
ARGO_266_1.3	0.043977286	0.000017	0.38	5.28

ARGO_266_1.4	0.043904045	0.000016	0.36	3.60
ARGO_266_1.5	0.043960911	0.000014	0.31	4.90
ARGO_12005A_1.1	0.043927878	0.000018	0.41	4.15
ARGO_12005A_1.2	0.044071003	0.000015	0.34	7.42
ARGO_12005A_1.3	0.043980618	0.000020	0.46	5.35
ARGO_12005A_1.4	0.044147594	0.000019	0.43	9.16
ARGO_033A_1.1	0.043885171	0.000019	0.43	3.17
ARGO_033A_1.2	0.043876098	0.000018	0.42	2.97
ARGO_033A_1.3	0.043895024	0.000017	0.39	3.40
ARGO_033A_1.4	0.043898372	0.000019	0.42	3.47
ARGO_033A_1.5	0.043860214	0.000014	0.33	2.60
ARGO_033A_1.6	0.04385337	0.000016	0.36	2.45
ARGO_033A_1.7	0.043854882	0.000018	0.41	2.48
ARGO_033A_1.8	0.043850868	0.000014	0.33	2.39
ARGO_033A_1.9	0.04385724	0.000014	0.32	2.54
ARGO_033A_1.10	0.043871892	0.000021	0.47	2.87
ARGO_033A_1.12	0.043825373	0.000020	0.46	1.81

Table 3.6: Stage 1 Pyrite LA-ICPMS results

	Stage 1 Pyrite Samples					
	AS21776-1.d Pyrite	AS21776-2.d Pyrite	033A-1.d Pyrite	033A-2.d Pyrite	Average	St.Dev
Element	**1**	**1**	**1**	**1**		
Mg ppm	11.70	82.00	4.03	1.35	**24.77**	**38.40**
Ti ppm	1148.00	1780.00	14.32	12.85	**738.79**	**876.25**
V ppm	1.54	3.77	0.06	0.03	**1.35**	**1.76**
Mn ppm	3.05	7.20	5.50	0.41	**4.04**	**2.96**
Co ppm	15970.00	204.00	225.30	103.16	**4125.62**	**7896.44**
Ni ppm	2.80	96.10	401.00	10.81	**127.68**	**187.04**
Cu ppm	28.00	14.10	28.10	283.00	**88.30**	**129.97**
Zn ppm	2.00	2.80	0.53	1.96	**1.82**	**0.94**
As ppm	16.59	0.21	3552.00	3951.00	**1879.95**	**2167.22**
Se 77 ppm	23.60	38.40	57.00	27.00	**36.50**	**15.06**
Se 82 ppm	24.50	39.20	21.33	27.57	**28.15**	**7.79**
Mo ppm	0.00	0.05	0.52	0.49	**0.27**	**0.28**
Ag ppm	22.80	18.20	20.22	27.57	**22.20**	**4.05**
Sn ppm	0.26	0.42	0.26	0.18	**0.28**	**0.10**
Sb ppm	0.34	24.00	0.05	0.05	**6.11**	**11.93**
Te ppm	18.10	2.70	7.58	2.69	**7.77**	**7.26**
W ppm	2.07	8.60	0.01	0.00	**2.67**	**4.07**
Pt ppm	0.65	0.29	0.07	0.00	**0.25**	**0.29**
Au ppm	1.28	0.38	1.04	0.52	**0.81**	**0.43**
Pb ppm	9.30	392.00	39.90	7.58	**112.20**	**187.13**
Bi ppm	0.41	0.34	0.85	0.19	**0.45**	**0.28**

Table 3.7: Stage 2 Pyrite LA-ICPMS results

	Stage 2 Pyrite Samples						
Mineral Stage	AS21287-1.d Pyrite 2	AS21287-2.d Pyrite 2	AS21287-3.d Pyrite 2	266-1.d Pyrite 2	266-2.d Pyrite 2	Average	St.Dev
Mg ppm	480.00	b.l.d	450.00	3.20	11.20	**236.10**	**264.61**
Ti ppm	7200.00	1920.00	3900.00	15.30	10.64	**2609.19**	**3028.92**
V ppm	33.40	6.80	20.70	0.10	0.03	**12.21**	**14.54**
Mn ppm	6.50	b.l.d	4.02	1.84	1.80	**3.54**	**2.23**
Co ppm	301.00	484.00	578.00	130.50	144.20	**327.54**	**200.22**
Ni ppm	369.00	737.00	666.00	957.00	1013.00	**748.40**	**257.09**
Cu ppm	6.42	b.l.d	9.50	62.40	62.00	**35.08**	**31.34**
Zn ppm	12.80	120.00	10.90	0.85	0.94	**29.10**	**51.11**
As ppm	165.10	203.00	307.00	881.00	100.00	**331.22**	**316.36**
Se 77 ppm	28.52	b.l.d	17.80	15.00	12.00	**18.33**	**7.19**
Se 82 ppm	27.30	b.l.d	19.50	19.19	23.60	**22.40**	**3.84**
Mo ppm	b.l.d	0.50	b.l.d	0.71	1.10	**0.77**	**0.30**
Ag ppm	5.29	b.l.d	13.50	18.62	22.10	**14.88**	**7.30**
Sn ppm	0.79	b.l.d	0.59	0.46	0.44	**0.57**	**0.16**
Sb ppm	1.11	b.l.d	2.43	0.09	0.12	**0.94**	**1.10**
Te ppm	37.10	b.l.d	34.90	0.19	0.66	**18.21**	**20.56**
W ppm	19.80	3.70	25.40	127.30	92.70	**53.78**	**53.36**
Pt ppm	0.16	8.00	4.60	0.09	0.04	**2.58**	**3.60**
Au ppm	2.80	1.90	4.00	0.04	0.04	**1.76**	**1.73**
Pb ppm	29.30	6.00	33.00	2.86	10.73	**16.38**	**13.83**
Bi ppm	1.39	2.00	5.73	0.17	0.75	**2.01**	**2.19**

Table 3.8: Stage 3 Pyrite LA-ICPMS results

	Stage 3 Pyrite Samples												
Element	A276-5.d Pyrite 3	A276-6.d Pyrite 3	A276-7.d Pyrite 3	A276-8.d Pyrite 3	A276-9.d Pyrite 3	1200A_SH1.d Pyrite 3	1200A_SH2.d Pyrite 3	12005-10.d Pyrite 3	12005-11.d Pyrite 3	12005-12.d Pyrite 3	12005-13.d Pyrite 3	Average	St.Dev
Mg ppm	52.00	28.60	11.00	73.00	279.00	26.00	96.00	282.00	5.04	9.00	2.68	**78.57**	**104.13**
Ti ppm	11.75	23.20	13.00	13.85	217.00	128.20	1349.00	16.50	17.40	20.90	860.00	**242.80**	**444.58**
V ppm	0.24	5.20	1.53	1.84	13.60	3.22	21.30	1.00	0.75	2.95	9.60	**5.57**	**6.66**
Mn ppm	1.17	0.27	0.47	3.95	3.72	0.17	4.01	10.90	0.31	0.42	0.49	**2.35**	**3.25**
Co ppm	1590.00	175.40	146.90	362.00	532.00	88.60	1600.00	213.00	690.00	50.70	99.00	**504.33**	**574.32**
Ni ppm	404.00	244.40	356.00	364.00	502.00	343.00	390.00	1012.00	2152.00	184.00	721.00	**606.58**	**562.63**
Cu ppm	30.00	36.50	25.20	32.30	29.50	8.10	4080.00	152.00	40.80	31.90	68.20	**412.23**	**1217.06**
Zn ppm	0.43	0.34	0.33	0.68	1.55	1.75	15.70	8.50	0.54	0.76	0.82	**2.85**	**4.87**
As ppm	126.00	22.60	93.50	30.40	56.10	27.20	655.00	323.00	166.10	179.60	206.00	**171.41**	**185.04**
Se 77 ppm	13.00	1.70	8.20	1.50	3.30	19.50	21.30	11.00	9.20	9.60	13.00	**10.12**	**6.53**
Se 82 ppm	30.10	28.50	18.51	24.70	28.30	20.20	22.10	32.40	49.40	38.80	28.20	**29.20**	**8.83**
Mo ppm	2.10	1.10	0.88	1.00	1.30	b.l.d	b.l.d	1.70	1.90	2.00	1.90	**1.54**	**0.75**
Ag ppm	29.50	27.50	17.70	22.10	26.30	1.96	3.20	33.80	47.80	38.50	27.90	**25.11**	**13.73**
Sn ppm	b.l.d	0.12	0.26	0.17	0.14	b.l.d	0.15	0.18	0.28	0.50	0.50	**0.26**	**0.17**
Sb ppm	0.07	0.08	0.08	0.07	0.10	0.32	3.63	0.13	0.14	0.15	0.21	**0.45**	**1.06**
Te ppm	0.57	0.17	0.11	0.09	0.43	4.93	16.70	0.27	1.16	0.10	1.86	**2.40**	**4.95**
W ppm	15.50	0.02	b.l.d	b.l.d	1.05	0.31	2.56	b.l.d	b.l.d	b.l.d	1.37	**3.47**	**4.59**
Pt ppm	b.l.d	b.l.d	0.03	0.02	0.05	b.l.d	1.04	0.10	b.l.d	b.l.d	0.01	**0.21**	**0.31**
Au ppm	0.10	1.27	0.09	0.15	0.75	0.89	2.50	1.12	2.76	2.93	6.90	**1.77**	**2.00**
Pb ppm	7.02	4.20	1.02	2.03	5.82	3.34	27.10	6.54	6.57	3.26	17.40	**7.66**	**7.78**
Bi ppm	0.12	0.08	0.03	0.04	0.15	0.07	1.16	0.14	0.37	0.08	0.73	**0.27**	**0.36**

Table 3.9: Stage 4 Pyrite LA-ICPMS results

	Stage 4 Pyrite Samples						
Element	364-1.d Pyrite 4	364-3.d Pyrite 4	ANU234-1.d Pyrite 4	ANU234-2.d Pyrite 4	ANU234-3.d Pyrite 4	Average	St.Dev
Mg ppm	1.49	1.00	18.00	53.00	209.00	**56.50**	**87.83**
Ti ppm	11.11	21.00	1233.00	7520.00	11900.00	**4137.02**	**5341.03**
V ppm	0.01	0.20	1.84	43.50	74.60	**24.03**	**33.81**
Mn ppm	1.21	7.50	2.56	3.82	31.70	**9.36**	**12.71**
Co ppm	19.53	1.11	120.20	55.20	309.00	**101.01**	**124.85**
Ni ppm	384.50	41.00	166.60	16.70	64.00	**134.56**	**150.93**
Cu ppm	37.10	52.00	0.30	7.37	3.51	**20.06**	**23.11**
Zn ppm	0.44	4.00	b.l.d	5.63	20.70	**7.69**	**8.94**
As ppm	2702.00	b.l.d	60.50	38.30	113.90	**728.68**	**1315.93**
Se 77 ppm	21.00	95000.00	14.83	32.80	23.25	**19018.38**	**42475.02**
Se 82 ppm	19.51	30.00	15.83	30.50	17.37	**22.64**	**7.07**
Mo ppm	0.94	120.00	b.l.d	b.l.d	0.03	**40.32**	**69.00**
Ag ppm	18.60	520.00	7.72	24.40	7.64	**115.67**	**226.14**
Sn ppm	0.25	b.l.d	0.18	0.60	0.71	**0.43**	**0.26**
Sb ppm	0.09	25.00	0.92	1.81	2.74	**6.11**	**10.60**
Te ppm	0.41	b.l.d	7.61	71.10	26.60	**26.43**	**31.76**
W ppm	39.41	45.50	0.13	27.40	19.90	**26.47**	**17.80**
Pt ppm	0.05	0.28	b.l.d	0.27	0.51	**0.28**	**0.19**
Au ppm	0.05	0.14	0.70	20.80	2.77	**4.89**	**8.96**
Pb ppm	3.70	0.98	18.10	69.50	42.80	**27.02**	**28.96**
Bi ppm	0.16	0.52	0.73	1.34	1.40	**0.83**	**0.54**

Table 3.10: All stages of Pyrrhotite LA-ICPMS results

	Mineral Stage								
Element	276_q.d Pyrrhotite 2	366_1.d Pyrrhotite 3	366_2.d Pyrrhotite 3	Stage 3 Average	Stage 3 St.Dev	A234_1.d Pyrrhotite 4	364.d Pyrrhotite 4	Stage 4 Average	Stage 4 St.Dev
Mg ppm	490000	14.1	13	**13.55**	**0.78**	115	27	**71**	**62.23**
Ti ppm	394000	0.9	b.d.l	**0.05**	**1.20**	8200	b.l.d	**8200**	**N/A**
V ppm	5800	0.038	0.01	**0.02**	**0.02**	71	0.042	**35.521**	**50.17**
Mn ppm	24400	2.1	29	**15.55**	**19.02**	28	2.66	**15.33**	**17.92**
Co ppm	116	404.2	386	**395.10**	**12.87**	4900	58.9	**2479.45**	**3423.17**
Ni ppm	75	1486	1348	**1417.00**	**97.58**	1370	886	**1128**	**342.24**
Cu ppm	13.20	4.5	0.21	**2.36**	**3.03**	76	11.5	**43.75**	**45.61**
Zn ppm	1160	2.5	0.52	**1.51**	**1.40**	24	1.5	**12.75**	**15.91**
As ppm	93	52.8	64.2	**58.50**	**8.06**	600	51	**325.5**	**388.20**
Se 77 ppm	7	21.7	19.3	**20.50**	**1.70**	77	27.8	**52.4**	**34.79**
Se 82 ppm	b.l.d	40.5	36	**38.25**	**3.18**	131	57.2	**94.1**	**52.18**
Mo ppm	0.73	0.327	0.196	**0.26**	**0.09**	0.17	0.51	**0.34**	**0.24**
Ag ppm	5.30	2.7	0.6	**1.65**	**1.48**	4.3	2.2	**3.25**	**1.48**
Sn ppm	61	0.33	0.03	**0.18**	**0.21**	0.71	b.d.l	**0.71**	**0.50**
Sb ppm	27	0.192	0.04	**0.12**	**0.11**	1.34	3.3	**2.32**	**1.39**
Te ppm	b.l.d	0.12	0.44	**0.28**	**0.23**	34	0.6	**17.3**	**23.62**
W ppm	1600	0.05	0.059	**0.05**	**0.01**	37	48.1	**42.55**	**7.85**
Pt ppm	50	7	0.93	**3.97**	**4.29**	118	6	**62**	**79.20**
Au ppm	12	1.08	0.09	**0.59**	**0.70**	0.95	0.28	**0.615**	**0.47**
Pb ppm	550	5.8	1.33	**3.57**	**3.16**	21	21	**21**	**0.00**
Bi ppm	0.17	0.69	0.34	**0.52**	**0.25**	0.23	0.42	**0.325**	**0.13**

4. THE LINK BETWEEN GRANITES AND HYDROTHERMAL ORE DEPOSITS: THE LACHLAN FOLD BELT GRANITE CONNECTION

ABSTRACT

The establishment of the S- and I-type granite classifications was based upon bulk chemistry and silicate mineralogy. Sulfides are commonly identified, albeit in rare abundance. Pyrite is the most common sulfide and hosts a gamut of major and minor elements as a function of crystallisation conditions, but has been largely overlooked in the granite story and, due to its late formation, provides valuable trace element trends that can be clearly linked to redox conditions. We assert that a single mineral approach using in-situ micro-analysis reflects the reduced nature of S-type granites and the exploration potential of specific granites may be ascertained. We also suggest that the trends observed in this study suggest a universal control on partitioning of elements of economic interest in sulfides. Thus, an over-arching redox control on pyrite compositions and the link between redox states of granites and associated ore deposit type has been established.

4.1 INTRODUCTION

Granites are clearly considered the source of fluids responsible for magmatic-hydrothermal ore deposits (Blevin et al., 1996; Hedenquist and Lowenstern, 1994). However, establishing clear links between individual intrusive and specific ore deposits remains elusive. Within hydrothermal ore deposits, sulfur isotopes and trace elements of pyrite have been useful monitors of conditions attending ore deposition. In particular, stages or groups of pyrite can be effectively monitored by in situ analysis of individual pyrite grains and used to indicate geochemical conditions, such as redox (Belousov et al., 2016; Peterson and Mavrogenes, 2014; Ward et al., 2017). Given that clear redox differences have been established for the I- and S-type granites of the Lachlan Fold Belt (LFB) by Chappell and White, late stage pyrite

grains from specific granites were selected for in situ analysis. These pyrite grains link the magmatic and the hydrothermal stages since they crystallised late yet before fluid saturation. Thus, any differences in the redox of the granites reflected in these pyrite grains could control the type of mineral deposit formed by the exsolved hydrothermal fluids.

Within the LFB, S- denotes a supracrustal (sedimentary) granitic source while I- denotes an intracrustal (igneous) source (Chappell and White, 1974). In a similar manner, Ishihara (1998) separated granites into the "magnetite" vs. "ilmenite" series. The major difference being their relative redox states (Trail et al., 2015a; Whalen and Chappell, 1988). On a basic level, S-type (ilmenite) granites contain white feldspar phenocrysts (no Fe^{3+}) while I-type (magnetite) granites often contain red feldspars (Fe^{3+}). Thus, S-type (ilmenite) granites are considered reduced relative to I-type (magnetite) granites. Suites of previously categorized granites from the classic localities of the Lachlan Fold Belt (LFB) of Eastern Australia will be referred to herein as of I- or S-type.

Although ubiquitous in granites, sulfide minerals have generally been ignored, except as trace components of bulk analyses. Pyrite, the most abundant sulfide, hosts variable major, minor and trace elements, as a function of depositional conditions (Abraitis et al., 2004). This information, however, can only be extracted via small-spot in situ analyses. Ward et al. (2017) showed that sulfur isotopes and trace elements in hydrothermal pyrite vary with redox conditions. The goal of the present study is to determine if pyrite crystals formed within oxidized vs. reduced granites are distinguishable by pyrite chemistry, and if this may control the type of ore deposit formed by the associated exsolved fluids.

This paper documents a selection of pyrites from LFB granites analyzed by micro-analytical techniques; LA-ICP-MS and SHRIMP-SI. This is the first time that in situ sulfur isotope data has

been coupled with trace element trends in pyrites from felsic intrusive suites. Our results show clear differences between the 2 populations consistent with a change in redox and/or source composition. The trends observed suggest a robust sensor of redox in granites, and confirm the long-held belief that these granite types are clearly distinguished by redox. Secondly, this study establishes pyrite as a redox sensor able to monitor hydrothermal and igneous systems. While zircon monitors redox during high temperature igneous stages, pyrite monitors the later stages as the system evolves toward volatile saturation. Finally, pyrite is the ideal phase to track the behaviour of chalcophile elements in granitic systems.

4.2 BACKGROUND

It is widely accepted that I-type and S-type granites result from melting of different material and differing fractionation history (Chappell and White, 1974; Chappell and White, 1992; Collins and Richards, 2008). The major element chemistry of S-type granites is high peraluminousity (i.e., ASI>1.1) with lower Ca, Na, Sr, $Fe^{3+/2+}$ and higher concentrations of Cr and Ni compared to I-type granites from the same region (Chappell and White, 2001). S-type granites also have higher $\delta^{18}O$ and more evolved Sr and Nd isotopes relative to I-type granites (Chappell and White, 2001; McCulloch and Chappell, 1982). I- and S-type granites, traditionally categorised using whole rock geochemistry, often overlap compositionally (Blevin et al., 1996; Chappell and White, 1992), except for mafic enclaves in I-type granites, which are clearly distinct. Mafic enclaves, the initial phases of granite-magma generation (Holden et al., 1991), contain up to 3 times more Ti, Al, Mg, Fe, Ni and REE than their host (Chappell et al., 1998; Eberz and Nicholls, 1990). Ascertaining trace element concentrations of a single mineral across a suite of samples may uncover trends that have been historically overlooked, and clarify the link between magmatic processes and hydrothermal ore deposits and provide new insights into the formation of granite-related metallic ores.

For chalcophile elements, valence strongly affects melt-sulfide partitioning. Belousova et al. (2002b) used redox trends to distinguish most I-type from S-type granites, in particular, Ce^{3+} when Ce^{4+} (i.e pegmatites), behaves similarly to Zr^{4+} and is preferentially partitioned into zircon over other REE. More recently Trail et al. (2015) and Burnham and Berry (2017) showed that Ce anomalies reliably track redox conditions (Burnham and Berry, 2017). In a similar manner, hydrothermal pyrite formed during reduction showed enrichments in the redox-sensitive elements; As, Sb, and Te (Ward et al. 2017), thus, zircon signatures monitor the early stages of granite evolution while pyrite captures the late stages.

A useful measure of redox in granites is the modal abundances of magnetite, ilmenite, pyrite and pyrrhotite (Whalen and Chappell, 1988), or the magnetite-ilmenite distinction of Ishihara (1998). This distinction seems odd given that magnetite and ilmenite are not mutually exclusive phases. The Fe-Ti ternary diagram (Figure 4.1) clearly shows that under reducing conditions (WM for the wustite-magnetite buffer), the stable oxides are titanium-rich at all temperatures. However, under the more oxidized conditions of NNO (the Nickel-nickel oxide buffer) high temperature (1000°C) $magnetite_{ss}$ coexists with titanium-rich $ilmenite_{ss}$ but during cooling (600°C) the tie-lines rotate to nearly pure magnetite. Thus, oxidised systems contain magnetite (+ilmenite) while reduced granites contain no magnetite. An alternative method for determining redox conditions during granite crystallization involve directly measuring the Fe^{2+}/Fe^{3+} of powdered rock samples (reported in the Chappell database).

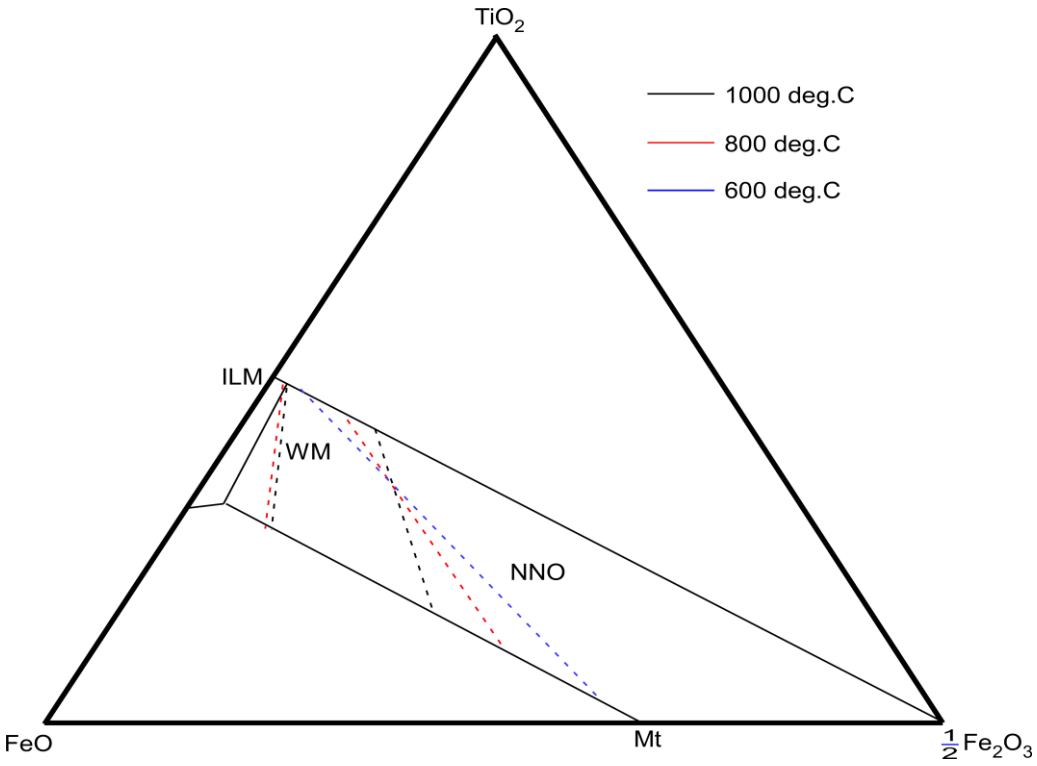

Figure 4.1: Fe-Ti oxide ternary, with tie-lines linking coexisting phases as a function of temperature (After Lindsley 1991).

The link between granite type and ore is well established (Chappell and White, 1992; Ishihara et al., 1979). The dominant relationships include Sn mineralization associated with highly silicic S-type granites and porphyry type Cu and Mo deposits associated with I-type granites (Chappell and White, 1992). Plant et al. (1990) linked S-type granites of the Pennine ore fields (Central England) to Sn mineralization, mostly due to their reduced nature. Sn^{2+} is expected to be more abundant in reduced melts than in oxidized melts where Sn^{4+} predominates. The large differences in atomic radii between $^{[VI]}Sn^{+2}$ (0.93 Å) vs $^{[VI]}Sn^{+4}$ (0.71 Å) control substitutions for $^{[VI]}Ti^{4+}$ (0.79 Å) in minerals such as titanite or rutile, according to Goldschmidt's rules (Ahrens, 1952). Thus, oxidized melts lose Sn^{4+} to Ti-bearing minerals while reduced melts retain Sn^{2+} until volatile exsolution occurs.

There are numerous hydrothermal environments in which redox clearly controls partitioning of multi-valent elements. Arsenic, for instance, is commonly found in gold-rich pyrite ores.,

As^{+3} undergoes reduction on the surface of pyrite as it bonds to both Fe and S (Bostick and Fendorf, 2003), resulting in S disproportionation, which promotes cation retention (Bancroft and Hyland, 1990). Thus, reduction promotes As precipitation, while Bi on the other hand, is precipitated due to oxidation (Skirrow and Walshe, 2002). This raises the question; do trace and stable elements in pyrite accurately reflect redox conditions during granite crystallisation?

4.3 METHODOLOGY

Granite samples were collected from established LFB localities. Samples were chosen from the Chappell database and include the most oxidised (Braidwood) and most reduced (Jillamatong) examples identified within that collection (Chappell et al., 1991; Trail et al., 2015b). Sample locations are shown in Figure 4.2 and GPS coordinates in Table 4.1.

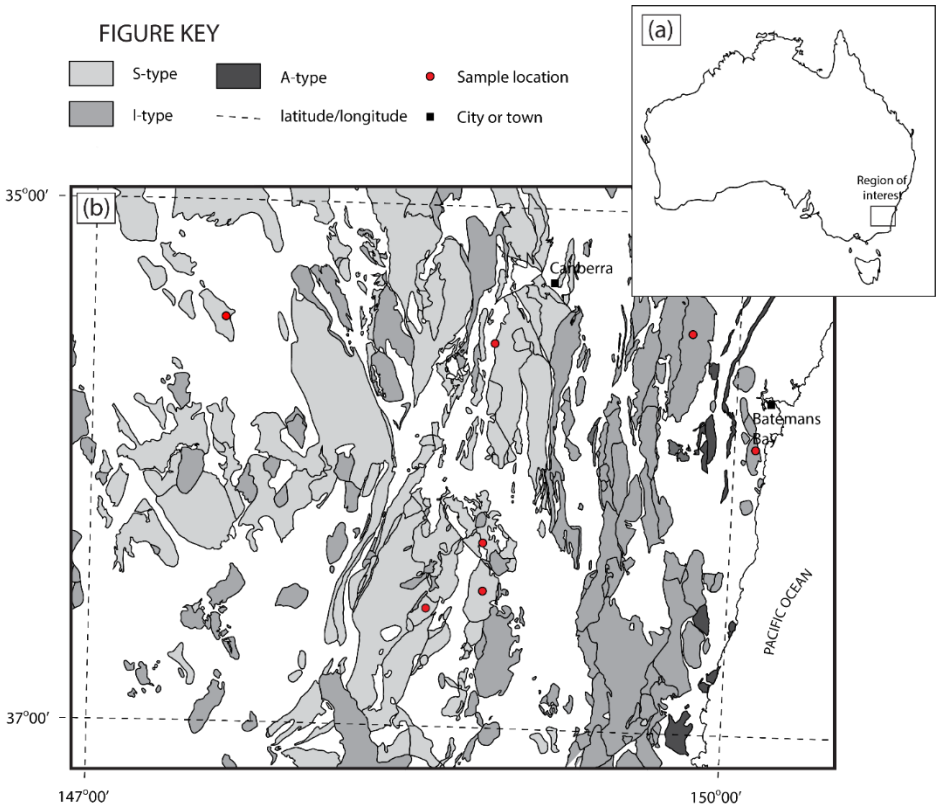

Figure 4.2: Simplified geologic map of granitoid types and sampling locations from this study. Red dots indicate sampling localities, dark grey = A-type plutons, mid-grey = I-type plutons and light-grey = S-type plutons. Image modified after Chappell et al. (1990)

Table 4.1: GPS coordinates of samples and SIAM classification (* Chappell reference number). A full list of samples and associated analyses are found in (Appendix 1).

Sample #	Name	GPS Southing (Datum = WGS84)	GPS Easting (Datum = WGS84)	Classification
W058	Cootralantra Granodiorite	36° 16'74'' S	148° 45' 25.9''E	S
W063	Dalgety Granodiorite	36° 29'36.3'' S	148° 50' 23.4''E	S
W073	Shannons Flat	35° 31'43.2'' S	148° 53' 54.9''E	S
W118	Braidwood Granodiorite	35°29'06.1" S	149°47'02.8"E	I
W120	Moruya Tonalite	35°54'15.0" S	150°06'49.1"E	I
W139	Kyeamba Monzogranite	35°30'30.4" S	147°33'49.9"E	S
KB32*	Jillamatong Granodiorite	36° 31'28'' S	148° 35'79'' E	S

* Chappell Sample Reference Number

Samples, provided by Nick Tailby (American Museum of Natural History), were cut, set in mounts and polished to 0.25 µm and studied by reflected light microscopy, Scanning Electron Microscopy (SEM), Laser Ablation Inductively Coupled Mass Spectrometry (LA-ICP-MS) and Sensitive High Resolution Iron Micro-Probe Stable Isotope (SHRIMP-SI) analysis. A complete list of pyrite samples and the analyses performed are found in Appendix 1.

Multiple interstitial pyrite grains from selected granites were identified under reflected light and documented with associated Fe-Ti-Oxides (Figure 4.4). S-type granites saturate in sulfur earlier than I-type granites, while, I-type granites contain higher sulfur concentrations pre-sulfide saturation due to their higher intrinsic oxygen fugacity (Wyborn, 1994). Given that pyrite is unstable at temperatures above 750 °C (Kullerud and Yoder, 1959) pyrite only forms during the late stages of crystallisation. Pyrites in this study were selected to avoid inclusions and found within fine-grained quartz groundmass and were not observed as inclusions in phenocrysts.

SHRIMP-SI

SHRIMP-SI was used to measure $\delta^{34}S$ using a 10µm spot on Al-coated polished mounts for a selection of S and I-type pyrites over a 24-hour period (Table 4.9 Appendix 2). Pyrite from Ruttan, Manitoba ($\delta^{34}S$ 1.2 per mil, Crowe and Vaughan 1996) was used to standardize the

session and was analysed at the start, after every 6 spots and at the conclusion of each session, with standard analyses all within error (Table 4.6 Appendix 1). SHRIMP –SI analyses used 2 detectors with data acquired through 10 separate integrations of 10 seconds. Total error on samples was +/- 0.37 per mil for all pyrites analysed. Samples were polished and cleaned in an ultrasonic bath after the SHRIMP analyses to remove any remnant Al on the surface or in pits. All measurements are relative to Canyon Diablo Troilite (CDT).

LA –ICP-MS

Pyrite grains were then analysed at the Research School of Earth Science at the Australian National University by an Agilent 100 LA-ICP-MS system using a 20um traverse to acquire average trace element concentrations across a crystal's surface. The LA–ICP-MS operated using a 'time slice' method outlined in Longerich et al (1996a). This method enables the identification of anomalous trends that may be caused by mineral inclusions.

Pyrite crystals were ablated by a Lambda Physik Laser ablation system and traverses were selected to avoid large inclusions, however small (under 10s) spikes due to mineral inclusions were unavoidable, examples of the laser traces are observed in Figure 4.3 and Figure 4.4. This system was operated at 193nm with an energy output of 45mJ. The sample was initially transported in a H-He-Ar mixture to the Agilent Technologies 7700 series quadrupole. NIST SRM-610 and iron sulfide pellet MASS-1 were employed as standards compared to published values (Jochum et al. 2005) to ensure acceptable homogeneity for the elements analysed. Elements analysed were selected as they have been commonly studied in relation to pyrite and economic ores, they include Co, Ni, Cu, ^{77}Se, ^{82}Se, Ca, Ti, V, Mn, Zn, As, Mo, Ag, Sn, Sb, Te, W, Au, Pb, Bi and all produced results within error and limits of detection (Table 4.5 Appendix 1). Raw CPS signals were reduced using Iolite and Igor Pro (6.34A). The aim of this software

is to minimise operator errors during processing and to normalise the unknown samples to known standards.

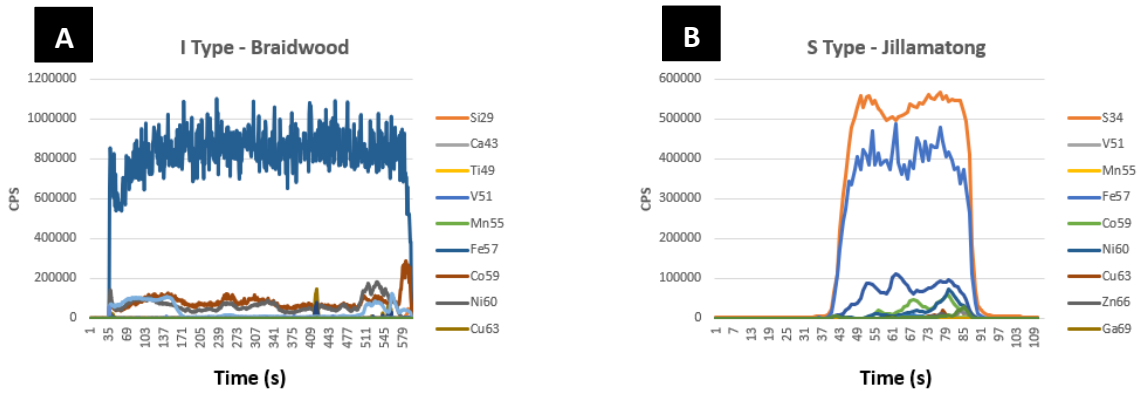

Figure 4.3 CPS laser trace examples for A) I Type Braidwood granite pyrite sample and B) S- Type Jillamatong granite pyrite sample

Trace element ratios of pyrites were calculated using the absolute element concentrations of individual pyrites and then an average determined for each pyrite stage to reflect the group. Ratios were determined through likely coupled substitution pairings and observing any trends through boxplots of the LA-ICPMS data.

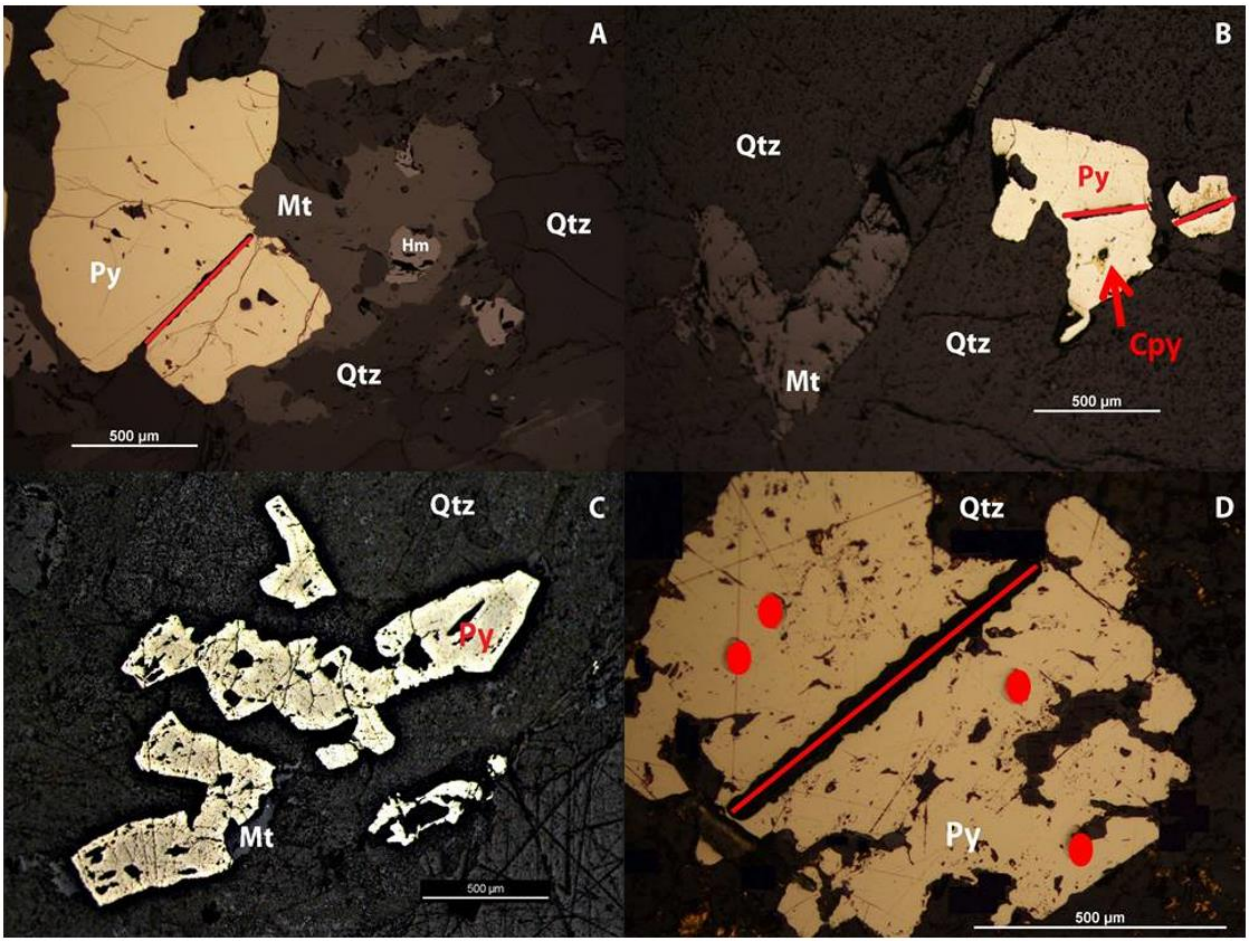

Figure 4.4: Pyrite grains, from A. Braidwood (I-type) with red line indicating laser traverse, B. Moruya (I-type) with small chalcopyrite inclusions indicated by red arrow, red line shows laser traverses, C. Mafic enclave pyrites from Braidwood (I-type), D. Dalgety (S-type) with red line showing laser traverse and red spots showing SHRIMP-SI analysis sites.

4.4 RESULTS

(A COMPLETE LIST OF RESULTS CAN BE FOUND IN APPENDIX 2)

I-Type Granites

I-type pyrites yielded a range of $\delta^{34}S$ of 0.7-2.7 per mil (Figure 4.5). Relative to S-type pyrite averages, I-type pyrites have higher median concentrations of Ni (1090 vs 633 ppm) and Co (2777 vs 176 ppm) relative to S-type pyrites (Figure 4.6). Pyrite grains contain minor Cu, As, Ag, Pb and Bi, and trace W, Sb, Sn, Mo and V (Table 4.2).

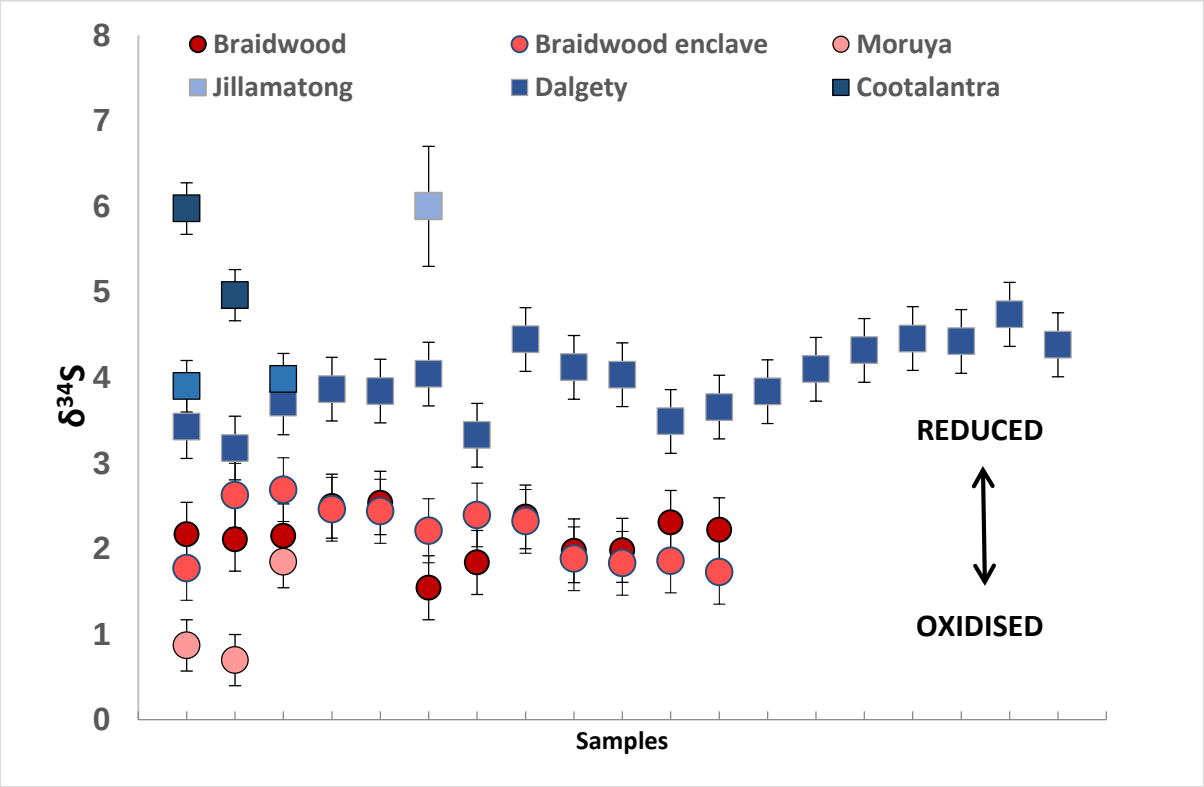

Figure 4.5: SHRIMP-SI results plotted as sample type indicator in red included to show the change in redox field. Total error displayed as error bars. Circle samples are from oxidised (I-type) granites, square samples are from reduced (S-type) granites.

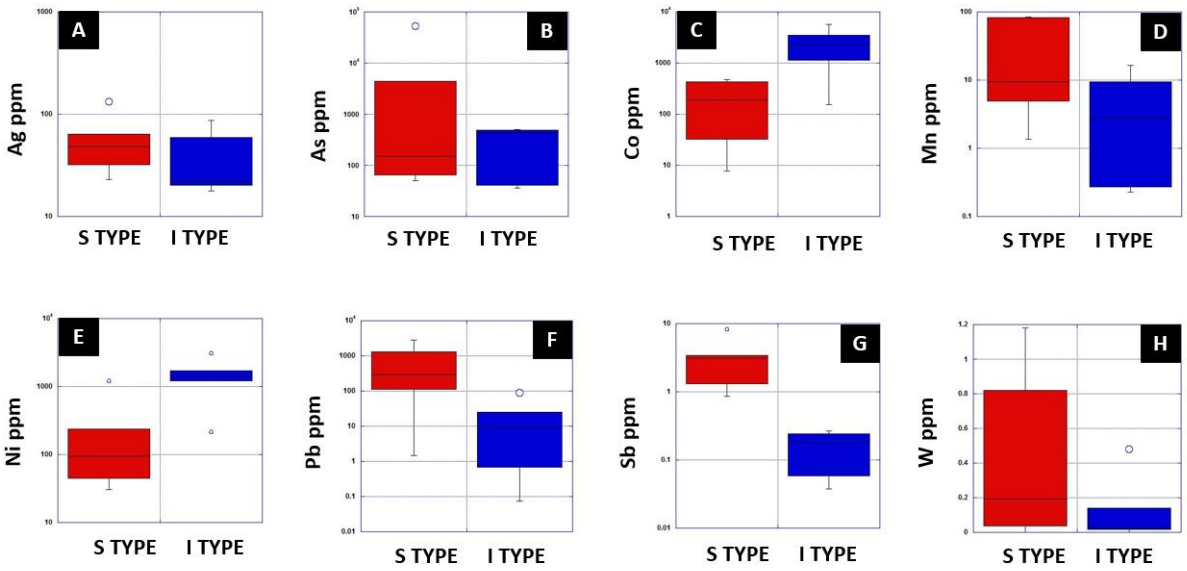

Figure 4.6 A) LA-ICPMS Ag ppm boxplot for S and I - Type granites B) As ppm C) Co ppm D) Mn ppm E) Ni ppm F) Pb ppm G) Sb ppm H) W ppm

Table 4.2: Trace element and sulfur isotopic comparison of S- vs I-type pyrites.

	S Type	I Type
δS^{34} range	1.8-6 per mil	0.7-2.7 per mil
Higher concentrations	Sb, Zn, As, Au, Sn, Pb, Bi	Co, Ni
Similar concentrations	Se, Mo, Ag, Te, W, V, Mn, Cu	

Pyrites from mafic enclaves in I- type granites can be distinguished by their lower median Ni (456 vs. 1513 ppm) and Te (0.3 vs. 4 ppm) than I-type granite pyrites. Enclave pyrites also contain higher median V (8 vs. 0.9 ppm), Mn (80vs. 3 ppm), Bi (11 vs.7 ppm), Mo (2 vs. 0.4 ppm) and As (665 vs. 322 ppm) than I-type pyrites. Sulfur isotopes are indistinguishable between I-type granite and mafic enclave pyrites (Figure 4.5).

S-Type Granites

S-type pyrite sulfur isotopes yielded a range of $\delta^{34}S$ from 1.8 to 6 per mil (Figure 4.5). S-type pyrites have higher median concentrations of Zn (14 vs. 9 ppm) Mn (53 vs. 35 ppm), Sn (3 vs. 0.15 ppm), Sb (4 vs. 0.18 ppm), Pb (185 vs. 19 ppm), Au (1 vs. 0.03 ppm), and Bi (63 vs. 9 ppm) relative to I-types (Figure 4.6, Table 4.7 and Table 4.8 Appendix 2).

4.5 DISCUSSION

Comparison of elemental ratios

Minor and trace element ratios distinguish pyrites from I- vs S-type granites, but given the heterogeneity of trace elements in pyrite, a combination of ratios best discriminates pyrites from different populations. Pb/W and As/Ni (Figure 4.7 and Table 4.10 Appendix 3) categorize most samples into granite types, but because these ratios partially overlap, plotting a ratio against a third redox sensitive element further separates granite types. As/Ni vs Sb clearly distinguish the two populations (Figure 4.6 and Figure 4.7).

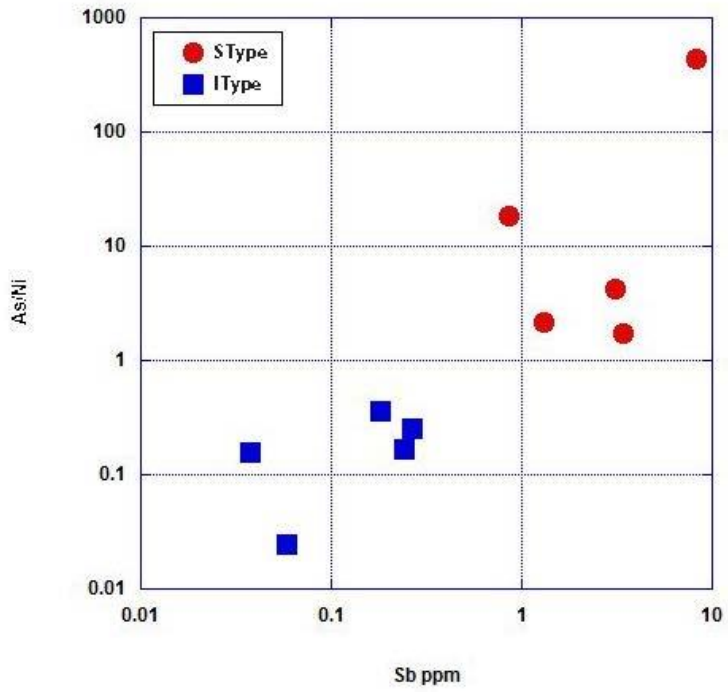

Figure 4.7: As/Ni vs Sb ppm for S-type and I-type pyrites

I-type pyrites have higher concentrations of Co and Ni than S-type pyrites; however, relative differences between pyrite groups are only observed via Co/Ni, where Co/Ni is higher in S-type than in I-type pyrites (Table 4.10 and Appendix 3). I-type pyrites contain less Sb and As compared to S-types (Table 4.7 and Table 4.8 Appendix 2). I-type samples contain lower Au, while the highest Au concentrations are found in reduced granites (average 0.9 ppm) and the highest individual Au concentration was found in the most reduced granite sampled, Jillamatong (1.2 ppm).

Sulfur isotopic trends

Chappell and White (1992) found that bulk $\delta^{18}O$ distinguished granite types, in that S-type granites are enriched in heavy oxygen relative to I-type granites. To our knowledge, no significant study of LFB $\delta^{34}S$ has been completed (Chappell and White, 1992). Sasaki & Ishihara (1979) used redox to distinguish magnetite series with bulk sulfur isotopes between 1 and 9 ‰ from ilmenite series with sulfur between -11 and -1 ‰ (Sasaki and Ishihara, 1979). The isotopic trends in the present study also found that reduced granites contain higher $\delta^{34}S$ than oxidized granites (Table 4.3). We suggest that granites are best divided at the Ni-NiO buffer rather than the magnetite-hematite (MH) buffer of Sasaki and Ishihara (1979). LFB pyrites are clearly delineated by sulfur isotopes: S-type pyrite have $\delta^{34}S > 3‰$ and I-type pyrite $\delta^{34}S < 3‰$, which is consistent with S-type granites involving heavy sulfur-rich sediments which reduce the magma (Sasaki and Ishihara, 1979; Ishihara and Sasaki, 1973; Chappell, 1974). Sasaki and Ishihara (1979) also determined that the mafic gabbros contained $\delta^{34}S$ between -1 and 3 ‰, in agreement with the present study.

Sulfur isotope fractionation is governed by temperature, pH and reduction-oxidation (Rye and Ohmoto, 1974). In magmas we can assume gradual cooling and negligible 'pH' change, leaving redox as the driver of sulfur fractionation (Rye and Ohmoto, 1974). The use of redox sensitive trace elements in pyrite to distinguish granite types may indicate oxygen fugacity measurement on a small scale. Burnham and Berry (2017) and Trail et al. (2015) used Ce/Ce* from LFB granites to discriminate S-type from I-type zircons based on oxygen fugacity. When these Ce/Ce* are plotted against sulfur isotopes from the same samples, the link between redox and sulfur isotopes becomes clear (Table 4.3 and Figure 4.8). The same trend is seen

when bulk Fe^{2+}/Fe^{3+} (Chappell database) is plotted against $\delta^{34}S$ of pyrites (Table 4.3 and Figure 4.9).

Table 4.3: Zircon (chondrite normalised) trace element data from Burnham and Berry (2017) and Trail et al. (2015), average SHRIMP sulfur isotopes(this study) and whole-rock Fe^{2+}/Fe^{3+} from the Chappell database and Trail et al. (2015).

	Cootralantra	Kyeamba	Dalgety	Braidwood Enclave	Braidwood	Moruya	Jillamatong
Type	S	S	S	I	I	I	S
Fe^{2+}/Fe^{3+}	2.4	4.0	3.3	1.5	1.5	1.9	5.9
δ34S	5.5	3.2	4	2.1	2.2	1.1	6
Ce/Ce*	45	no data	23.8	143.8	143.8	no data	23.59

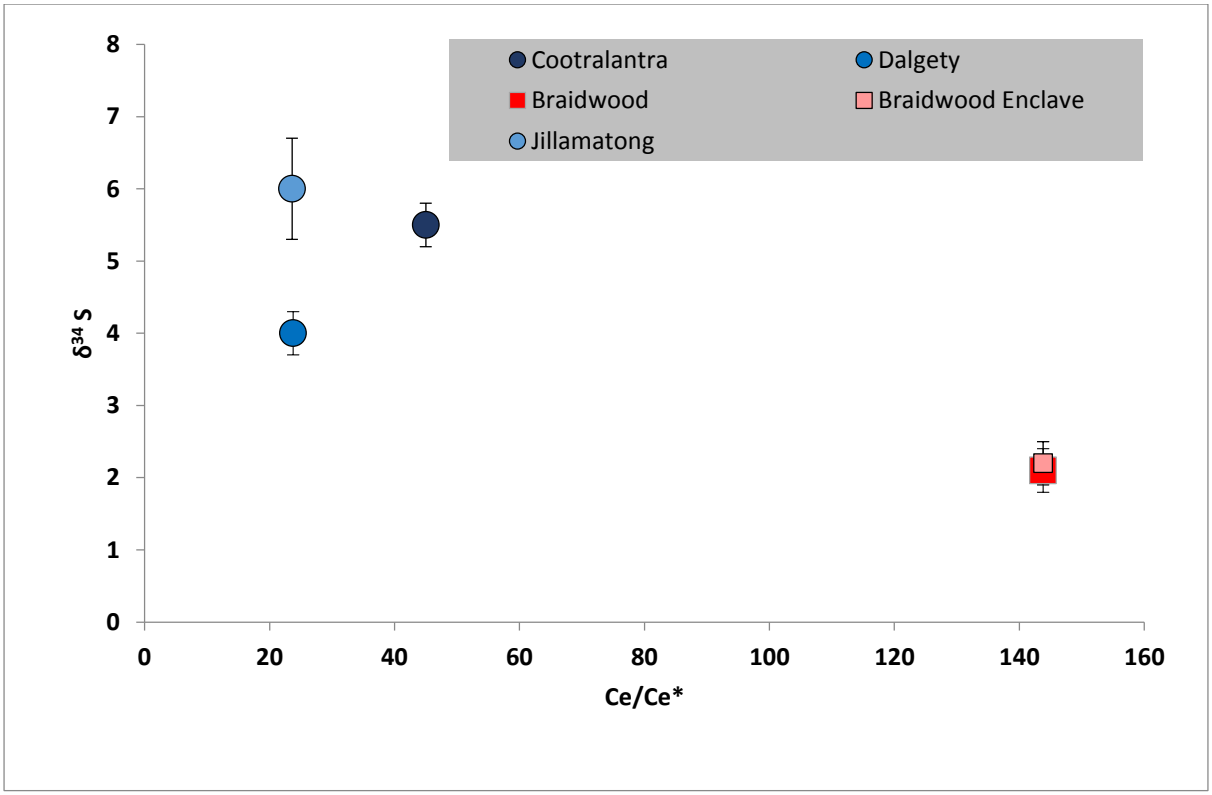

Figure 4.8: Zircon Ce/Ce* vs pyrite $\delta^{34}S$. Reduced and oxidised granites, S-type granites denoted by circle symbols and square symbols are I-type granites. Granites with high Ce/Ce* contain pyrites with low $\delta^{34}S$. Zircon Ce/Ce* from Burnham and Berry (2017) and Trail et al. (2015)

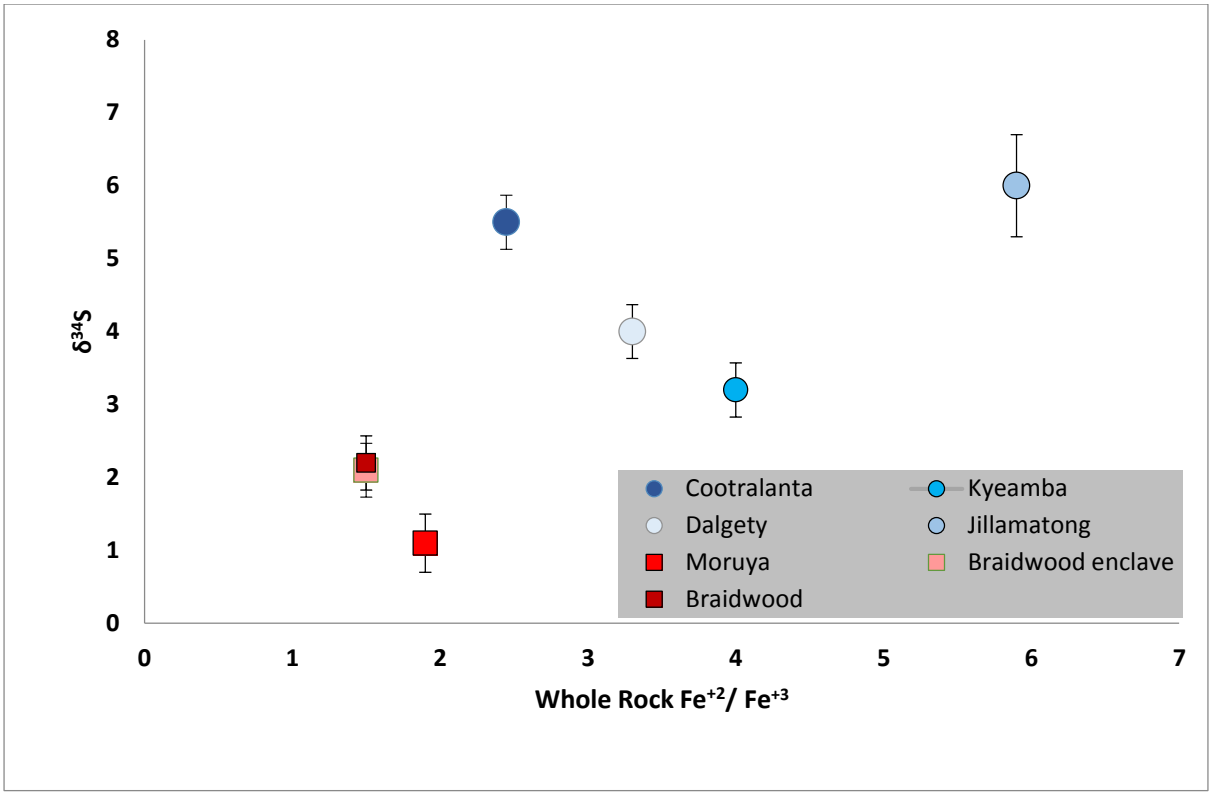

Figure 4.9: $\delta^{34}S$ of pyrites versus whole rock Fe^{2+}/Fe^{3+}. Circle samples are from reduced (S-type) granites and square samples are from oxidised (I-type) granites. $Fe^{2+}/Fe^{3+}$from the Chappell database and Trail et al. (2015).

Trace element trends in granites

Bulk geochemical approaches produced significant overlap between I- and S-type granite compositions. For this study, in a manner similar to Park et al. (2013), co-existing Fe-Ti-O and Fe-S phases discriminate I- from S- type (Ishihara et al., 1979; Park et al., 2013).

Generally, higher Pb/W is found in S-type-pyrites relative to I-type due to higher average Pb concentrations in S-type pyrite (604 vs 19 respectively). While sulfur isotopes discriminate granite types, when combined with trace elements the distinction becomes even clearer. Similar concentrations of W are identified in pyrites of both type, although higher Sn concentrations (Table 4.2) in S-type pyrites fit the associations of S-types and Sn-porphyries set out by Blevin and Chappell (1995). Arsenic is lower in I -type pyrites than in S-types, likely

due to redox controlled partitioning (Table 4.2). This is similar to the Wallaby gold deposit (Western Australia) where As and Sb are concentrated into pyrite under reducing conditions (Ward et al., 2017) Conversely, Mn concentrations in pyrite are similar in both granite types. It is likely that many of the 'redox sensitive' elements are able to effectively differentiate granite types, due to inherent atomic radius controls. It follows that while availability of an element is vital, oxidation state controls the type of associated ore system.

Mafic Enclaves

Trace elements are able to be used to distinguish pyrites in host rock from pyrite in enclaves in a manner similar to zircon (Belousova et al., 2002; Villaros et al., 2009). Enclave pyrite contains an order of magnitude higher V, Mn, Mo and Bi than host granite pyrites, with lower Ni, Zn and Te. This may be a measure of assimilation as no associated change in sulfur isotopes is seen. Note that the majority of these elements are economically significant. These consistent trace element trends are not seen in bulk analyses, because of dilution by other minerals, such that only in situ sulfide analyses can properly track chalcophile elements in granitic systems.

Cu-Mo versus Sn-W bearing granites

Whalen and Chappell (1988) grouped S- and I-type granites based on Fe^{+2}/Fe^{+3}, and modal abundances of opaque minerals (titanite, ilmentite, magnetite), with some overlap between the two groups. They attributed the association of S-type granites and Sn deposits to source rock chemistry and fractionation (Whalen and Chappell, 1988). Blevin et al. (1996) used redox to explain this link. Sulfur isotopes support the proposal of Blevin et al. (1996) and Whalen and Chappell (1988) that Sn^{+4} in oxidized magmas substitutes into Ti^{+4} sites in opaque minerals, such that high Sn concentrations are only seen in reduced hydrothermal systems.

As found by Chappell and White (1974) in whole rock studies, this study found similar W concentrations in both I-type and S-type pyrites. Consistent with Blevin and Chappell (1992), W is observed to be incompatible in oxidised and reduced granite types undergoing fractionation. W is demonstrated as having a weaker redox driver than Mo (Candela and Bouton, 1990) and as such can be used as a normalising element. I-type pyrites have an average Sn/W of 0.5 while S-type pyrites have an average Sn/W of 72. This is an excellent sensor of redox that is seen more clearly in pyrite analyses than in whole rock chemistry.

Trends observed in the reduced S-type Hatapang granite suite (Sumatra) pyrites are similar to those identified here. These granites, associated with Sn-W deposits, contain pyrites rich in Pb, As, Zn and Bi (Clarke and Beddoe-Stephens, 1987). On the other hand, Mo is observed to exolve late during crystallisation and the Hongshan Cu-Mo-(W) deposit (China; (Wang et al., 2014; Yang et al., 2017) is associated with I-type granites that contain pyrites rich in Mo, Ag and Co. Thus, monitoring these key chalcophile elements in pyrite provide an appropriate method to distinguish oxidised from reduced pathways.

Chappell and White (1974, 2001) established the link between Cu-Mo porphyries and I-type granites, and we have found this same relationship in granite pyrites. This allows assessment of granite fertility for associated economic concentrations of Cu and Mo. S-type pyrites have on average a higher Cu/Mo (189) compared to I-type (33). This suggests, regardless of concentration that I-type Cu and Mo are closer to unity relative to reduced systems. This difference relies on the concentration of Mo in pyrite during fractionation, as Mo prefers pyrite under oxidising conditions (Candela and Holland, 1984). This is consistent with oxidised systems forming Cu-Mo deposits (Frikken et al., 2005; Rowins, 2000).

Au porphyry deposits are often linked to oxidised granite suites (Blevin, 2004). Particular examples include the shoshonitic deposits contained within Ordovician igneous units of the LFB. These Cu-Au deposits are highly oxidised. Given that the present study found trace gold in higher concentrations in S-type (0.9 ppm) than in I-type granites (0.03), it may be the case that bisulfide complexed (reduced) gold partitions into pyrite while chloride complexed (oxidised) gold ends up in hydrothermal fluids. This may explain the Braidwood (I-type) pyrites containing low average Au (0.3ppm) content despite its association with Major's Creek gold deposit (Wake and Taylor, 1988).

4.6 CONCLUSION

We have shown that sulfur isotopes of paragenetically late pyrites independently sense redox, and discriminate S- from I-type granites. We have also shown that redox sensitive trace elements in pyrite reflect this. When combined, sulfur isotopes and trace elements of pyrite show remarkable trends, as follows:

- S-type pyrites, precipitated under reducing conditions, contain high concentrations of As, Sn, Bi, Zn and Au. These pyrites also tend to contain micro-inclusions of Ca-Ti silicates.
- I-type pyrites, precipitated under oxidizing conditions, are concentrated in Co and Ni and have the lowest gold concentrations despite their association with hydrothermal gold deposits.

Overall, absolute trace element concentrations are higher in pyrite formed under reducing conditions than those that formed under oxidising conditions. The As-Au affinity observed in economic gold deposits is also seen in S-type granites. This suggests a universal control on partitioning of elements of economic interest in sulfides. We also suggest that despite the

gamut of trace elements available within melts or fluids, semi-transition metals most obviously substitute for Fe or S in the pyrite structure. Since redox controls oxidation states and therefore size of available anions and cations, the idea of an over-arching redox control on ore deposition is plausible for both magmatic and hydrothermal deposits, and explains why Sn deposits are associated with reduced granites while Cu deposits are associated with oxidised granites.

APPENDIX 1 – LOCATION and DATA COLLECTION STATISTICS

Table 4.4: All samples and analyses used in this study

Collection #		Sample Name	LA-ICP-MS	SHRIMP
W058	S	Cootralantra granodiorite	58-1.d	No Spot
			No Traverse	58_2
			58-3.d	*58_3*
W139	S	Kyeamba Monzogranite	139-1.d	*139-1*
				139-2
				139-3
W063	S	Dalgety granodiorite	DYTA-1.d	*DYTA_1.1*
				DYTA_1.2
				DYTA_1.3
			DYTA-2.d	*DYTA_2.1*
				DYTA2_2
				DYTA2.3
				DYTA2_4
				DYTA2_5
				DYTA3_1
				DYTA3_2
				DYTA3_3
				DYTa_4

			DYTB-1.d	*DYTB_1* *DYTB_2* *DYTB_3* *DYTB_4* DYT_B_5 DYT_B_6 DYT_B_7
W118	**I**	**Braidwood Granodiorite**	BDW_1.d BDW_2.d	*BDW_1* *BDW_2* *BDW_3* *BDW_4* *BDW_5* *BDW_6* *BDW_7* BDW_8 BDW_9 BDW_10 BDW_11 BDW_12
W118	**I**	**Braidwood Granodiorite** **Mafic enclave**	BDWM_1a.d BDWM_2.d BDWM_3.d	BDW_m_7 BDW_m_8 *BDW_m_3* *BDW_m_6*

			BDWM_4.d	***BDW_m_5*** ***BDW_m_4*** **BDW_m_13** ***BDW_m_14*** **BDW_m_15** **BDW_m_16** **BDW_m_17** **BDW_m_18**
W120	**I**	**Moruya Tonalite**	**120a_1.d** **120a_2.d** **120B-1.d** **120B-2.d**	***120A_1*** ***120A_2*** ***120A_3***
KB32	**S**	**Jillamatong Granite**	**No Traverse** **JILL_2.d**	**JILL** **No Spot**
KB32	**S**	**Jillamatong Granite**	**JILL_1.d** **JILL_1b.d**	**No Spot** **No Spot**

Table 4.5: Statistics of analyses relative to GEOREM standards and the recorded Limits of Detection (LOD)

	NIST610			MASS 1		
	Average	σ	2σ	Average	σ	2σ
Si	329400.00	7014.75	14029.49	755.50	70.91	141.82
Ca	82825.00	1746.19	3492.37	69.50	22.90	45.80
Ti	436.45	10.23	20.47	15.67	4.65	9.29
V	445.23	8.81	17.62	72.66	5.84	11.68
Mn	488.30	10.18	20.37	324.95	24.51	49.01
Co	407.05	8.56	17.12	82.54	6.24	12.47
Ni	461.55	9.62	19.25	134.48	10.47	20.94
Cu	432.83	9.32	18.63	159675.00	10312.25	20624.50
Zn	460.38	10.26	20.52	265950.00	21411.91	42823.83
As	319.78	7.56	15.12	72.37	5.57	11.13
Se	110.25	4.06	8.13	57.18	2.67	5.34
Mo	412.35	9.19	18.38	65.55	5.12	10.23
Ag	240.20	6.36	12.71	69.53	5.35	10.70
Sn	398.75	9.63	19.26	65.41	4.82	9.65
Sb	371.70	9.71	19.41	67.81	5.34	10.69
Te	323.20	9.56	19.13	23.27	1.29	2.58
W	448.55	10.13	20.25	22.11	1.84	3.68
Au	23.24	0.59	1.17	56.13	4.21	8.43
Pb	428.85	10.66	21.31	80.48	4.84	9.68
Bi	361.48	9.65	19.30	68.95	4.17	8.34

LOD (ppm)	
Si	131.44
Ca	34.23
Ti	0.80
V	0.03
Mn	0.21
Co	0.21
Ni	0.13
Cu	0.11
Zn	0.14
As	0.25
Se	1.47
Mo	0.03
Ag	0.03
Sn	0.14
Sb	0.04
Te	0.24
W	0.02
Au	0.00
Pb	0.03
Bi	0.01

Table 4.6: Statistics of SHRIMP –SI analyses relative to Ruttan standard

	Title	34S/32S	95%T_err	ratio_per mil	wStdErr_ 95%T_per mil	Total Error
RUTTAN	*Rut-1*	0.04	1.91E-06	1.14	0.04	0.37
	Rut-2	0.04	1.91E-06	1.34	0.04	0.37
	RUTTAN_1	0.04	2.27E-06	1.17	0.05	0.37
	RUTTAN_1	0.04	2.14E-06	1.05	0.05	0.37
	RUTTAN_1	0.04	2.44E-06	1.21	0.06	0.37
	RUTTAN_1	0.04	2.19E-06	0.97	0.05	0.37
	RUTTAN_1	0.04	2.01E-06	0.90	0.05	0.37
	RUTTAN_1	0.04	2.41E-06	1.40	0.05	0.37
	RUTTAN_1	0.04	1.81E-06	1.21	0.04	0.37
	RUTTAN_1	0.04	2.04E-06	1.17	0.05	0.37
	RUTTAN_1	0.04	1.96E-06	1.14	0.04	0.37
	RUTTAN_1	0.04	1.91E-06	0.95	0.04	0.37
	RUTTAN_2	0.04	1.94E-06	1.45	0.04	0.37
	RUTTAN_2	0.04	2.06E-06	1.25	0.05	0.37
	RUTTAN_2	0.04	2.37E-06	0.95	0.05	0.37
	Ruttan_3	0.04	2.11E-06	1.55	0.05	0.37
	Ruttan_5	0.04	1.91E-06	1.43	0.04	0.37
	Ruttan_6	0.04	2.18E-06	1.49	0.05	0.37
	Ruttan_7	0.04	2.25E-06	1.05	0.05	0.37
	Ruttan_8	0.04	1.83E-06	1.19	0.04	0.37
	RUTTAN_8	0.04	2.16E-06	1.30	0.05	0.37
	RUTTAN_9	0.04	1.71E-06	1.08	0.04	0.37

APPENDIX 2 – PROCESSED DATA

Table 4.7: All I-type trace element data collected using LA-ICP MS

	I TYPE											
	120a_1.d	120a_2.d	BDWM_1	BDWM_2.	BDWM_3.	BDWM_4.	BDW_1.d	BDW_2.d	120B-1.d	120B-2.d	Average	σ
Si	61000.00	8600.00	14700.00	1560.00	2500.00	1690.00	482.00	162.90	255.00	5260.00	9620.99	18633.74
Ca	346.00	780.00	4090.00	207.00	440.00	580.00	82.00	27.50	74.00	2040.00	866.65	1277.71
Ti	42.00	46.00	159.00	32.64	30.90	28.14	21.14	18.77	15.16	18.60	41.24	42.62
V	0.20	0.23	28.90	1.09	2.24	0.16	0.41	0.07	0.05	4.20	3.75	8.93
Mn	9.40	2.11	289.00	3.32	25.70	0.83	3.56	0.23	0.27	16.40	35.08	89.60
Co	2180.00	3490.00	4520.00	4460.00	314.00	3380.00	155.00	1128.00	2493.00	5650.00	2777.00	1858.74
Ni	1480.00	1358.00	524.00	179.00	194.00	930.00	3100.00	1218.00	1709.00	217.00	1090.90	907.03
Cu	9.00	46.40	28.80	6.20	14.50	1.19	170.00	11.80	2.09	7.83	29.78	51.15
Zn	2.35	72.00	29.50	1.10	2.45	0.37	7.00	1.16	0.43	0.94	11.73	22.96
As	375.00	482.00	1180.00	779.00	133.00	568.00	491.00	508.00	41.40	36.10	459.35	350.34
Se	43.00	49.00	21.30	15.07	8.35	35.10	32.36	22.17	52.20	62.10	34.07	17.47
Mo	0.96	1.03	3.50	0.62	2.44	0.01	0.32	0.01	0.05	0.06	0.90	1.18
Ag	59.60	87.00	31.80	43.00	29.40	20.00	17.70	20.10	22.20	21.20	35.20	22.40
Sn	0.09	0.46	0.25	0.06	0.07	0.04	0.08	0.06	0.09	0.31	0.15	0.14
Sb	0.27	0.18	0.55	0.09	0.09	0.09	0.04	b.l.d	0.06	0.24	0.18	0.16
Te	4.34	6.25	0.34	0.10	0.13	0.48	0.32	b.l.d	0.34	9.01	2.37	3.24
W	0.14	0.48	0.96	0.23	0.30	b.l.d	0.03	b.l.d	0.02	0.02	0.27	0.31
Au	0.03	0.01	0.01	b.l.d	0.02	b.l.d	0.01	b.l.d	0.07	0.09	0.03	0.03
Pb	90.00	24.80	37.00	5.30	9.20	3.85	1.88	0.08	0.67	16.70	18.95	27.70
Bi	9.50	4.95	24.80	2.99	7.20	10.40	1.53	0.12	0.11	27.30	8.89	9.75

Table 4.8: S-type trace element data collected using LA-ICP MS

	S TYPE										
	JILL_1.d	JILL_1.d	JILL_2.d	58-1.d	58-3.d	DYTB-1.d	DYTA-1.d	DYTA-2.d	139-1.d	Average	σ
Si	n.s	n.s	n.s	63900.00	1570.00	282.00	6680.00	9500.00	312.00	13707.33	24873.19
Ca	n.s	n.s	n.s	55.00	33.00	5300.00	740.00	2070.00	46.00	1374.00	2078.53
Ti	n.s	n.s	n.s	39.40	19.16	16.83	820.00	1020.00	14.24	321.61	467.89
V	0.25	0.12	1.83	0.51	0.07	0.06	15.30	19.90	0.04	4.23	7.69
Mn	154.00	117.00	18.60	7.00	11.80	1.36	82.00	83.90	4.90	53.40	57.08
Co	112.00	20.10	135.00	430.00	32.40	471.00	213.00	169.00	7.69	176.69	170.29
Ni	2350.00	1190.00	450.00	122.00	236.00	66.70	44.60	30.20	1208.00	633.06	796.20
Cu	70.00	5.20	127.00	107.00	250.00	12.80	15.60	8.60	12.40	67.62	82.53
Zn	5.20	9.40	44.00	3.42	2160.00	5.37	20.50	24.20	0.66	252.53	715.43
As	76.00	1.86	189.00	53000.00	4400.00	113.30	189.00	64.80	50.50	6453.83	17512.82
Se	23.10	23.00	43.30	15.60	193.00	8.02	6.47	9.13	22.67	38.25	59.12
Mo	n.s	n.s	n.s	1.56	0.02	0.25	0.07	0.15	0.09	0.36	0.59
Ag	6.90	7.04	13.60	132.00	63.80	50.50	31.90	45.60	23.10	41.60	39.34
Sn	3.30	3.56	6.70	2.56	289.00	0.14	3.36	4.63	0.06	34.81	95.34
Sb	7.90	1.52	67.00	8.20	0.86	3.44	3.08	1.30	b.l.d	11.66	22.54
Te	b.l.d	0.18	0.32	1.90	0.34	1.24	4.36	0.46	2.51	1.41	1.46
W	n.s	n.s	n.s	0.34	0.05	0.04	0.82	1.18	b.l.d	0.49	0.49
Au	0.05	1.24	5.30	1.11	0.41	0.02	0.01	0.01	b.l.d	0.91	1.72
Pb	168.00	5.92	426.00	2820.00	151.00	1320.00	430.00	114.40	1.48	604.09	924.73
Bi	5.10	0.10	8.00	285.00	229.00	19.90	16.80	10.81	0.95	63.96	110.53

Table 4.9: All S and I-type sulfur isotope data collected using SHRIMP-SI

	Title	34S/32S	95%T_err	ratio_per mil	wStdErr_95%T _permil	Total Error
I TYPE	*120A_1*	0.04	2.10E-06	0.87	0.05	0.37
	120A_2	0.04	1.66E-06	0.70	0.04	0.37
	120A_3	0.04	2.56E-06	1.84	0.06	0.37
	BDW_1	0.04	2.21E-06	2.17	0.05	0.37
	BDW_10	0.04	1.53E-06	2.11	0.03	0.37
	BDW_11	0.04	2.30E-06	2.15	0.05	0.37
	BDW_12	0.04	2.51E-06	2.50	0.06	0.37
	BDW_2	0.04	2.06E-06	2.53	0.05	0.37
	BDW_3	0.04	1.98E-06	1.54	0.05	0.37
	BDW_4	0.04	2.08E-06	1.84	0.05	0.37
	BDW_5	0.04	1.95E-06	2.37	0.04	0.37
	BDW_6	0.04	1.90E-06	1.97	0.04	0.37
	BDW_7	0.04	1.81E-06	1.98	0.04	0.37
	BDW_8	0.04	1.98E-06	2.31	0.05	0.37
	BDW_9	0.04	1.81E-06	2.22	0.04	0.37
	BDW_m_13	0.04	1.79E-06	1.77	0.04	0.37
	BDW_m_14	0.04	2.39E-06	2.62	0.05	0.37
	BDW_m_15	0.04	2.32E-06	2.69	0.05	0.37
	BDW_m_16	0.04	1.86E-06	2.46	0.04	0.37
	BDW_m_17	0.04	1.95E-06	2.44	0.04	0.37
	BDW_m_18	0.04	2.21E-06	2.21	0.05	0.37
	BDW_m_3	0.04	2.37E-06	2.39	0.05	0.37
	BDW_m_4	0.04	1.71E-06	2.32	0.04	0.37
	BDW_m_5	0.04	2.09E-06	1.88	0.05	0.37
	BDW_m_6	0.04	2.41E-06	1.83	0.05	0.37
	BDW_m_7	0.04	2.35E-06	1.86	0.05	0.37
	BDW_m_8	0.04	2.01E-06	1.73	0.05	0.37

S TYPE	*139-1*	0.04	1.84E-06	3.90	0.04	0.37
	139-3	0.04	2.05E-06	3.98	0.05	0.37
	58_2	0.04	2.03E-06	5.97	0.05	0.37
	58_3	0.04	2.08E-06	4.96	0.05	0.37
	DYT_B_5	0.04	2.15E-06	3.43	0.05	0.37
	DYT_B_6	0.04	1.95E-06	3.17	0.04	0.37
	DYT_B_7	0.04	1.81E-06	3.70	0.04	0.37
	DYTA_1.1	0.04	1.74E-06	3.86	0.04	0.37
	DYTA_1.2	0.04	1.79E-06	3.84	0.04	0.37
	DYTA_1.3	0.04	1.90E-06	4.04	0.04	0.37
	DYTA_2.1	0.04	1.90E-06	3.33	0.04	0.37
	DYTa_4	0.04	1.84E-06	4.44	0.04	0.37
	DYTA2.3	0.04	1.85E-06	4.12	0.04	0.37
	DYTA2_2	0.04	1.70E-06	4.03	0.04	0.37
	DYTA2_4	0.04	1.59E-06	3.49	0.04	0.37
	DYTA2_5	0.04	2.04E-06	3.65	0.05	0.37
	DYTA3_1	0.04	2.00E-06	3.83	0.05	0.37
	DYTA3_2	0.04	1.99E-06	4.10	0.05	0.37
	DYTA3_3	0.04	2.09E-06	4.32	0.05	0.37
	DYTB_1	0.04	2.13E-06	4.45	0.05	0.37
	DYTB_2	0.04	1.78E-06	4.42	0.04	0.37
	DYTB_3	0.04	1.90E-06	4.74	0.04	0.37
	DYTB_4	0.04	2.30E-06	4.38	0.05	0.37
	JIL	0.60	2.13E-06	6.00	0.04	0.80

APPENDIX 3 – PROCESSED DATA

Table 4.10: Table 1 Average ratios of trace elements in S- Type and I-Type Pyrites. From average element values.

	Sn/W	Cu/Mo	As/Ni	Co/Ni	Pb/W
S TYPE	72	189	10	0.3	1494
I TYPE	0.50	33	0.4	2.50	70

5. REDOX CONTROLLED VARIATION OF AU AND AS IN SYNTHESIZED PYRITE

ABSTRACT

Pyrite precipitates over a wide range of conditions and is found in most rock types, including gold deposits where a clear link between arsenic (As) and gold (Au) is observed within pyrite (Reich and Becker, 2006; Simon et al., 1999; Ward et al., 2017). There is limited understanding of the mode or tenor of gold deposition over a range of redox conditions in the presence or absence of As (Belousov et al., 2016; Kusebauch et al., 2018; Large et al., 2016). Whether the initial oxidation state of Au impacts concentrations of gold with pyrite during transport and deposition is also unclear. This study aims to show that the oxidation state of Au, in the presence of As, can affect the mode and tenor of pyrite-bearing gold ore deposition. While reduction is widely regarded as a destabiliser of complexes in solution and creation of Au bearing pyrite ore, we assert that the oxidation state the Au delivered to site and the presence of As, controls the mode of deposition, as well as the grade and tenor of a deposit. The experiments described here provide insights into how gold deposits form, particularly porphyry deposits and may be extended to lower temperatire Carlin deposit formation.

Pyrite crystals were synthesized using Chemical Vapor Transport (CVT) over a range of buffered fO_2 conditions (fO_2= -14, -19, -24) at constant temperature (600 °C). Experiments were doped with combinations of trace elements including; arsenic (As^0), gold (Au^0) or Au^{+1} (from AuCl). Au^0 was shown to be incompatible in pyrite with the greatest concentrations occurring in pyrite formed under the most reduced conditions. This contrasts with experiments starting with Au^+, which produced an order of magnitude higher Au in pyrite but also precipitated gold inclusions under all experimental conditions, thus establishing

that Au oxidation state affects deposition style. Arsenic and Au (regardless of state) were shown to covary, although As and Au concentrations in pyrite increased systematically with reduction in experiments starting with As+Au^0, in runs starting with As +Au^+ concentrations decreased with reduction. This contrasting behaviour is controlled by the mode of Au deposition, i.e whether Au deposits as free Au or within the pyrite structure.

5.1 INTRODUCTION

Pyrite is the most common sulfide mineral in hydrothermal ore deposits (Abraitis et al., 2004; Vaughan and Corkhill, 2017) and the most important in gold deposits (Chen et al., 2014b). Anomalous As concentrations are often present within pyrite from high-yielding gold deposits, and the concentration of As in pyrite is known to affect and control the maximum solubility of Au in its structure (Reich et al., 2005; Simon et al., 1999; Zhu et al., 2011). While pyrite (FeS_2) is most commonly found in the face centered cubic (FCC) structure, sulfur as a dimer (as shown in Figure 5.1; (Chen et al., 2014b) forms different crystal structures based on formation conditions (Dubosq et al., 2019) and the availability of compatible trace elements when crystallization occurs via either magma or fluid (Craig et al., 1998; King et al., 2014; Peterson and Mavrogenes, 2014). Pyrite has been shown to act as a trap for trace elements in magmatic-hydrothermal environments (Fontboté et al., 2017).

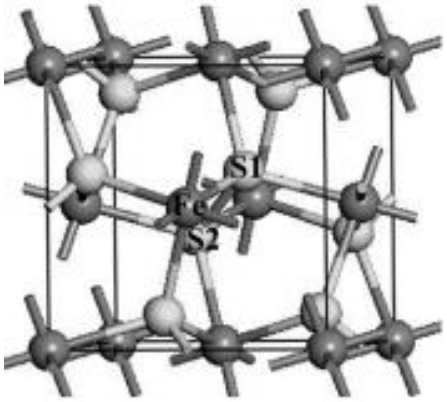

Figure 5.1: Modified after Chen et al. (2014), bulk FeS_2 unit cell (2 x 2 x 2 supercell) with S_2 dimer indicated.

In pyrite-bearing gold deposits, where a clear link exists between As and Au concentrations, As-rich pyrite grains either contain significant Au or are associated with native Au (Reich et al., 2005; Ward et al., 2017). Pyrite contains As either as nano-inclusions of minerals such as realgar or arsenopyrite or substituted into its crystal lattice. The difference between these two scenarios is not easily determined given that sub-micron inclusions often appear as substitutions.

Gold has been identified as micro inclusions in over-saturated conditions in the presence of Au - establishing a Au-As solubility curve (Reich et al., 2005), which demonstrates the significance of As in Au deposits. Yet the oxidation states of the Au and As and how these affect gold deposition remains unknown. Sulfur and chlorine are also recognised as important elements in Au transport as they are crucial ligand-formers (Zhu et al., 2011). Gold complexes, particularly when charged, enable effective adsorption of Au ligands to the surface of As-rich pyrite crystals via electrostatic attraction, i.e $Au(HS)$ and $Au(HS)^-_2$ (Widler and Seward, 2002). If ligand charge affects Au deposition then the oxidation state also must.

A study of a Carlin style gold deposit at Twin Peaks shows gold and As present in pyrite as Au^0, Au^{+1} and As^{-1} respectively (Simon et al., 1999). Micro-inclusions of gold (Au^0) were found in

pyrite in addition to Au^{+1} and As^{-1} in the pyrite structure. This provides an explanation for how gold is found in any given deposit (i.e structural or as inclusions) and provides an indication of the depositional mechanism that took place. If As aids surface adsorption of Au on pyrite via electrostatic attraction, i.e semi-conducting properties, then the coordination of the Au controls the size of the vacancy in pyrite, such that As creates vacancies favourable for Au deposition into said vacancies.

Reduction of sulfur (SO_4 (S^{4+}) to H_2S (S^{2-}) results in precipitation of sulfides in combination with one or more of the following anions; Fe^{+2}, Ni^{+2}, Co^{+2}. Thus, sulfide formation depends on cation availability and redox conditions. Metalloids, such as As and antimony precipitate due to reduction (Skirrow and Walshe, 2002; Ward et al., 2017). The common association between Au and As within pyrite suggests a clear link to Au depositional processes (Maddox et al. 1998, Reich et al. 2005). However, this association is found in pyrite under both oxidized and reduced conditions, obscuring the controlling process(es). Additionally, arsenopyrite often contains higher concentrations of Au than coexisting pyrite (Maddox et al. 1998), further complicating this link. The conditions driving the Au-As affinity in Fe-S minerals is unclear, as is the mode of deposition, whether as mineral inclusion or in substitution (Reich et al. 2005).

Thermodynamic modelling suggests that As-S bonding is energetically favourable during FeS_2 crystallization at low fO_2 (Reich and Becker, 2006). In a study of natural pyrites, Reich et al. (2005) found concentrations of As as high as 19 wt. % in pyrite at formation temperatures as low as 300 °, however these samples were not measured for redox conditions and so no direct link should be made between As content of pyrite and redox. Thus, the present study seeks to determine the maximum solubility of As in pyrite and its redox sensitivity. Direct

measurement of Au and As concentrations in pyrite formed over a series of oxygen fugacity-controlled experiments aims to clarify the As-FeS_2 and As-Au-FeS_2 relationships.

Anomalous As has been shown experimentally to correlate with Fe cation deficiencies in pyrites containing structurally bound 'invisible' Au over a range of temperatures (Fleet and Mumin, 1997a). Substitution of As^{+3} (0.58 atomic radius) for Fe^{+2} (0.61) into the crystal lattice of pyrite can modify inherent bond lengths making substitution of unusual trace element sizes (Au^{+1}) via hetero-valent substitution favourable (Deditius et al., 2008; Reich et al., 2005).

Thus, arsenian pyrite may be the key to gold deposition. Conversely, Au^{+3} adheres to arsenopyrite more readily than pyrite (Maddox et al. 1998) and arsenopyrite contains higher concentrations of Au than pyrite in many gold deposits, where Au positively correlates with As (Fleet et al., 1993). However, pyrite is generally more abundant than arsenopyrite (Abraitis et al., 2004), making arsenian-pyrite the key control on economic concentration of Au.

Gold has been reported in pyrite as free gold (Au^0) and/or within the pyrite structure as Au^+ or Au^{3+}. This study used synthesized pyrites to determine if correlations exist between As and Au concentrations in pyrite as a function of redox state. This study also sought to determine how redox controls depositional mechanisms, which in turn determine if Au ends up in pyrite or as nuggets, which will be referred to as its mode of occurrence, which is indicative of the oxidation state of the Au and whether it is coupled with As or not. The relationships established in this paper may better explain Au deposition in the Fe-S system and clarify the role played by As in such systems.

5.2 METHODOLOGY

Pyrite crystals, varying from 10-100 microns across, were precipitated using chemical vapor transport (CVT) in sealed silica tubes containing oxide buffers and dopants. Crystals were then

mounted, polished to ¼μm, imaged via reflected light microscopy, Scanning Electric Microscopy (SEM) and analysed by Laser Ablation Inductively Coupled Plasma Mass Spectroscopy (LA-ICP-MS). Co-precipitating FeO and AsS minerals were documented and used to ensure experiments occurred at the correct oxygen fugacity.

This study aimed to determine if the oxidation state of Au, in the presence of As affects the mode and tenor of gold deposition. Using a table of standard electopotentials, it is predicted that Au^{+} is far more likely to substitute into pyrite during than Au^{0} (Table 5.1). As previously mentioned, As is thought to aid in Au deposition in pyrite via electrostatic attraction, providing defects in the pyrite structure and binding with gold substituting for Fe^{+2} (Reich et al., 2005; Simon et al., 1999; Zhu et al., 2011). Due to the volatile nature of As and its many oxidation states, no appropriate half-equation exists to predict its behaviour.

Table 5.1: Electrochemical potential of pyrite reactions involving Au and the predicted volts

Equation	Volts
$Fe^{+2}_{(aq)} + S_{2(g)} \rightleftharpoons FeS_2$	0.033
$Fe^{+2}_{(aq)} + Au^{+}_{(aq)} + S_{2(g)} \rightleftharpoons Fe(Au)S_2$	1.713
$Fe^{+2}_{(aq)} + S_{2(g)} + Au_{(s)} \rightleftharpoons Fe(Au)S_2 + e^{-}$	-1.647

Crystal Synthesis

Pyrite crystals were synthesized from a mix of 99.9% FeS powder, 99.999% pure granulated sulfur, and 98+% $Fe(III)Br_3$ (Anhydrous) powder (Equation 1).

Equation 1 $FeS_{(s)} + S_{2(S)} + FeBr_{3(s)} \rightleftharpoons 2FeS_{2(s)} + Br_{2(g)}$

Dopants were added in a fixed amount to each experiment as either 99.9% pure As powder, 99.9% Au(I)Cl powder or Au^0. A full list of experiment components are shown in Appendix 1. Oxygen buffers used in the experiments include pure hematite, magnetite and ulvòspinel ($Mt_{15}Usp_{85}$ and $Mt_{90}Usp_{10,}$ both equation 2, 3 respectively and made using gas ratios in Table 5.2) and aimed to mimic fugacities shown in Figure 5.2.

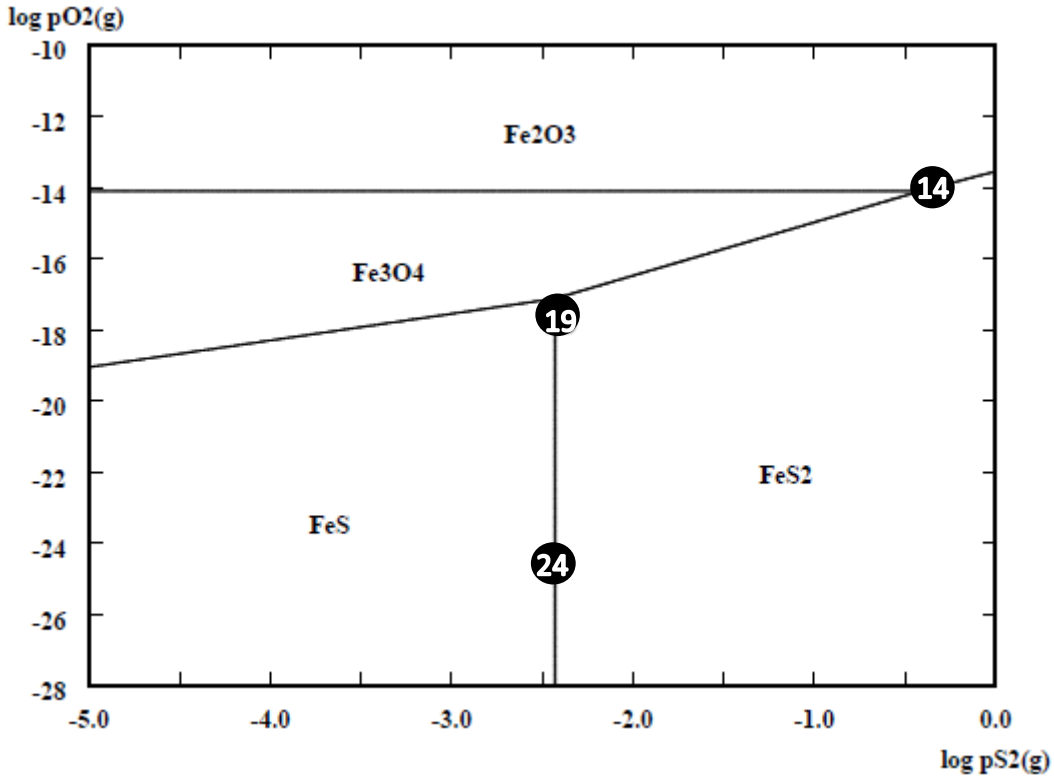

Figure 5.2: fO_2-fS_2 phase diagram of the Fe-S-O system at 600°C and 1 kbar generated using Outotec HSC chemistry software. Points represent positions of buffered experiment at the 3 oxygen fugacities studied (hm-mt-py, py-mt-po and po-py).

Buffers were synthesized in 1 atmosphere gas furnaces using carbon-dioxide and carbon-monoxide mixtures at ratios appropriate to the oxygen fugacites outlined in Buddington and Lindsley (1964) at 600 °C . Oxygen fugacity conditions of pyrite synthesis were confirmed via observation of co-existing As-S and Fe-O minerals present. This provided a check for

approximate oxygen fugacity of fO_2 =-14, -19 and -24. Excess sulfur set S fugacity at approximately fS_2= -2.

Equation 2 $Fe_2O_{3(s)} + TiO_{2(s)} \rightleftharpoons 2FeTiO_{3(s)}$

Equation 3 $2Fe_3O_{4(s)} + 3TiO_{2(s)} \rightleftharpoons 3Fe_2TiO_{4(s)} + O_{2(g)}$

Table 5.2: Gas mixes used in the 1 atmosphere furnaces to make buffers according to the methods outlined in Buddington and Lindsley (1964) and modelled using the Bioanalytical Microfluidics Program from the School of Chemical and Biological Engineering at Colorado State University.

	CO	**CO_2**
logfO_2 -19	4x10ppm	69x200ppm
logfO_2-24	100x10ppm	5x 10ppm

$FeBr_3$ was used as a halogen accelerator, forming Br_2 which was lost upon cracking of the tube (Equation 4) (Lehner et al., 2006b).

Equation 4 $FeBr3 \rightleftharpoons Fe^{2+} + Br_{2(g)}$

Chemical vapor deposition (CVD) in silica tubes (Outside Diameter 50mm and Internal Diameter 40mm) yielded fine-grained pyrite crystals (<80μm) using the apparatus in Figure 5.3. Sealed silica tubes were contained in pressurised steel vessels within a box furnace held at a constant 600°C for 48 hours and subsequently cooled over 24 hours to promote crystal growth producing measurable crystals.

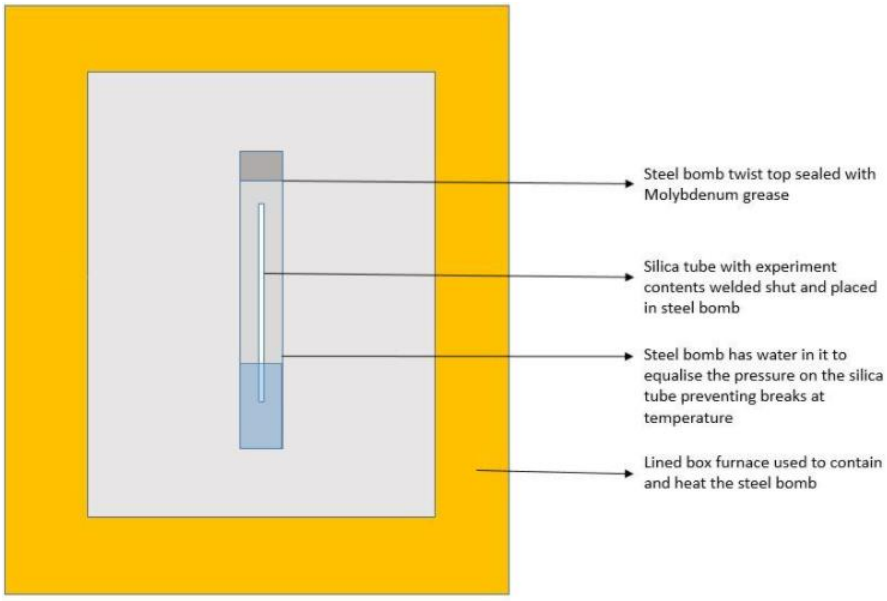

Figure 5.3: Schematic of apparatus used to grow pyrite crystals at buffered conditions

Experimental products were mounted in epoxy and polished. SEM confirmed mineral identifications and major element concentrations. Subsequent LA-ICP-MS analyses utilized an Agilent 100 at the Australian National University's Research School of Earth Sciences, analysing Fe, As and Au CPS (Longerich et al., 1996).

Laser Ablation-Inductively Coupled Plasma-Mass Spectrometry (LA-ICP-MS)

Grains larger than 30 µm were selected for LA-ICP-MS analysis. Multiple measurements of each phase were made to assess variability, a full list can be found in Appendix 1. 20 µm wide traverses were used to measure trace element concentrations in pyrite grains. Pyrites were ablated using a Lambda Physik laser ablation system at the Australian National University, operating at 193nm, with an output energy of 45mJ. The ablated sample was initially delivered to the Agilent Technologies 7700 series quadrupole via a H-He-Ar stream. Standards used during analyses were NIST SRM-612 and iron sulfide pellet MASS-1 (Appendix 2, Table 5.4). All raw counts per second were processed using Iolite and Igor Pro (6.34A). This software minimizes operator error when signal processing and normalization to known standards. The

averages attained were compared to published values (Jochum et al., 2005). Average values and standard deviations can be found in Appendix 2. Limits of detection located in Appendix 2, Table 5.5.

5.3 RESULTS

(APPENDIX 3 HAS A COMPLETE LIST OF DATA AND AVERAGED RESULTS)

Experiments doped only with As resulted in mean As concentrations increasing with reduction in a linear pattern (Figure 5.4A, Figure 5.5). Experiments doped with Au^0 resulted in mean Au concentrations in pyrite decreasing, best fitting a polynomial relationship (Figure 5.4B). Experiments doped with Au^{+1} show average most oxidised and reduced conditions to be higher than log 19 oxygen fugacity (saddle pattern), the raw data and averaged trend exhibit a polynomial fit (Figure 5.4C)). Pyrite grains doped with Au^{+1} contain an order of magnitude more gold than those starting with Au^0 (Figure 5.4).

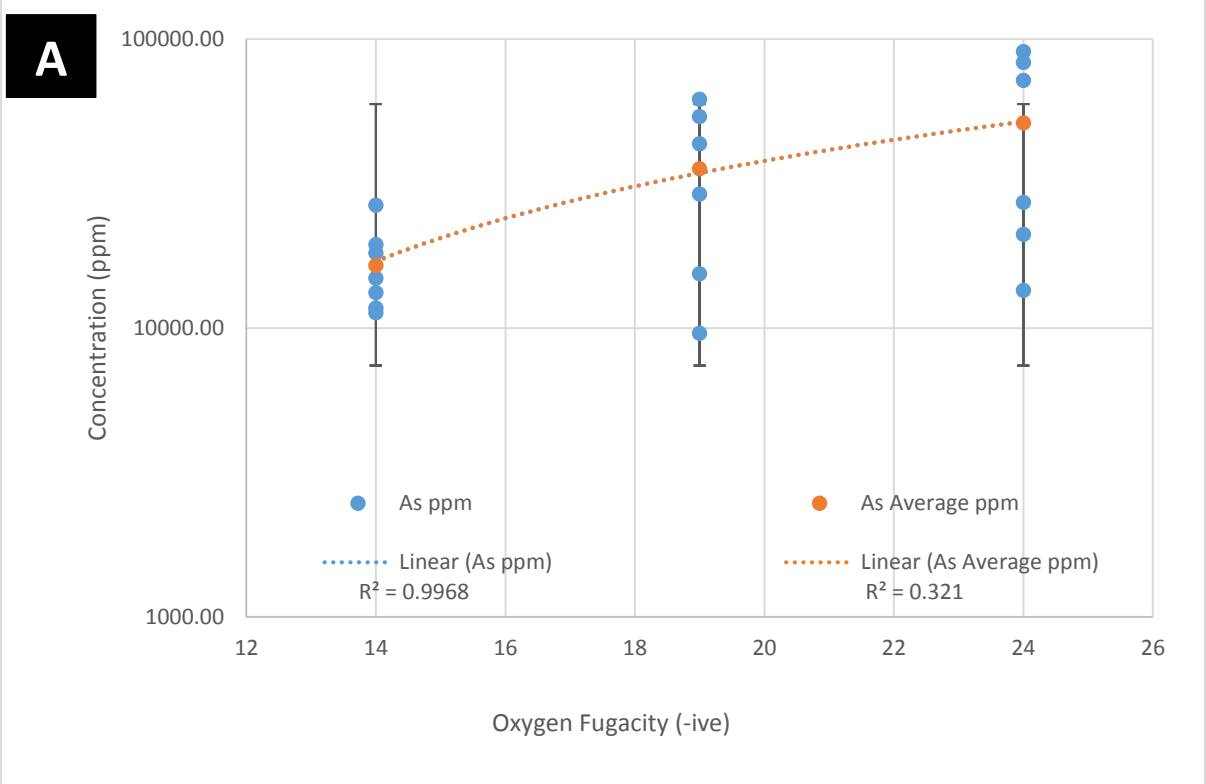
A
100000.00
10000.00
1000.00
Concentration (ppm)
As ppm
As Average ppm
Linear (As ppm)
R² = 0.9968
Linear (As Average ppm)
R² = 0.321
12
14
16
18
20
22
24
26
Oxygen Fugacity (-ive)

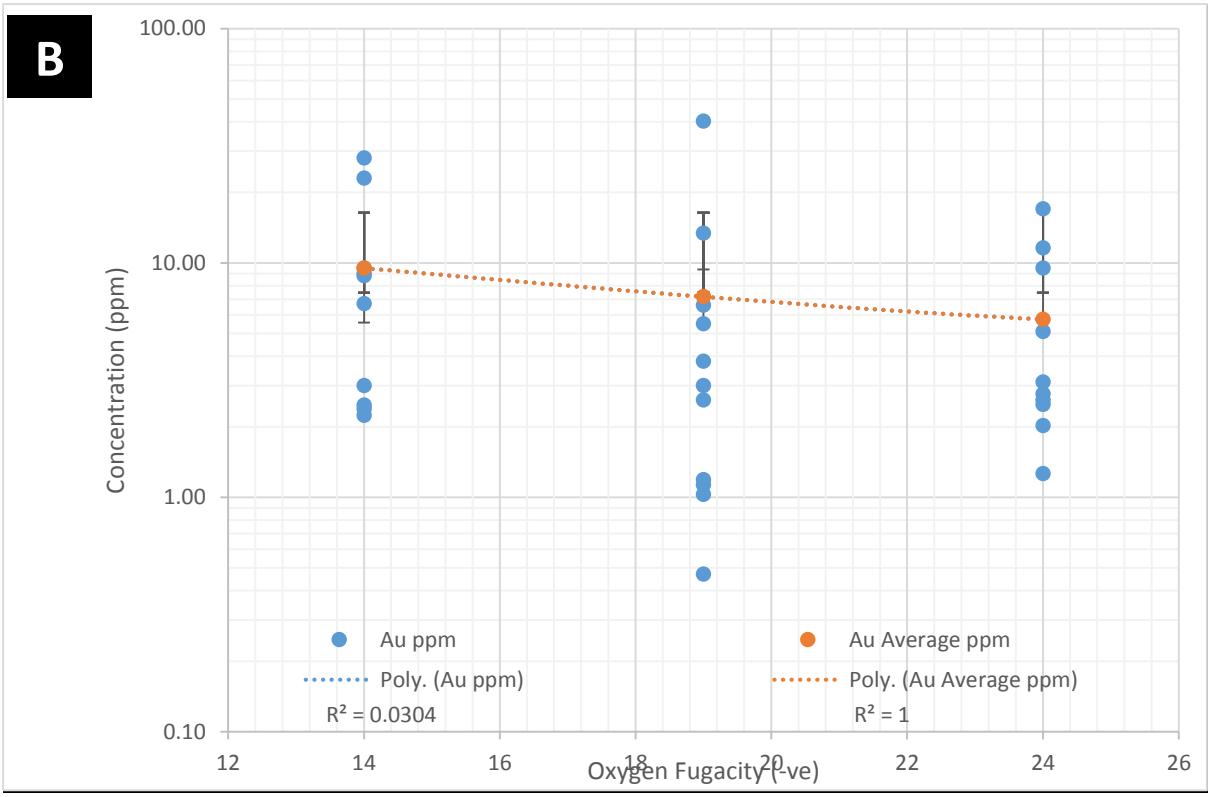
B
100.00
10.00
1.00
0.10
Concentration (ppm)
Au ppm
Au Average ppm
Poly. (Au ppm)
R² = 0.0304
Poly. (Au Average ppm)
R² = 1
12
14
16
18
20
22
24
26
Oxygen Fugacity (-ve)

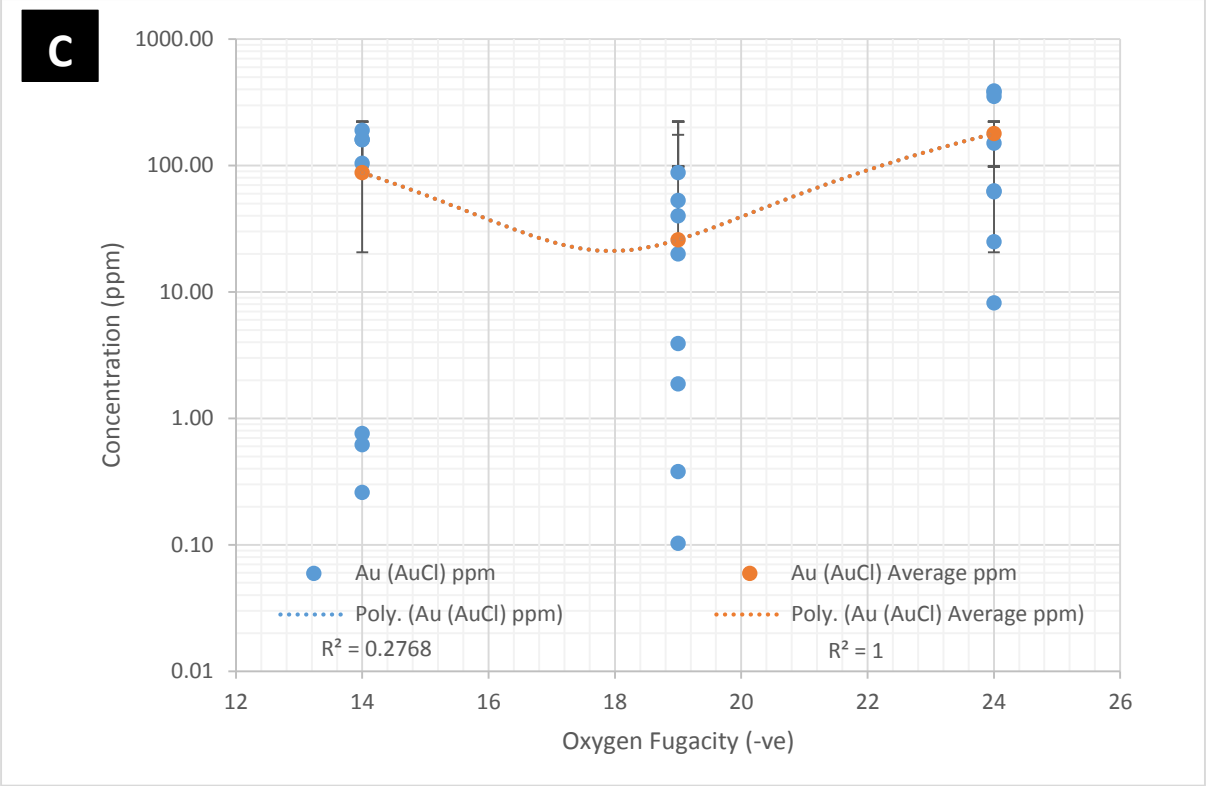

Figure 5.4: Single element experiments: A) Average concentration of As, B) Au0 and C) Au+1 in pyrite crystals from each experimental run across 3 oxygen fugacities. Error bars depict standard deviation of results.

Experiments with As and Au^0 also show both elements exhibiting highest concentrations at reduced conditions compared with the most oxidised condition (Figure 5.6 and Figure 5.7). However, As and Au^0 both display a polynomial relationship that displays a saddle between fO_2 14-19. Conversely, Au^{+1}+ As experiments show the inverse trend, with the lowest average As and Au^+ concentrations found at the most reduced oxygen fugacity (Figure 5.8 and Figure 5.9). The average values for As and Au+ are similar between fO_2 14 and 19 however, the highest average values for both are identified at fO_2 19.

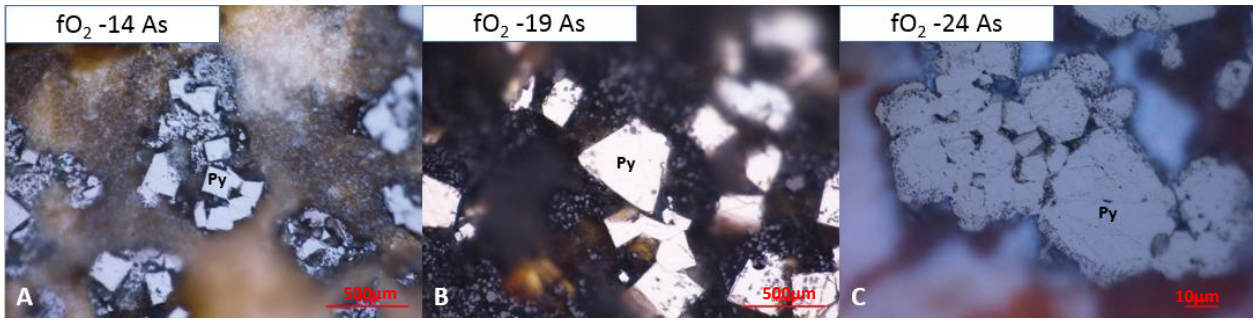

Figure 5.5: Micrographs of pyrite taken using reflected light microscope with oil A) Most oxidized pyrite doped with Arsenic B) Pyrite formed at fO_2 -19 with As C) Pyrite formed at fO_2 -24 with As.

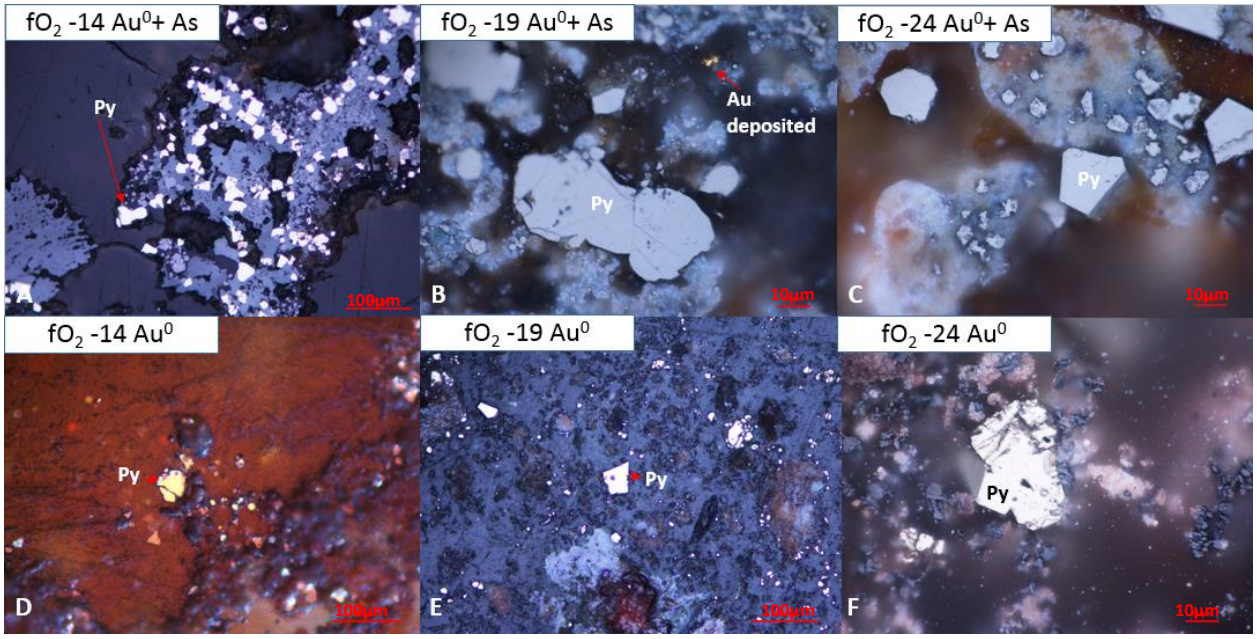

Figure 5.6: A) Pyrite grown at fO_2 -14 doped with Au^0 and As B) Pyrite grown at fO_2 -19 doped with Au^0 and As showing native gold C) Pyrite grown at fO_2 -24 doped with Au^0 and As D) Pyrite grown at fO_2 -14 doped with Au^0 E) Pyrite grown at fO_2 -19 doped with Au^0 F) Pyrite grown at fO_2 -24 doped with Au^0

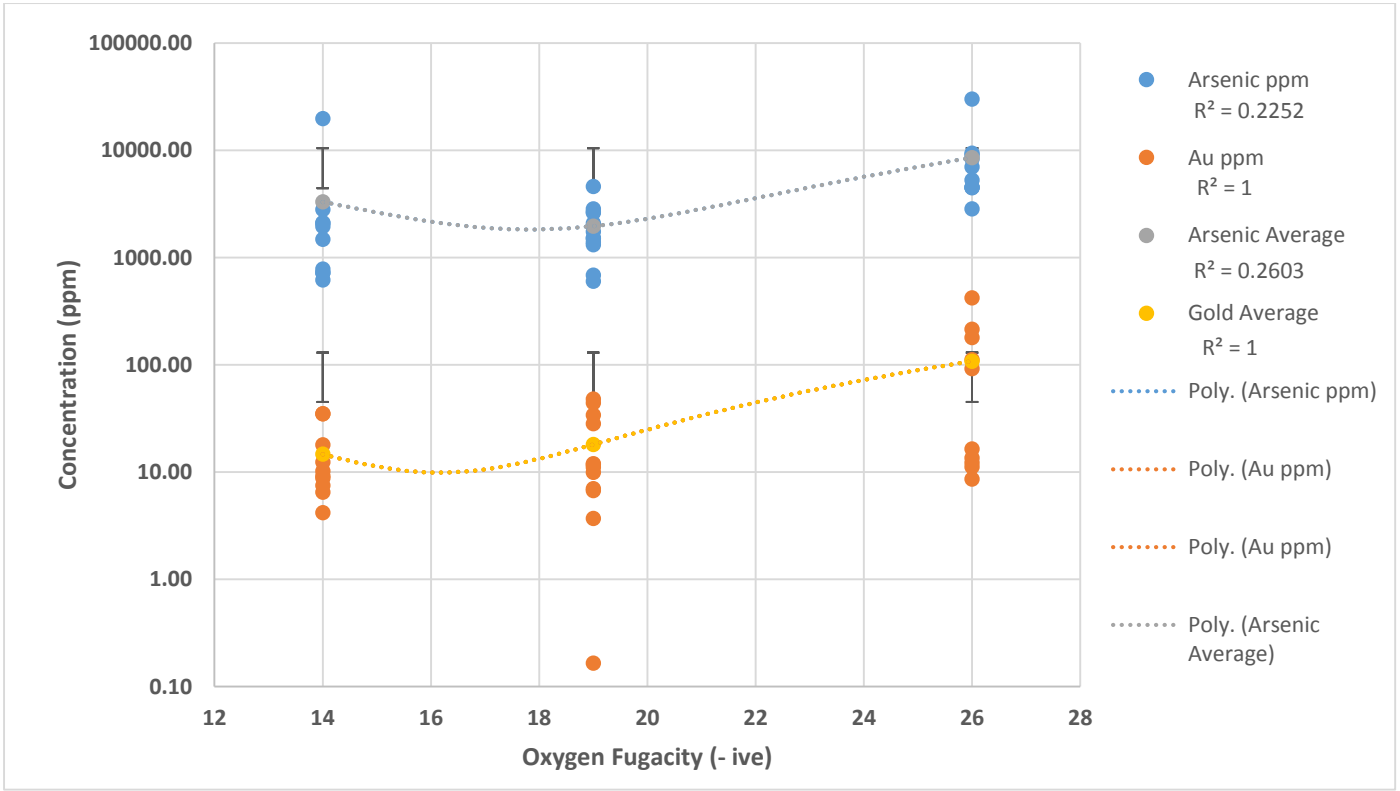

Figure 5.7: Average concentrations of Au and As in the experiments containing both. Error bars are standard deviation of results in each experimental run for 3 oxygen fugacities

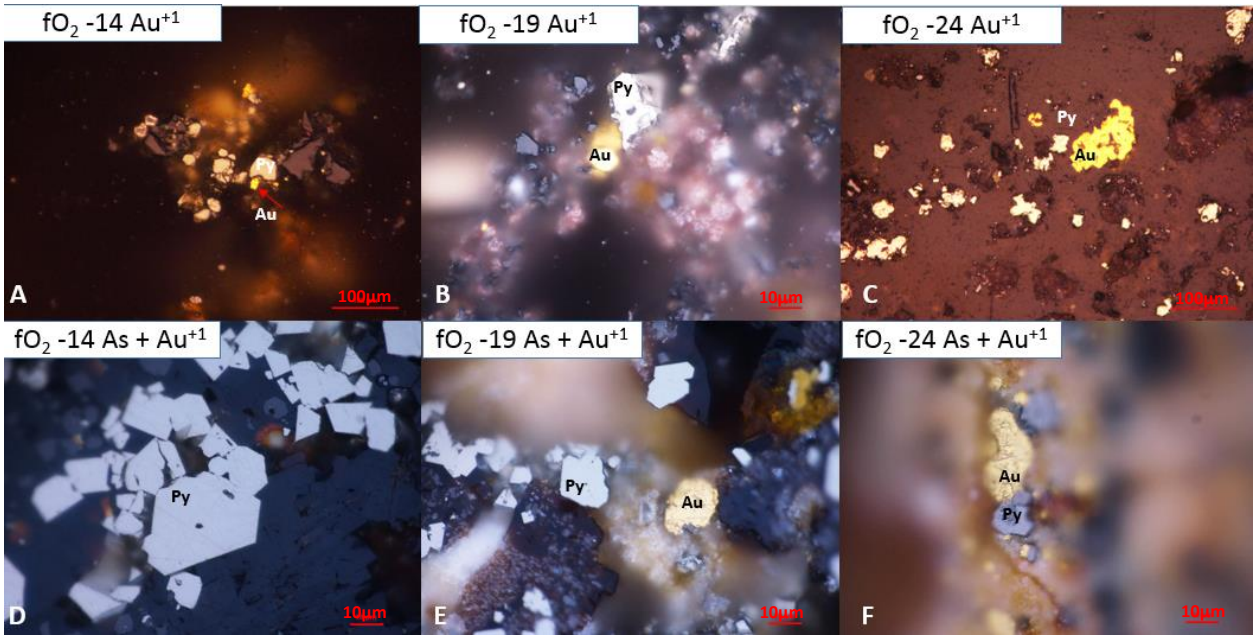

Figure 5.8: A) Pyrite grown at fO_2 -14 doped with Au^1 showing native gold B) Pyrite grown at fO_2 -19 doped with Au^1 and showing native gold C) Pyrite grown at fO_2 -24 doped with Au^1 showing native gold D) Pyrite grown at fO_2 -14 doped with Au^1 and As E) Pyrite grown at fO_2 -19 doped with Au^1 and As, showing native gold F) Pyrite grown at fO_2 -24 doped Au^1 and As and showing native gold.

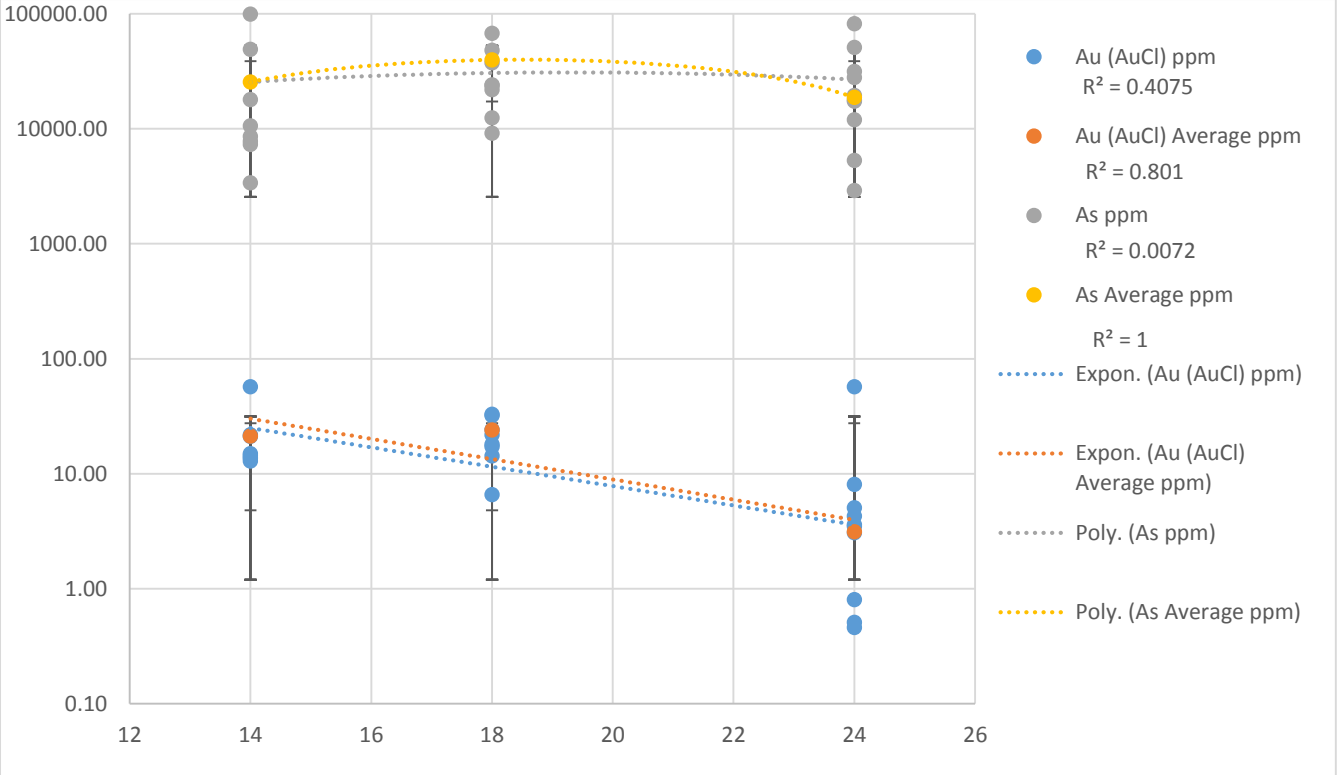

Figure 5.9: Average concentrations of Au^{+1} and experiments containing both. Error bars are standard deviation of results in each experimental run for 3 oxygen fugacities.

Observable native gold specks were found in Au^{+} only experiments independent of redox (at all fO_2). The highest concentration of Au in pyrite in these experiments was at the most reduced condition. Gold analyses exhibit higher standard deviations due to small unavoidable micro-inclusions of gold due to the nugget effect.

Observable gold flecks were also observed in the reduced experiments (-19 and -24) for experiments starting with Au^{+} + As. Coincidently, the highest Au concentration is observed in the most oxidized experiment.

Experiments starting with As+Au^{0} show clearly increasing As and Au concentrations in pyrite with reduction. The highest average Au and As concentration occurred at the lowest fO_2 ($logfO_2$ -24). When pyrite is doped with As and Au (regardless of oxidation state i.e Au^{0} or

Au^{+}) the concentrations of both elements co-vary, regardless of rexdox environment (Figure 5.7 and Figure 5.9).

Arsenic only experiments formed pore free euhedral crystals below fO_2 -24, where they developed a porous rim. Experiments with Au^0 all exhibited clear euhedral- anhedral crystals. Experiments starting with As+Au^0 all produced euhedral crystals, while those starting with As+Au^{+} produced clear rounded-anhedral crystals. Au^{+} experiments exhibited qualitatively smaller rounded crystals (Figure 5.5, Figure 5.6 and Figure 5.8).

5.4 DISCUSSION

Oxidation state and the occurance of bonanza grade Au

This study shows that the oxidation state of gold affects the mode and tenor of deposition. Experiments undertaken in the gas phase, demonstrate As and Au (Au^0 and Au^{+1}) do not solely concentrate in pyrite during reduction. Gold and As concentrate into pyrite over a large range of oxygen fugacity, which has not been previously shown, i.e Au and As co-existing in pyrite over fO_2 -14 to -24. The Au^{+} only experiments all exhibit Au inclusions regardless of fO_2, and the concentration of Au in pyrite is an order of magnitude higher than in the Au^0 only experiments. Further, in the Au^0 only experiments no visible Au inclusions are observed, suggesting that Au^{+} greatly reduces the solubility of Au.

This study shows that when Au (Au or Au^{+}) is in the presence of As the change in concentration of these trace elements covary during reduction. This supports the well established link between Au and As in pyrite, particularly the solubility curve determined by Reich et al. (2005). Further, As and Au, regardless of oxidation state substitute into pyrite via a coupled substitution. The Au^{+}+As experiments show that these elements concentrate most efficently

into pyrite under oxidised conditions in the absence of native Au formation. With further reduction, Au^{+}+As experiments show a decrease in trace elements in pyrite when comparing results from the most oxidised and reduced conditions. This coincides with the appearance of native Au. The Au^{+}+ As experiments result in gold in pyrite very similar to the Au^{0} + As experiments for fO_2 14 and 19 experiments, however the fO_2 24 Au^{0} is an order of magnitude higher. The concentration of As is also an order of magnitude higher across all AuCl + As experiments, suggesting that the difference in Au oxidation state facillitates deposition more than the presence of As.

Au^{0} + As experiments showed As and Au both concentrated systematically in pyrite according to a polynomial relationship that generally increased concentration with reduction however, native Au was only precipitated at logfO_2 -19. Gold concentrations in pyrite were greatest at the most reduced condition. Au^{0} deposition is an order of magnitude higher when in the presence of As under all redox conditions. This suggests that while Au^{0} is harder to attenuate, As can increase the incorporation of Au into the pyrite lattice, most likely by creating defects in its structure (Simon et al. 1999). The role of As on effecting deposition of native gold inclusions is not clear in this study.

While unmeasured, it is assumed that during the Au^{0} + As experiments, Au remained largely as Au^{0} or was incorporated into other minerals until significant reduction encouraged deposition into pyrite or as inclusions.

Gold in Pyrite in Natural Systems

Arsenic and Au are understood to concentrate strongly in pyrites that have crystallised during desulfidation (Figure 5.2). An example includes the low sulfidation-epithermal deposits of Emperor (Fiji) containing Au and As-rich pyrite formed as a result of an oxidised fluid

undergoing desulfidation (Hedenquist, 2000; Pals et al., 2003). Emperor displays 'invisible Au' (structural Au) within pyrite, similar to what is observed in this study in the oxidised As + Au^{+1} experiments. We assert that Au is most likely present in the Au^{+1} oxidation state to occur as 'structurally bound' Au via substitution (Chen et al. 2014). As both Au and As positively correlate under these conditions we suggest that low-sulfidation epithermal deposits are favourable to As^{-1} + Au^{3+} coupled substitution for Fe^{+2} , resulting in an expansion of the pyrite lattice (Chen et al. 2014). We also assert that As^{-1} can directly substitute for S^{-2}, thus explaining the high concentrations of As in all experiments starting with As and Au^{+1} compared to those starting with As and Au^{0}.

Rapid crystal growth can alter lattice configuration and result in irregular crystal formation, enabling greater trace element accumulation into the pyrite structure (Dowty, 1976; Tomm et al. 1995; Reich et al., 2005). Thus, changes in the crystal surface of any mineral due to the conditions under which it forms is more likely to affect crystal trace element concentrations as changes in oxidation state of elements at the surface may establish electronegative gradients favouring particular element adsorption This is a significant factor affecting Au in pyrite formation (Tomm et al., 1995). The results of Tomm et al. confirm the association of As and Au in pyrite formed under reduced conditions (Reich et al., 2005; Deditius et al., 2011).

Arsenic and Au concentrations generally increase with greater reduction in As+ Au^{0} experiments. The most reduced condition resulting in micro-Au inclusions within As-enriched pyrites.

Zhu and Tan (2011) assert that the fluids responsible for Carlin deposits were undersaturated in gold resulting in As-pyrite incorporating and subsequently concentrating rare Au from fluids during reduction, possibly as a result of preferential partitioning (As discussed in Chapter 3

of this thesis). Ore fluids have undergone decarbonisation and reactions with reduced sulfur during wall rock interactions that has resulted in the deposition of pyrite containing economic concentrations of submicron Au (Cline et al., 2005). Typically in Carlin deposits, Au is concentrated with As in rims at a later stage of mineralisation (Cline, 2001). This occurs by the greater As^{-1} concentration in the pyrite stucture making the pyrite surface relatively more electro-negative and thus more likely to adsorb Au^{+1} onto crystal surfaces (Simon et al., 1999). The enriched Au and As rims of Carlin pyrites, observed by Zhu and Tan, are similar to the As and Au enriched rims at Wallaby (WA) (Ward et al. 2017)(Laidler, 1987). We suggest that while hydrothermal deposits are thought to form from Au-saturated fluids, they are unlike Carlin style deposits, in which As scavenges Au either via coupled substitution (under oxidised, sulfur defficient environments such as Ladolam (PNG)) or by lowering the activation energy for sulfide formation (Lengke and Tempel, 2005). Laidler (1987) suggested that Au could catalyse homogenous and heterogenous substitution reactions by lowering activation energies by a factor or 2-10 in sulfides. The mechanism that may control this is based on Sabatier's Principle (suggesting there is an ideal ratio between substrate to reactant during reactions) and involves heterogeneous catalysis where the reactants (pyrite forming elements) adsorb onto the surface of trace catalyst atoms (or nanoparticles) of Au (Haruta, 1997; Haruta, 2005). When the Au is in oxidised form and in trace amounts in a fluid, the resulting surface attraction during crystallisation yields a 'domino' effect of concentrating gold into the pyrite structure, thereby lowering the activation energy.

The role of substitution and the formation of Au deposits

Pyrite can concentrate a heterogenous trace element array in ore-bearing deposits irrespective of origin (Raisewell and Plant, 1980; Large et al. 2009). While trace element

variations in pyrite are largely redox controlled and highly influenced by the presence (or absence) of sulfur, the presence of As and the oxidation state of Au in the fluid or magma significantly affects how Au attenuates in pyrite by affecting the geometry and amount of defects in the lattice available for exploitation. The pyrites produced in this study demonstrate the clear link between structural Au with As over a range of oxygen fugacities and the concentration of Au inclusions (free Au) with As. We suggest that when free Au inclusions form it is dependent on the oxidation state of Au, not solely reduction or the presence of As, i.e Au inclusions with pyrite crystals is not only identified in the most reduced condition. Single Au^{+1} experiments show that, in the absence of As, Au^{+1} is mostly concentrated as micro nuggets at the lowest oxygen fugacity. The As + Au^{0} experiments show no observable micro-nuggets and concentrate with As in structure sites. Interestingly, in As + Au^{+1} experiments, As generally decreases with reduction albeit not systematically, however the average Au concentration stays relatively stable between fO_2 14 and 18 but has lowest average of all experiments at the most reduced condition. Highly oxidised environments are understood to be relatively sulfide deficient, thus the As is believed to be directly substituting for S in the FeS_2 structure as $FeAs_xS_{(1-x)}$. This is consistent with Reich and Becker (2006) as the end-member FeAsS is shown to be energetically favourable at high oxygen fugacities.

Arsenic substitution and the potential of As fugacity in sulfur deficient deposits

The concentration of Au^{+1} and As under extremely oxidising conditions suggests that coupled substitution and direct ion exchange of Au^{+3} for Fe^{+2} may occur, similar to substitutions documented for pyrite formed under oxidising conditions at the Au-Ag-Cu Pascua deposit in Chile (Chouinard et al. 2005). In the present study, As is not as strongly correlated to Au^{+1}, likely because differences in oxidation state enables simpler substitution for Fe^{+2}. Hayashi and Ohmoto (1991) showed that Au solubility is independent of Cl^{-1} activity and pH, implying that chloride complexes are unimportant. Zajacz et al. (2017) showed that ore systems with abundant chloride form at lower activation energies i.e partitioning of Au into vapour in shallow environments is increased via metal-chloride reactions. There is much debate over the transport of Au in liquid and vapour and we propose that As, even in trace amounts, is extremely volatile and with multiple oxidation states, has a fugacity component similar to fS_2 in ore systems. That is, in deposits where S is deficient, volatile As species may play a controlling role in forming As-pyrite and/ or concentrating Au as either nano-inclusions or within mineral structures.

5.5 CONCLUSION

This study supports the widely observed Au-As relationship within pyrite in ore deposits. Experiments have shown that oxidation state of Au affects the mode and tenor of deposition to a greater extent than the presence of As. This study also establishes that Au and As concentrate into pyrite over a large range of oxygen fugacity and when Au (Au or Au^{+}) is in the presence of As, of both trace elements covary with respect to reduction.

This study demonstrates the link between structural Au deposited with As over a range of oxygen fugacities and the presence of Au inclusions (‘free gold’) with As.

The differences observed in Au and As concentration over the range of oxygen fugacities may explain Au deposition in natural systems i.e epithermal, hydrothermal.

APPENDIX 1

Table 5.3: Starting materials for all experiments, organized by dopants and redox condition.

fO_2	-14 (Fe_2O_3)	-19 ($Mt_{15}Usp_{85}$)	-24 ($Mt_{90}Usp_{10}$)
As	FeS (99.9%), S (99.999%), As (99.9%), $FeBr_3$ (98+%)		
Au^0	FeS (99.9%), S (99.999%), Au (99.9%), $FeBr_3$ (98+%)		
Au^{+1}	FeS (99.9%), S (99.999%), Au(I)Cl (99.9%), $FeBr_3$ (98+%)		
As+Au^0	FeS (99.9%), S (99.999%), As (99.9%), Au (99.9%), $FeBr_3$ (98+%)		
As+Au^{+1}	FeS (99.9%), S (99.999%), As (99.9%), Au(I)Cl(99.9%), $FeBr_3$ (98+%)		

APPENDIX 2

Table 5.4: Standard data for NIST SRM 612 and MASS-1 from the LA-ICPMS analyses

	As		Au	
	Av	**SD**	**Av**	**SD**
NIST SRM 612	40.6	10.7	5.3	0.4
MASS- 1	148	172.6	102	19

Table 5.5: Limits of Detection of Au and As from the LA –ICPMS

Element	LOD
As ppm	**11.48**
Au ppm	**0.33**

APPENDIX 3

Table 5.6: Average ppm values of As and Au in each experiment set.[ ] indicate which trace element measured for two-element experiments. Each doping experiment contains results from fO_2 -14, -19 and -24.

		Single Element Experiments			Au and As Experiments		AuCl and As Experiments	
		As ppm	Au ppm	AuCl ppm	As ppm	Au ppm	As ppm	Au ppm
14	Average	16487.14	9.51	87.95	1473.78	15.57	25447.50	21.25
	SD	5420.67	8.99	85.61	798.33	11.61	33066.35	14.86
19	Average	35566.67	7.17	25.91	1966.42	18.05	39637.50	24.03
	SD	21058.84	11.56	32.08	1101.48	16.23	25076.32	14.62
24	Average	51233.33	5.74	178.90	8545.00	108.09	18757.00	3.02
	SD	34349.77	5.23	167.36	7858.53	133.33	15073.08	2.47

Table 5.7: Data for each As only experiments

	Source file	Duration(s)	As_ppm_m75
Output_1_1	Py_As_14_11.d	3.9	19430.00
Output_1_2	Py_As_14_22.d	7.2	11730.00
Output_1_3	Py_As_14_3.d	7.8	11300.00
Output_1_4	Py_As_14_4.d	5.1	18200.00
Output_1_5	Py_As_14_5.d	3.3	14870.00
Output_1_6	Py_As_14_6.d	9.0	26600.00
Output_1_7	Py_As_14_7.d	4.8	13280.00
		Average	**16487.14**
		SD	**5420.67**
Output_1_9	Py_As_19.2.d	6.0	61900.00
Output_1_10	Py_As_19.3.d	6.3	54000.00
Output_1_11	Py_As_19.4.d	7.5	15400.00
Output_1_13	Py_As_19.6.d	12.6	9600.00
Output_1_14	Py_As_19.7.d	7.2	29100.00
Output_1_15	Py_As_19.8.d	5.7	43400.00
		Average	**35566.67**
		SD	**21058.84**
Output_1_16	Py_As_24.1.d	8.1	90600.00
Output_1_17	Py_As_24.2.d	5.4	13500.00
Output_1_19	Py_As_24.4.d	5.1	83000.00
Output_1_20	Py_As_24.5.d	5.1	72000.00
Output_1_21	Py_As_24.6.d	5.7	21100.00
Output_1_22	Py_As_24.7.d	5.1	27200.00
		Average	**51233.33**
		SD	**34349.77**

Table 5.8: Data for each Au0 only experiments

	Source file	Duration(s)	Au_ppm_m197
Output_1_118	Py_Au_14.1.d	5.0844	2.38
Output_1_119	Py_Au_14.1.d	5.9816	9.50
Output_1_120	Py_Au_14.1.d	7.178	2.24
Output_1_121	Py_Au_14.1.d	5.6826	9.00
Output_1_122	Py_Au_14.1.d	10.468	3.00
Output_1_123	Py_Au_14.1.d	6.5798	2.47
Output_1_124	Py_Au_14.1.d	2.6917	28.00
Output_1_125	Py_Au_14.1.d	4.7853	23.00
Output_1_126	Py_Au_14.1.d	4.7853	6.70
Output_1_127	Py_Au_14.1.d	4.1871	8.80
		Average	**9.51**
		SD	**8.99**
Output_1_128	Py_Au_19.1.d	5.0844	0.47
Output_1_129	Py_Au_19.1.d	5.3835	3.80
Output_1_130	Py_Au_19.1.d	4.7853	2.60
Output_1_131	Py_Au_19.1.d	3.8881	1.03
Output_1_132	Py_Au_19.1.d	5.9816	6.60
Output_1_133	Py_Au_19.1.d	4.4862	3.00
Output_1_134	Py_Au_19.1.d	6.5798	5.50
Output_1_135	Py_Au_19.1.d	6.5798	40.20
Output_1_136	Py_Au_19.1.d	3.8881	13.40
Output_1_137	Py_Au_19.1.d	5.3835	1.13
Output_1_138	Py_Au_19.1.d	5.6826	1.19
		Average	**7.17**
		SD	**11.56**
Output_1_140	Py_Au_24.1.d	7.7761	11.60
Output_1_141	Py_Au_24.1.d	3.589	5.10
Output_1_142	Py_Au_24.1.d	6.5798	17.00
Output_1_143	Py_Au_24.1.d	5.0844	9.50
Output_1_144	Py_Au_24.1.d	4.4862	2.60
Output_1_145	Py_Au_24.1.d	5.3835	1.26
Output_1_146	Py_Au_24.1.d	4.4862	2.02
Output_1_147	Py_Au_24.1.d	7.7761	2.76
Output_1_148	Py_Au_24.1.d	7.7761	3.10
Output_1_149	Py_Au_24.1.d	7.477	2.49
		Average	**5.74**
		SD	**5.23**

Table 5.9: Raw data for each Au^+ only experiments

	Source file	Duration(s)	Au_ppm_m197
Output_1_10	AuCl14.d	21.687	104.00
Output_1_11	AuCl14.d	21.068	190.00
Output_1_12	AuCl14.d	14.252	160.00
Output_1_13	AuCl14.d	21.068	0.76
Output_1_14	AuCl14.d	21.068	0.26
Output_1_15	AuCl14.d	21.068	160.00
Output_1_16	AuCl14.d	21.068	0.62
		Average	**87.95**
		SD	**85.61**
Output_1_18	AuCl19.d	16.11	53.00
Output_1_19	AuCl19.d	19.828	88.00
Output_1_20	AuCl19.d	15.491	40.00
Output_1_21	AuCl19.d	19.209	0.10
Output_1_22	AuCl19.d	17.969	1.87
Output_1_23	AuCl19.d	16.73	0.38
Output_1_24	AuCl19.d	21.068	20.00
Output_1_25	AuCl19.d	13.012	3.90
		Average	**25.91**
		SD	**32.08**
Output_1_151	Py_AuCl_24.1.d	5.0844	380.00
Output_1_152	Py_AuCl_24.1.d	5.9816	150.00
Output_1_154	Py_AuCl_24.1.d	6.8789	353.00
Output_1_155	Py_AuCl_24.1.d	8.3743	8.20
Output_1_156	Py_AuCl_24.1.d	7.178	25.00
Output_1_157	Py_AuCl_24.1.d	9.2715	63.00
Output_1_159	Py_AuCl_24.1.d	5.9816	390.00
Output_1_160	Py_AuCl_24.1.d	6.5798	62.00
		Average	**178.90**
		SD	**167.36**

Table 5.10: Raw data for each Au0 and As experiments

	Source file	Duration(s)	As_ppm_m75	Au_ppm_m197
Output_1_24	Py_As_Au_14.1.d	6.0	720.00	12.40
Output_1_25	Py_As_Au_14.2.d	7.2	1480.00	9.20
Output_1_26	Py_As_Au_14.3.1.d	4.8	620.00	8.80
Output_1_27	Py_As_Au_14.4.d	4.8	2110.00	18.00
Output_1_28	Py_As_Au_14.5.d	4.5	1950.00	7.50
Output_1_29	Py_As_Au_14.6.d	6.3	780.00	4.17
Output_1_31	Py_As_Au_14.8.d	8.7	724.00	35.00
Output_1_32	Py_As_Au_14.9.d	5.1	2800.00	10.20
Output_1_33	Py_As_Au_14.10.d	5.7	2080.00	34.90
		Average	**1473.78**	**15.57**
		SD	**798.33**	**11.61**
Output_1_34	Py_As_Au_19.1.d	5.4	685.00	0.17
Output_1_35	Py_As_Au_19.2.d	5.1	1510.00	12.00
Output_1_36	Py_As_Au_19.3.d	4.8	2610.00	7.00
Output_1_37	Py_As_Au_19.4.d	3.9	602.00	3.70
Output_1_38	Py_As_Au_19.5.d	6.9	1390.00	9.90
Output_1_39	Py_As_Au_19.6.d	5.1	1320.00	44.00
Output_1_40	Py_As_Au_19.6.d	3.9	1750.00	11.70
Output_1_41	Py_As_Au_19.6.d	9.3	2840.00	11.10
Output_1_42	Py_As_Au_19.6.d	4.8	2090.00	48.00
Output_1_43	Py_As_Au_19.6.d	5.7	1520.00	34.00
Output_1_44	Py_As_Au_19.6.d	4.5	2680.00	6.73
Output_1_45	Py_As_Au_19.6.d	5.7	4600.00	28.30
		Average	**1966.42**	**18.05**
		SD	**1101.48**	**16.23**
Output_1_46	Py_Au_As_24_1.d	4.8	9400.00	92.00
Output_1_47	Py_Au_As_24_1.d	3.6	9100.00	112.00
Output_1_48	Py_Au_As_24_1.d	5.1	30000.00	16.40
Output_1_49	Py_Au_As_24_1.d	6.0	4520.00	420.00
Output_1_50	Py_Au_As_24_1.d	6.3	7000.00	215.00
Output_1_51	Py_Au_As_24_1.d	6.0	8300.00	180.00
Output_1_52	Py_Au_As_24_1.d	5.4	5270.00	11.20
Output_1_53	Py_Au_As_24_1.d	6.9	4470.00	12.21
Output_1_54	Py_Au_As_24_1.d	6.9	4540.00	13.50
Output_1_55	Py_Au_As_24_1.d	9.0	2850.00	8.60
		Average	**8545.00**	**108.09**
		SD	**7858.53**	**133.33**

Table 5.11: Raw data for each Au^+ and As experiments

	Source file	Duration(s)	As_ppm_m75	Au_ppm_m197
Output_1_79	Py_As_AuCl_14.1.d	10.2	7300.00	13.60
Output_1_80	Py_As_AuCl_14.1.d	5.1	8600.00	57.00
Output_1_84	Py_As_AuCl_14.1.d	8.7	49000.00	21.20
Output_1_85	Py_As_AuCl_14.1.d	6.6	10600.00	21.90
Output_1_86	Py_As_AuCl_14.1.d	12.9	99000.00	12.90
Output_1_87	Py_As_AuCl_14.1.d	6.9	7800.00	15.00
Output_1_88	Py_As_AuCl_14.1.d	9.0	3380.00	13.90
Output_1_89	Py_As_AuCl_14.1.d	3.6	17900.00	14.50
		Average	**25447.50**	**21.25**
		SD	**33066.35**	**14.86**
Output_1_67	Py_AuCl_As_19.1.d	5.1	9130.00	32.00
Output_1_68	Py_AuCl_As_19.1.d	4.5	37400.00	6.60
Output_1_69	Py_AuCl_As_19.1.d	5.1	67600.00	21.90
Output_1_71	Py_AuCl_As_19.1.d	6.3	23800.00	24.20
Output_1_74	Py_AuCl_As_19.1.d	4.8	24000.00	18.00
Output_1_75	Py_AuCl_As_19.1.d	4.8	48000.00	33.00
Output_1_76	Py_AuCl_As_19.1.d	5.7	21900.00	14.30
Output_1_77	Py_AuCl_As_19.1.d	11.7	12400.00	17.20
Output_1_78	Py_AuCl_As_19.1.d	4.5	82000.00	57.00
		Average	**39637.50**	**24.03**
		SD	**25076.32**	**14.62**
Output_1_56	Py_As_AuCl_24.1.d	3.6	51000.00	3.08
Output_1_57	Py_As_AuCl_24.1.d	12.3	19500.00	4.30
Output_1_59	Py_As_AuCl_24.1.d	7.2	17400.00	3.50
Output_1_60	Py_As_AuCl_24.1.d	7.2	31600.00	0.51
Output_1_61	Py_As_AuCl_24.1.d	7.5	2900.00	0.81
Output_1_62	Py_As_AuCl_24.1.d	10.2	5300.00	0.46
Output_1_63	Py_As_AuCl_24.1.d	6.6	17800.00	3.60
Output_1_64	Py_As_AuCl_24.1.d	7.2	27900.00	5.06
Output_1_65	Py_As_AuCl_24.1.d	5.1	12000.00	8.10
Output_1_66	Py_As_AuCl_24.1.d	9.3	2170.00	0.75
		Average	**18757.00**	**3.02**
		SD	**15073.08**	**2.47**

6. REFERENCES

Abraitis, P., Pattrick, R. and Vaughan, D., 2004. Variations in the compositional, textural and electrical properties of natural pyrite: a review. International Journal of Mineral Processing, 74(1-4): 41-59.

Agangi, A., Hofmann, A., Rollion-Bard, C., Marin-Carbonne, J., Cavalazzi, B., Large, R. and Meffre, S., 2015. Gold accumulation in the Archaean Witwatersrand Basin, South Africa—Evidence from concentrically laminated pyrite. Earth-Science Reviews, 140: 27-53.

Ahrens, L.H., 1952. The use of ionization potentials Part 1. Ionic radii of the elements. Geochimica et cosmochimica Acta, 2(3): 155-169.

Arehart, G.B., Chryssoulis, S.L. and Kesler, S.E., 1993. Gold and arsenic in iron sulfides from sediment-hosted disseminated gold deposits; implications for depositional processes. Economic Geology, 88(1): 171-185.

Bajwah, Z., Seccombe, P. and Offler, R., 1987. Trace element distribution, Co: Ni ratios and genesis of the Big Cadia iron-copper deposit, New South Wales, Australia. Mineralium Deposita, 22(4): 292-300.

Bancroft, G. and Hyland, M., 1990. Spectroscopic studies of adsorption/reduction reactions of aqueous metal complexes on sulphide surfaces. Reviews in Mineralogy and Geochemistry, 23(1): 511-558.

Bath, A.B., Walshe, J.L., Cloutier, J., Verrall, M., Cleverley, J.S., Pownceby, M.I., Macrae, C.M., Wilson, N.C., Tunjic, J. and Nortje, G.S., 2013. Biotite and apatite as tools for tracking pathways of oxidized fluids in the Archean East Repulse gold deposit, Australia. Economic Geology, 108(4): 667-690.

Belcher, R., Rozendaal, A. and Przybylowicz, W., 2004. Trace element zoning in pyrite determined by PIXE elemental mapping: evidence for varying ore–fluid composition and electrochemical precipitation of gold at the Spitskop deposit, Saldania Belt, South Africa. X-Ray Spectrometry: An International Journal, 33(3): 174-180.

Belousov, I., Large, R., Meffre, S., Danyushevsky, L., Steadman, J. and Beardsmore, T., 2016. Pyrite compositions from VHMS and orogenic Au deposits in the Yilgarn Craton, Western Australia: Implications for gold and copper exploration. Ore Geology Reviews, 79: 474-499.

Belousova, E., Griffin, W., O'Reilly, S.Y. and Fisher, N., 2002. Igneous zircon: trace element composition as an indicator of source rock type. Contributions to Mineralogy and Petrology, 143(5): 602-622.

Blevin, P.L., 2004. Redox and compositional parameters for interpreting the granitoid metallogeny of eastern Australia: Implications for gold-rich ore systems. Resource Geology, 54(3): 241-252.

Blevin, P.L., Chappell, B.W. and Allen, C.M., 1996. Intrusive metallogenic provinces in eastern Australia based on granite source and composition. Geological Society of America Special Papers, 315: 281-290.

Blewett, R., Czarnota, K. and Henson, P., 2010. Structural-event framework for the eastern Yilgarn Craton, Western Australia, and its implications for orogenic gold. Precambrian Research, 183(2): 203-229.

Bostick, B.C. and Fendorf, S., 2003. Arsenite sorption on troilite (FeS) and pyrite (FeS2). Geochimica et cosmochimica Acta, 67(5): 909-921.

Boutroy, E., Dare, S.A., Beaudoin, G., Barnes, S.-J. and Lightfoot, P.C., 2014. Magnetite composition in Ni-Cu-PGE deposits worldwide: application to mineral exploration. Journal of Geochemical Exploration, 145: 64-81.

Buddington, A. and Lindsley, D., 1964. Iron-titanium oxide minerals and synthetic equivalents. Journal of petrology, 5(2): 310-357.

Burnham, A. and Berry, A., 2017. Formation of Hadean granites by melting of igneous crust. Nature Geoscience, 10(6): 457.

Campbell, I. and Naldrett, A., 1979. The influence of silicate: sulfide ratios on the geochemistry of magmatic sulfides. Economic Geology, 74(6): 1503-1506.

Candela, P.A. and Bouton, S.L., 1990. The influence of oxygen fugacity on tungsten and molybdenum partitioning between silicate melts and ilmenite. Economic Geology, 85(3): 633-640.

Candela, P.A. and Holland, H.D., 1984. The partitioning of copper and molybdenum between silicate melts and aqueous fluids. Geochimica et Cosmochimica Acta, 48(2): 373-380.

Chappell, B., Bryant, C., Wyborn, D., White, A. and Williams, I., 1998. High-and Low-Temperature I-type Granites. Resource Geology, 48(4): 225-235.

Chappell, B., English, P., King, P., White, A. and Wyborn, D., 1991. Granites and related rocks of the Lachlan Fold Belt (1: 1 250 000 scale map). Bureau of Mineral Resources, Canberra.

Chappell, B. and White, A., 1974. Two contrasting granite types. Pacific geology, 8(2): 173-174.

Chappell, B. and White, A., 1992. I-and S-type granites in the Lachlan Fold Belt. Geological Society of America Special Papers, 272: 1-26.

Chappell, B. and White, A.J.R., 2001. Two contrasting granite types: 25 years later. Australian Journal of Earth Sciences, 48(4): 489-499.

Chen, J.-H., Li, Y.-Q. and Zhong, S.-P., 2013. DFT simulation of the occurrences and correlation of gold and arsenic in pyrite. American Mineralogist, 98(10): 1765-1771.

Chen, J., Li, Y. and Zhao, C., 2014a. First principles study of the occurrence of gold in pyrite. Computational materials science, 88: 1-6.

Chen, J., Li, Y. and Zhao, C., 2014b. First principles study of the occurrence of gold in pyrite. Computational Materials Science, 88(Supplement C): 1-6.

Clarke, M. and Beddoe-Stephens, B., 1987. Geochemistry, mineralogy and plate tectonic setting of a Late Cretaceous Sn-W granite from Sumatra, Indonesia. Mineralogical Magazine, 51(361): 371-387.

Cleverley, J.S., Benning, L.G. and Mountain, B.W., 2003. Reaction path modelling in the As–S system: a case study for geothermal As transport. Applied Geochemistry, 18(9): 1325-1345.

Cline, J.S., 2001. Timing of gold and arsenic sulfide mineral deposition at the Getchell Carlin-type gold deposit, north-central Nevada. Economic Geology, 96(1): 75-89.

Cline, J.S., Hofstra, A.H., Muntean, J.L., Tosdal, R.M. and Hickey, K.A., 2005. Carlin-type gold deposits in Nevada: Critical geologic characteristics and viable models. Economic Geology 100th anniversary volume, 451: 484.

Collins, W. and Richards, S., 2008. Geodynamic significance of S-type granites in circum-Pacific orogens. Geology, 36(7): 559-562.

Cook, N.J. and Chryssoulis, S.L., 1990. Concentrations of invisible gold in the common sulfides. The Canadian Mineralogist, 28(1): 1-16.

Cox, S., 2010. The application of failure mode diagrams for exploring the roles of fluid pressure and stress states in controlling styles of fracture-controlled permeability enhancement in faults and shear zones. Geofluids, 10(1-2): 217-233.

Cox, S. and Ruming, K., 2004. The St Ives mesothermal gold system, Western Australia—a case of golden aftershocks? Journal of Structural Geology, 26(6): 1109-1125.

Cox, S.F., 1995. Faulting processes at high fluid pressures: an example of fault valve behavior from the Wattle Gully Fault, Victoria, Australia. Journal of Geophysical Research: Solid Earth, 100(B7): 12841-12859.

Craig, J., Vokes, F. and Solberg, T., 1998. Pyrite: physical and chemical textures. Mineralium Deposita, 34(1): 82-101.

Crawford, M., 2011. Dynamic Coupling Between Deformation Processes, Fluid-Rock Interaction, and Gold Deposition in the Argo Gold Deposit, St Ives, Western Australia. Unpublished Thesis Thesis, The Australian National University.

Crerar, D.A., Susak, N., Borcsik, M. and Schwartz, S., 1978. Solubility of the buffer assemblage pyrite+ pyrrhotite+ magnetite in NaCl solutions from 200 to 350 C. Geochimica et Cosmochimica Acta, 42(9): 1427-1437.

Deditius, A.P., Reich, M., Kesler, S.E., Utsunomiya, S., Chryssoulis, S.L., Walshe, J. and Ewing, R.C., 2014. The coupled geochemistry of Au and As in pyrite from hydrothermal ore deposits. Geochimica et Cosmochimica Acta, 140: 644-670.

Deditius, A.P., Utsunomiya, S., Reich, M., Kesler, S.E., Ewing, R.C., Hough, R. and Walshe, J., 2011. Trace metal nanoparticles in pyrite. Ore Geology Reviews, 42(1): 32-46.

Deditius, A.P., Utsunomiya, S., Renock, D., Ewing, R.C., Ramana, C.V., Becker, U. and Kesler, S.E., 2008. A proposed new type of arsenian pyrite: Composition, nanostructure and geological significance. Geochimica et Cosmochimica Acta, 72(12): 2919-2933.

Deyell, C. and Tosdal, R., 2005. Alkalic Cu-Au deposits of British Columbia: Sulfur isotope zonation as a guide to mineral exploration. British Columbia Ministry of Energy and Mines, Geological Fieldwork Paper, 1: 191-208.

Dmitrijeva, M., Cook, N.J., Ehrig, K., Ciobanu, C.L., Metcalfe, A.V., Kamenetsky, M., Kamenetsky, V.S. and Gilbert, S., 2020. Multivariate statistical analysis of trace elements in pyrite: prediction, bias and artefacts in defining mineral signatures. Minerals, 10(1): 61.

Dowty, E., 1976. Crystal structure and crystal growth; II, Sector zoning in minerals. American Mineralogist, 61(5-6): 460-469.

Dubosq, R., Rogowitz, A., Schweinar, K., Gault, B. and Schneider, D.A., 2019. A 2D and 3D nanostructural study of naturally deformed pyrite: assessing the links between trace element mobility and defect structures. Contributions to Mineralogy and Petrology, 174(9): 72.

Eberz, G.W. and Nicholls, I.A., 1990. Chemical modification of enclave magma by post-emplacement crystal fractionation, diffusion and metasomatism. Contributions to Mineralogy and Petrology, 104(1): 47-55.

Fleet, M., E. and Mumin, A.H., 1997a. Gold-bearing arsenian pyrite and marcasite and arsenopyrite from Carlin Trend gold deposits and laboratory synthesis, American Mineralogist, pp. 182.

Fleet, M.E., Chryssoulis, S.L., Stone, W.E. and Weisener, C.G., 1993. Partitioning of platinum-group elements and Au in the Fe− Ni− Cu− S system: experiments on the fractional

crystallization of sulfide melt. Contributions to Mineralogy and Petrology, 115(1): 36-44.

Fleet, M.E. and Mumin, A.H., 1997b. Gold-bearing arsenian pyrite and marcasite and arsenopyrite from Carlin Trend gold deposits and laboratory synthesis. American Mineralogist, 82(1-2): 182-193.

Fontboté, L., Kouzmanov, K., Chiaradia, M. and Pokrovski, G.S., 2017. Sulfide minerals in hydrothermal deposits. Elements, 13(2): 97-103.

Fougerouse, D., Reddy, S.M., Kirkland, C.L., Saxey, D.W., Rickard, W.D. and Hough, R.M., 2019. Time-resolved, defect-hosted, trace element mobility in deformed Witwatersrand pyrite. Geoscience Frontiers, 10(1): 55-63.

Frikken, P.H., Cooke, D.R., Walshe, J.L., Archibald, D., Skarmeta, J., Serrano, L. and Vargas, R., 2005. Mineralogical and isotopic zonation in the Sur-Sur tourmaline breccia, Rio Blanco-Los Bronces Cu-Mo deposit, Chile: Implications for ore genesis. Economic Geology, 100(5): 935-961.

Gavelin, S., 1947. Spectrochemical investigations of sulphide minerals from the ores of the Skellefte district.

Godefroy-Rodríguez, M., Hagemann, S., Frenzel, M. and Evans, N.J., 2020. Laser ablation ICP-MS trace element systematics of hydrothermal pyrite in gold deposits of the Kalgoorlie district, Western Australia. Mineralium Deposita: 1-22.

Godefroy-Rodríguez, M., Hagemann, S., LaFlamme, C. and Fiorentini, M., 2018. The multiple sulfur isotope architecture of the Golden Mile and Mount Charlotte deposits, Western Australia. Mineralium Deposita.

Goldfarb, R.J. and Groves, D.I., 2015. Orogenic gold: Common or evolving fluid and metal sources through time. Lithos, 233: 2-26.

Gregory, D., Mukherjee, I., Olson, S.L., Large, R.R., Danyushevsky, L.V., Stepanov, A.S., Avila, J.N., Cliff, J., Ireland, T.R. and Raiswell, R., 2019. The formation mechanisms of sedimentary pyrite nodules determined by trace element and sulfur isotope microanalysis. Geochimica et Cosmochimica Acta, 259: 53-68.

Gregory, D.D., Large, R.R., Bath, A.B., Steadman, J.A., Wu, S., Danyushevsky, L., Bull, S.W., Holden, P. and Ireland, T.R., 2016. Trace element content of pyrite from the kapai slate, St. Ives Gold District, Western Australia. Economic Geology, 111(6): 1297-1320.

Groves, D., 1993. The crustal continuum model for late-Archaean lode-gold deposits of the Yilgarn Block, Western Australia. Mineralium deposita, 28(6): 366-374.

Hageman, S. and Cassidy, K., 2000. Archean orogenic lode deposits. Gold in 2000: 9-68.

Hall, A., 1986. Pyrite-pyrrhotine redox reactions in nature. Mineralogical Magazine, 50: 223-9.

Haruta, M., 1997. Size- and support-dependency in the catalysis of gold. Catalysis Today, 36(1): 153-166.

Haruta, M., 2005. Catalysis: gold rush. Nature, 437(7062): 1098-9.

Hawley, J. and Nichol, I., 1961. Trace elements in pyrite, pyrrhotite and chalcopyrite of different ores. Economic Geology, 56(3): 467-487.

Hayashi, K.-i. and Ohmoto, H., 1991. Solubility of gold in NaCl-and H2S-bearing aqueous solutions at 250–350 C. Geochimica et Cosmochimica Acta, 55(8): 2111-2126.

Hedenquist, J.W. and Lowenstern, J.B., 1994. The role of magmas in the formation of hydrothermal ore deposits. Nature, 370(6490): 519-527.

Hedenquist, J.W.A., A ; Gonzalez-Urien, E, 2000. Exploration for Epithermal Gold Deposits. SEG Reviews, 13: 245-277.

Holden, P., Halliday, A.N., Stephens, W.E. and Henney, P.J., 1991. Chemical and isotopic evidence for major mass transfer between mafic enclaves and felsic magma. Chemical Geology, 92(1): 135-152.

Howe, D., 2002. Hydrothermal alteration and gold size distribution at the Argo A1 Ore Body, Argo Gold Deposit, Kambalda, Western Australia. University of Western Australia.

ISHIHARA, S., 1998. Granitoid series and mineralization in the Circum-Pacific Phanerozoic granitic belts. Resource Geology, 48(4): 219-224.

Ishihara, S., Sawata, H., Arpornsuwan, S., Busaracome, P. and Bungbrakearti, N., 1979. The magnetite-series and ilmenite-series granitoids and their bearing on tin mineralization, particularly of the Malay Peninsula region. Bulletin of the Geological Society of Malaysia, 11: 103-110.

Jochum, K.P., Nohl, U., Herwig, K., Lammel, E., Stoll, B. and Hofmann, A.W., 2005. GeoReM: A New Geochemical Database for Reference Materials and Isotopic Standards. Geostandards and Geoanalytical Research, 29(3): 333-338.

Keith, M., Smith, D.J., Jenkin, G.R., Holwell, D.A. and Dye, M.D., 2018. A review of Te and Se systematics in hydrothermal pyrite from precious metal deposits: Insights into ore-forming processes. Ore Geology Reviews, 96: 269-282.

Kerrich, R. and Cassidy, K.F., 1994. Temporal relationships of lode gold mineralization to accretion, magmatism, metamorphism and deformation—Archean to present: A review. Ore Geology Reviews, 9(4): 263-310.

King, J., Williams-Jones, A., van Hinsberg, V. and Williams-Jones, G., 2014. High-sulfidation epithermal pyrite-hosted Au (Ag-Cu) ore formation by condensed magmatic vapors on Sangihe Island, Indonesia. Economic Geology, 109(6): 1705-1733.

Kojonen, K. and Johanson, B., 1999. Determination of refractory gold distribution by microanalysis, diagnostic leaching and image analysis. Mineralogy and Petrology, 67(1-2): 1-19.

Kullerud, G. and Yoder, H.S., 1959. Pyrite stability relations in the Fe-S system. Economic Geology, 54(4): 533-572.

Kusebauch, C., Oelze, M. and Gleeson, S.A., 2018. Partitioning of arsenic between hydrothermal fluid and pyrite during experimental siderite replacement. Chemical Geology, 500: 136-147.

LaFlamme, C., Sugiono, D., Thébaud, N., Caruso, S., Fiorentini, M., Selvaraja, V., Jeon, H., Voute, F. and Martin, L., 2018. Multiple sulfur isotopes monitor fluid evolution of an Archean orogenic gold deposit. Geochimica et Cosmochimica Acta, 222: 436-446.

Laidler, K.J., 1987. Chemical kinetics.

Large, S.J., Bakker, E.Y., Weis, P., Wälle, M., Ressel, M. and Heinrich, C.A., 2016. Trace elements in fluid inclusions of sediment-hosted gold deposits indicate a magmatic-hydrothermal origin of the Carlin ore trend. Geology, 44(12): 1015-1018.

Lehner, S., Savage, K. and Ayers, J., 2006a. Vapor growth and characterization of pyrite (FeS2) doped with Co, Ni, and As: Variations in semiconducting properties. Journal of Crystal Growth, 286(2): 306-317.

Lehner, S., Savage, K. and Ayers, J., 2006b. Vapor growth and characterization of pyrite (FeS 2) doped with Co, Ni, and As: variations in semiconducting properties. Journal of Crystal Growth, 286(2): 306-317.

Lehner, S., Savage, K., Ciobanu, M. and Cliffel, D.E., 2007. The effect of As, Co, and Ni impurities on pyrite oxidation kinetics: An electrochemical study of synthetic pyrite. Geochimica et Cosmochimica Acta, 71(10): 2491-2509.

Lengke, M.F. and Tempel, R.N., 2005. Geochemical modeling of arsenic sulfide oxidation kinetics in a mining environment. Geochimica et Cosmochimica Acta, 69(2): 341-356.

Liang, J.-l., Sun, W.-d., Li, Y.-l., Zhu, S.-y., Li, H., Liu, Y.-l. and Zhai, W., 2013. An XPS study on the valence states of arsenic in arsenian pyrite: implications for Au deposition mechanism of the Yang-shan Carlin-type gold deposit, western Qinling belt. Journal of Asian Earth Sciences, 62: 363-372.

Liu, W., Etschmann, B., Testemale, D., Hazemann, J.-L., Rempel, K., Müller, H. and Brugger, J., 2014. Gold transport in hydrothermal fluids: Competition among the Cl−, Br−, HS− and NH3 (aq) ligands. Chemical Geology, 376: 11-19.

Loftus -Hills , G. and Solomon , M., 1967. Cobalt, nickel and selenium in sulphides as indicators of ore genesis. Mineral, Deposita, 2: 228-242.

Longerich, H.P., Günther, D. and Jackson, S.E., 1996. Elemental fractionation in laser ablation inductively coupled plasma mass spectrometry. Fresenius' journal of analytical chemistry, 355(5-6): 538-542.

Loucks, R.R. and Mavrogenes, J.A., 1999. Gold Solubility in Supercritical Hydrothermal Brines Measured in Synthetic Fluid Inclusions. Science, 284(5423): 2159-2163.

Maddox, L.M., Bancroft, G.M., Scaini, M. and Lorimer, J., 1998. Invisible gold: Comparison of Au deposition on pyrite and arsenopyrite. American Mineralogist, 83(12): 1240-1245.

Mann, S., Sparks, N.H., Frankel, R.B., Bazylinski, D.A. and Jannasch, H.W., 1990. Biomineralization of ferrimagnetic greigite (Fe 3 S 4) and iron pyrite (FeS 2) in a magnetotactic bacterium. Nature, 343(6255): 258-261.

McCuaig, T.C. and Kerrich, R., 1998. P—T—t—deformation—fluid characteristics of lode gold deposits: evidence from alteration systematics. Ore Geology Reviews, 12(6): 381-453.

McCulloch, M.T. and Chappell, B.W., 1982. Nd isotopic characteristics of S-and I-type granites. Earth and Planetary Science Letters, 58(1): 51-64.

McGoldrick, K., Squire, R.J., Cas, R., Briggs, M., Tunjic, J., Allen, C.M., Campbell, I. and Hayman, P., 2013a. The largest Au deposits in the St Ives Goldfield (Yilgarn Craton, Western Australia) may be located in a major Neoarchean volcano-sedimentary depo-centre. Mineralium Deposita, 48(7): 861-881.

McGoldrick, K.L., Squire, R.J., Cas, R.A.F., Briggs, M., Tunjic, J., Allen, C.M., Campbell, I.H. and Hayman, P.C., 2013b. The largest Au deposits in the St Ives Goldfield (Yilgarn Craton, Western Australia) may be located in a major Neoarchean volcano-sedimentary depo-centre. Mineralium Deposita, 48(7): 861-881.

Moritz, R., 2000. What have we learnt about orogenic lode gold deposits over the past 20 years. Scientific Communication. Section des Sciences de la Terre., University of Geneva, Switzerland: 1-7.

Mycroft, J., Bancroft, G., McIntyre, N. and Lorimer, J., 1995. Spontaneous deposition of gold on pyrite from solutions containing Au (III) and Au (I) chlorides. Part I: A surface study. Geochimica et Cosmochimica Acta, 59(16): 3351-3365.

Myers, J., 1997. Preface: Archaean geology of the Eastern Goldfields of Western Australia—regional overview. Elsevier.

Nelson, D., 2008. Geochronology of the Archean of Australia. Australian Journal of Earth Sciences, 55(6-7): 779-793.

Nesse, W., 2009. Introduction to Optical Mineralogy (international edition). Oxford University Press.

Neumayr, P., Walshe, J., Hagemann, S., Petersen, K., Roache, A., Frikken, P., Horn, L. and Halley, S., 2008. Oxidized and reduced mineral assemblages in greenstone belt rocks

of the St. Ives gold camp, Western Australia: vectors to high-grade ore bodies in Archaean gold deposits? Mineralium Deposita, 43(3): 363-371.

Ohmoto, H., 1972. Systematics of sulfur and carbon isotopes in hydrothermal ore deposits. Economic Geology, 67(5): 551-578.

Ovens, G., 2014. Gold Fields Australia Site Visit: St Ives Gold Mine.

Palin, J. and Xu, Y., 2000. Gilt by association? Origins of pyritic gold ores in the Victory mesothermal gold deposit, Western Australia. Economic Geology, 95(8): 1627-1634.

Pals, D.W., Spry, P.G. and Chryssoulis, S., 2003. Invisible gold and tellurium in arsenic-rich pyrite from the Emperor gold deposit, Fiji: implications for gold distribution and deposition. Economic Geology, 98(3): 479-493.

Park, J.-W., Campbell, I.H., Ickert, R.B. and Allen, C.M., 2013. Chalcophile element geochemistry of the Boggy Plain zoned pluton, southeastern Australia: a S-saturated barren compositionally diverse magmatic system. Contributions to Mineralogy and Petrology, 165(2): 217-236.

Peterson, E.C. and Mavrogenes, J.A., 2014. Linking high-grade gold mineralization to earthquake-induced fault-valve processes in the Porgera gold deposit, Papua New Guinea. Geology, 42(5): 383-386.

Plant, J., Breward, N., Simpson, P. and Slater, D., 1990. Regional geochemistry and the identification of metallogenic provinces: examples from lead-zinc-barium, tin-uranium and gold deposits. Journal of Geochemical Exploration, 39(1-2): 195-224.

Pokrovski, G.S., Borisova, A.Y. and Harrichoury, J.-C., 2008. The effect of sulfur on vapor–liquid fractionation of metals in hydrothermal systems. Earth and Planetary Science Letters, 266(3): 345-362.

Pokrovski, G.S., Roux, J. and Harrichoury, J.-C., 2005. Fluid density control on vapor-liquid partitioning of metals in hydrothermal systems. Geology, 33(8): 657-660.

Prendergast, K., 2007. Application of lithogeochemistry to gold exploration in the St Ives goldfield, Western Australia. Geochemistry: Exploration, Environment, Analysis, 7(2): 99-108.

Reich, M. and Becker, U., 2006. First-principles calculations of the thermodynamic mixing properties of arsenic incorporation into pyrite and marcasite. Chemical Geology, 225(3-4): 278-290.

Reich, M., Deditius, A., Chryssoulis, S., Li, J.-W., Ma, C.-Q., Parada, M.A., Barra, F. and Mittermayr, F., 2013. Pyrite as a record of hydrothermal fluid evolution in a porphyry copper system: A SIMS/EMPA trace element study. Geochimica et Cosmochimica Acta, 104: 42-62.

Reich, M., Kesler, S.E., Utsunomiya, S., Palenik, C.S., Chryssoulis, S.L. and Ewing, R.C., 2005. Solubility of gold in arsenian pyrite. Geochimica et Cosmochimica Acta, 69(11): 2781-2796.

Roberts, D.E., Elias, M.,, 1990. Gold deposits of the St Ives–Kambalda

region. . The Australasian Institute of Mining

and Metallurgy, Melbourne.

Rowins, S.M., 2000. Reduced porphyry copper-gold deposits: A new variation on an old theme. Geology, 28(6): 491-494.

Rye, R.O., 2005. A review of the stable-isotope geochemistry of sulfate minerals in selected igneous environments and related hydrothermal systems. Chemical Geology, 215(1-4): 5-36.

Rye, R.O. and Ohmoto, H., 1974. Sulfur and carbon isotopes and ore genesis: a review. Economic Geology, 69(6): 826-842.

Sasaki, A. and Ishihara, S., 1979. Sulfur isotopic composition of the magnetite-series and ilmenite-series granitoids in Japan. Contributions to Mineralogy and Petrology, 68(2): 107-115.

Seward, T.M., 1973. Thio complexes of gold and the transport of gold in hydrothermal ore solutions. Geochimica et Cosmochimica Acta, 37(3): 379-399.

Sibson, R.H., Robert, F. and Poulsen, K.H., 1988. High-angle reverse faults, fluid-pressure cycling, and mesothermal gold-quartz deposits. Geology, 16(6): 551-555.

Simon, A.C., Pettke, T., Candela, P.A., Piccoli, P.M. and Heinrich, C.A., 2007. The partitioning behavior of As and Au in S-free and S-bearing magmatic assemblages. Geochimica et Cosmochimica Acta, 71(7): 1764-1782.

Simon, G., Huang, H., Penner-Hahn, J.E., Kesler, S.E. and Kao, L.-S., 1999. Oxidation state of gold and arsenic in gold-bearing arsenian pyrite. American Mineralogist, 84(7-8): 1071-1079.

Skirrow, R.G. and Walshe, J.L., 2002. Reduced and oxidized Au-Cu-Bi iron oxide deposits of the Tennant Creek inlier, Australia: An integrated geologic and chemical model. Economic Geology, 97(6): 1167-1202.

Stefánsson, A. and Seward, T., 2004. Gold (I) complexing in aqueous sulphide solutions to 500 C at 500 bar. Geochimica et Cosmochimica Acta, 68(20): 4121-4143.

Sung, Y.-H., Brugger, J., Ciobanu, C., Pring, A., Skinner, W. and Nugus, M., 2009. Invisible gold in arsenian pyrite and arsenopyrite from a multistage Archaean gold deposit: Sunrise Dam, Eastern Goldfields Province, Western Australia. Mineralium Deposita, 44(7): 765.

Thode, H., 1970. Sulfur isotope geochemistry and fractionation between coexisting sulfide minerals. Mineralogical Society of America Special Paper, 3: 133-144.

Tomm, Y., Schieck, R., Ellmer, K. and Fiechter, S., 1995. Growth mechanism and electronic properties of doped pyrite (FeS2) crystals. Journal of crystal growth, 146(1-4): 271-276.

Toulmin III, P. and Barton Jr, P.B., 1964. A thermodynamic study of pyrite and pyrrhotite. Geochimica et Cosmochimica Acta, 28(5): 641-671.

Trail, D., Tailby, N.D., Lanzirotti, A., Newville, M., Thomas, J.B. and Watson, E.B., 2015a. Redox evolution of silicic magmas: Insights from XANES measurements of Ce valence in Bishop Tuff zircons. Chemical Geology, 402: 77-88.

Trail, D., Tailby, N.D., Sochko, M. and Ackerson, M.R., 2015b. Possible biosphere-lithosphere interactions preserved in igneous zircon and implications for Hadean Earth. Astrobiology, 15(7): 575-586.

Vaughan, D.J. and Corkhill, C.L., 2017. Mineralogy of Sulfides. Elements, 13(2): 81-87.

Villaros, A., Stevens, G., Moyen, J.-F. and Buick, I.S., 2009. The trace element compositions of S-type granites: evidence for disequilibrium melting and accessory phase entrainment in the source. Contributions to Mineralogy and Petrology, 158(4): 543-561.

Wake, B. and Taylor, G., 1988. Major's Creek, NSW, Australia—A Devonian epithermal gold deposit. Mineralium Deposita, 23(4): 239-246.

Wang, X.-S., Bi, X.-W., Leng, C.-B., Zhong, H., Tang, H.-F., Chen, Y.-W., Yin, G.-H., Huang, D.-Z. and Zhou, M.-F., 2014. Geochronology and geochemistry of Late Cretaceous igneous intrusions and Mo–Cu–(W) mineralization in the southern Yidun Arc, SW China:

implications for metallogenesis and geodynamic setting. Ore Geology Reviews, 61: 73-95.

Ward, J., Mavrogenes, J., Murray, A. and Holden, P., 2017. Trace element and sulfur isotopic evidence for redox changes during formation of the Wallaby gold deposit, Western Australia. Ore Geology Reviews, 82: 31-48.

Wells, J.D. and Mullens, T.E., 1973. Gold-bearing arsenian pyrite determined by microprobe analysis, Cortez and Carlin gold mines, Nevada. Economic Geology, 68(2): 187-201.

Whalen, J.B. and Chappell, B.W., 1988. Opaque mineralogy and mafic mineral chemistry of I- and S-type granites of the Lachlan fold belt, southeast Australia. American Mineralogist, 73(3-4): 281-296.

Widler, A. and Seward, T., 2002. The adsorption of gold (I) hydrosulphide complexes by iron sulphide surfaces. Geochimica et Cosmochimica Acta, 66(3): 383-402.

Wu, Y.-F., Fougerouse, D., Evans, K., Reddy, S.M., Saxey, D.W., Guagliardo, P. and Li, J.-W., 2019. Gold, arsenic, and copper zoning in pyrite: A record of fluid chemistry and growth kinetics. Geology, 47(7): 641-644.

Wyborn, D.a.S., S.S. , 1994. ,Sulphur-undersaturated magmatism—key

factor for generating magma-related copper -gold deposits. AGSO Research

Newsletter, 21: 7-8.

Yang, J., Barling, J., Siebert, C., Fietzke, J., Stephens, E. and Halliday, A.N., 2017. The molybdenum isotopic compositions of I-, S-and A-type granitic suites. Geochimica et Cosmochimica Acta, 205: 168-186.

Zajacz, Z., Candela, P.A. and Piccoli, P.M., 2017. The partitioning of Cu, Au and Mo between liquid and vapor at magmatic temperatures and its implications for the genesis of magmatic-hydrothermal ore deposits. Geochimica et Cosmochimica Acta, 207: 81-101.

Zhao, J., Liang, J., Li, J., Huang, Y., Liu, X., Zhang, J., Hao, J., Sun, W., Li, J. and Xie, J., 2020. Gold and sulfur sources of the Taipingdong Carlin-type gold deposit: Constraints from simultaneous determination of sulfur isotopes and trace elements in pyrite using nanoscale secondary ion mass spectroscopy. Ore Geology Reviews, 117: 103299.

Zheng, Y.F., 1991. Sulphur isotopic fractionation between sulphate and sulphide in hydrothermal ore deposits: disequilibrium vs equilibrium processes. Terra Nova, 3(5): 510-516.

Zhu, Y., An, F. and Tan, J., 2011. Geochemistry of hydrothermal gold deposits: a review. Geoscience Frontiers, 2(3): 367-374.